Spectroscopic Studies of the Gas Phase Complexes Benzene-Ammonia, Sodium-Water, and Sodium-Ammonia

Thesis by

David Allen Rodham

In Partial Fulfillment of the Requirements
for the Degree of
Doctor of Philosophy

California Institute of Technology
Pasadena, California

1997
(Submitted 27 February 1997)

Acknowledgements

I wish to thank several people who helped me arrive (finally) at the completion of this thesis. Most prominent among these individuals is my advisor Geoff Blake, who generously provided financial support during my lengthy stay at Caltech. Geoff supplied scientific support in even greater abundance, evidenced by his enthusiastic discussion of some new idea every time we talked. I'm most appreciative of his suggestion that I do ZEKE experiments on sodium-water and sodium-ammonia complexes, my only regret being that I did not act on his suggestion sooner.

Thanks are also due to the other members of Geoff's group- Sheng Wu, who with me shared the suffering of our first attempts at ZEKE spectroscopy and our lab move, Sakae Suzuki, who collaborated on the microwave work and provided a good example and a TV set during the three years we shared an apartment, Paul Stockman, who never gave up on group pizza, and Peter Green, who helped build the experimental apparatus. Thanks also to Roger Bumgarner, Pin Chen, and the people from the GPS division- Amir, Hui, and Zifu, who were brave enough to work for Geoff.

This work could not have been completed without the assistance of many other people at Caltech, in particular Guy Duremberg and Tony Stark of the chemistry instrument shop and Bart Pelsue of the GPS machine shop. Other helpful individuals were Geoff's secretary Jan Haskell and the chemistry graduate secretary Dian Buchness.

Graduate school was difficult, but it would have been even worse without a supportive family. I thank my parents Howard and Mary Rodham for their encouragement and prayers during my years in school. In every conversation with them they expressed their belief that this would eventually come to a successful conclusion. Finally, I would like to thank my wife Pon for her love and support. Along with my parents, this thesis is dedicated to her.

Abstract

The results of spectroscopic studies of the $C_6H_6(NH_3)$, $Na(H_2O)$, and $Na(NH_3)$ gas phase complexes are reported. The goal of these experiments was to obtain information upon which a more quantitative understanding of the intermolecular interactions found within them could be based. These intermolecular interactions, amino-aromatic hydrogen bonding in the $C_6H_6(NH_3)$ complex and the primarily electrostatic bonding of Na^+ to polar molecules in the $Na^+(H_2O)$ and $Na^+(NH_3)$ complexes, form the basis for many biologically significant processes.

The $C_6H_6(NH_3)$ dimer was investigated with resonant two-photon ionization (R2PI) and microwave spectroscopies. Using R2PI via the 6_0^1 transition of the benzene in the complex, it was found that the NH_3 is located above the benzene plane, on or near the benzene C_6 axis, and that the monomers undergo free or nearly free internal rotation. Subsequent high resolution microwave absorption and emission measurements of the rotational spectrum revealed that the center of mass separation (R_{cm-cm}) of the monomers is 3.59 Å and that the ammonia C_3 axis is tilted 58° from the benzene C_6 axis. In this geometry, the ammonia protons interact with the benzene π-cloud in a hydrogen-bonded geometry similar to that observed in high-resolution x-ray crystallography of protein structures.

The $Na(H_2O)$, $Na(D_2O)$, $Na(NH_3)$, and $Na(ND_3)$ complexes were studied with ZEKE-PFI (zero kinetic energy-pulsed field ionization) photoelectron spectroscopy. Spectra of all four complexes were obtained by single-photon ionization. For the $Na(NH_3)$ and $Na(ND_3)$ complexes, two-color (1+1′) photoionization was used as well, with the $\tilde{A}\ ^2E$ state serving as the intermediate resonance. Improved values for the ionization energies (IEs) and intermolecular stretching vibrational frequencies of the complexes were determined, while the intermolecular bending vibrational frequencies of $Na(NH_3)$ and $Na(ND_3)$ were measured for the first time. From the rotational structure observed in the ZEKE-PFI spectra, it was found that the Na-O and Na-N

bond lengths shrink by 5.2±0.5% when the complexes are ionized. The single-photon ZEKE-PFI spectra show transitions only between states of the same vibrational symmetry, in accord with the selection rule for allowed electronic transitions. Some of the two-color ZEKE-PFI spectra, however, show strong transitions between states of different vibrational symmetry which are attributed to vibronic coupling in the intermediate state. All of the single-photon spectra as well as the two-color spectra of $Na(NH_3)$ showed unusually strong O-branches, presumably the result of field-induced rotational autoionization. This effect is commonly observed in ZEKE-PFI spectroscopy, particularly for species such as $Na(H_2O)$ and $Na(NH_3)$ which combine small rotational constants with strongly anisotropic ion-electron scattering potentials.

Contents

Acknowledgements i

Abstract ii

1 Introduction 1

1.1 Introductory Remarks 1

1.2 Amino-Aromatic Hydrogen Bonding 2

1.3 Interactions of Alkali Metal Ions with Polar Molecules 7

Bibliography 13

2 Experimental Methods 17

2.1 Introduction 17

2.2 Complex Formation and Identification 17

2.2.1 Complex Formation 17

2.2.2 Complex Identification with the TOFMS 18

2.2.3 Vacuum Apparatus 19

2.3 Experimental Methods Used on the Benzene-Ammonia Dimer 20

2.3.1 R2PI Experiments 20

2.3.2 Microwave Experiments 23

2.4 Experimental Methods Used to Study Sodium-Water and Sodium - Ammonia Complexes 26

2.4.1 ZEKE-PFI Spectroscopy 26

2.4.2 The Pick-Up Source 27

2.4.3 The Sodium Oven 32

2.4.4 The ZEKE-PFI Apparatus 33

2.4.5 Lasers and Optics 39

2.5 Data Acquisition and Laser Scanning 39

Bibliography **47**

3 Structure of the Benzene-Ammonia Dimer **49**

3.1 Introduction 49

3.2 R2PI-TOFMS Results 50

3.3 Results of Microwave Experiments 62

3.4 Conclusions 71

Bibliography **72**

4 ZEKE-PFI Spectroscopy of the $Na(H_2O)$ and $Na(NH_3)$ Complexes **74**

4.1 Introduction 74

4.2 Results and Discussion 77

4.3 Rotational Structure 104

4.3.1 Single Photon Spectra 104

4.3.2 Two-Color ZEKE-PFI Spectra of $Na(NH_3)$ 118

4.4 Conclusions 128

Bibliography **130**

5 Conclusions and Future Directions **133**

Bibliography **136**

Appendix A The G_{36} MS Group **137**

Bibliography **142**

Appendix B Experimental Details **143**

B.1 Getting ZEKE-PFI Signals 143

B.2 The General Valve 143

B.3 The Interlock Circuit 144

B.4 Data Collection Software 147

List of Figures

1.1 Examples of amino-aromatic hydrogen bonds 3

1.2 Ion channels and binding sites 9

2.1 Energy levels used in R2PI of benzene-ammonia 21

2.2 R2PI experimental apparatus 24

2.3 Generation of ZEKE-PFI signal 28

2.4 Schematic of the sodium cluster pick-up source. 30

2.5 Schematic of the ZEKE-PFI apparatus. 34

2.6 ZEKE-PFI pulse circiut diagram and timing diagram. 37

2.7 Voltage divider and filter circuits used in ZEKE-PFI experiments. . . 40

2.8 Oscilloscope traces of the voltage pulse used and the signal obtained in ZEKE-PFI experiments. 42

2.9 Schematic of the ZEKE-PFI experimental apparatus. 44

3.1 TOFMS signal showing clusters of ammonia with benzene. 51

3.2 R2PI scans used to locate the 6_0^1 transition of the benzene-ammonia dimer 54

3.3 R2PI spectra of the 6_0^1 transition of $C_6H_6(NH_3)$ and $C_6H_6(ND_3)$. . . . 57

3.4 R2PI spectra of the 6_0^1 transition of C_6H_6 and $C_6H_6(NH_3)$. 59

3.5 Plot of R_{N-Bz} as a function of θ for benzene-ammonia 65

3.6 Structure of the benzene-ammonia dimer. 68

4.1 TOFMS signal showing clusters of water with sodium. 78

4.2 TOFMS signal showing clusters of ND_3 with sodium. 80

4.3 Single-photon ZEKE-PFI spectra of $Na(H_2O)$ and $Na(D_2O)$. 83

4.4 Single-photon ZEKE-PFI spectra of $Na(NH_3)$ and $Na(ND_3)$. 85

4.5 Transitions observed in single-photon ZEKE-PFI spectra. 88

4.6 Two-color (1+1′) photoionization spectra of $Na(ND_3)$. 92
4.7 Two-color (1+1′) photoionization spectra of $Na(NH_3)$. 96
4.8 Two-color ZEKE-PFI spectra of sodium-ammonia complexes. 99
4.9 Two-color ZEKE-PFI spectra of sodium-ammonia complexes. 102
4.10 Single-photon ZEKE-PFI spectra of sodium-water complexes. 106
4.11 Single-photon ZEKE-PFI spectra of sodium-ammonia complexes. . . 108
4.12 Single-photon ZEKE-PFI spectra of sodium-water complexes. 110
4.13 A comparison of $Na(NH_3)$ R2PI and ZEKE-PFI spectra. 113
4.14 Single-photon ZEKE-PFI spectra of $Na(NH_3)$ and $Na(H_2O)$. 115
4.15 Single-photon ZEKE-PFI spectra of the 0_0^{0+} transition of $Na(NH_3)$. . 119
4.16 R2PI and two-color ZEKE-PFI spectra of $Na(NH_3)$. 121
4.17 Two-color ZEKE-PFI spectra of $Na(NH_3)$. 123
4.18 Two-color ZEKE-PFI spectra of $Na(NH_3)$. 125

B.1 The interlock circuit 145

List of Tables

3.1 Nuclear spin statistical weights of $C_6H_6(^{14}NH_3)$. 61

3.2 Spectroscopic constants of Benzene-Ammonia. 62

3.3 Frequencies of rotational transitions observed with DAMW spectroscopy for $C_6H_6(^{14}NH_3)$. 63

3.4 Spectroscopic fits to m = 0 microwave data 63

3.5 Frequencies of benzene-ammonia rotational transitions observed with FTMW spectroscopy (MHz). 64

3.6 Hyperfine components of the J=3←2, K=2 transition of $C_6H_6(^{14}NH_3)$. 67

3.7 Stark field data for the benzene-ammonia rotational transitions observed with FTMW spectroscopy (MHz). The electric field was applied between plates having an effective separation of 33.8685 cm. 70

4.1 Ionization energies (IE), intermolecular stretching vibrational frequencies (ν_3), and intermolecular bending vibrational frequencies (ν_6) determined with ZEKE-PFI spectroscopy. 87

4.2 Parameters used to fit the $Na(NH_3)$ 0_0^0 and $3_0^1 6_0^1$ bands. 95

4.3 Separation of the P and O band heads (D_{PO}), the P and N band heads (D_{PN}), and the ratios of these values from the single-photon ZEKE-PFI spectra of the 0_0^{0+} transitions of $Na(H_2O)$ and $Na(NH_3)$. 112

A.1 Class Structure of the G_{36} MS Group 138

A.2 Character Table of the G_{36} MS Group 139

A.3 Symmetry of the Rotational Wavefunctions of $C_6H_6(^{14}NH_3)$. 139

A.4 Symmetry of the Torsional Wavefunctions of $C_6H_6(^{14}NH_3)$. 139

A.5 The Reducible Representation of the Nuclear Spin Wavefunctions of $C_6H_6(^{14}NH_3)$. 140

A.6 Reduction of the Reducible Representation of the Nuclear Spin Wavefunctions of $C_6H_6(^{14}NH_3)$. 141

A.7 Nuclear spin statistical weights of $C_6H_6(^{14}NH_3)$. 141

Chapter 1 Introduction

1.1 Introductory Remarks

This thesis describes experimental work that was performed with the aim of ultimately obtaining more quantitative descriptions of two types of molecular interactions that occur in biological systems: hydrogen bonding between amino and aromatic groups and ion-dipole bonding between alkali metal ions and small polar molecules. Amino-aromatic hydrogen bonding within a protein can influence its structure, while intermolecular amino-aromatic hydrogen bonding is sometimes a key interaction in the binding of molecules to the surfaces or active sites of proteins. The ability of membrane proteins to selectively transport Na^+ and K^+ into or out of cells, processes essential to cell function and signal transmission in nerve cells, is based in the interaction between the alkali ions and polar molecules or functional groups, as is the binding of these ions to a wide variety of molecules.

This work is a first step toward obtaining more accurate intermolecular potential energy surfaces (IPESs) which give the strengths of the van der Waals or hydrogen bond interactions as a function of the distance between the interacting species and the angles describing their relative orientation. As it is not possible to directly measure these interaction energies while the positional coordinates of the species are varied, the information upon which an IPES is based, as in the case of covalent bonds within molecules, is the equilibrium geometry of the system, the binding strength in that geometry, and its normal modes of vibration. Unfortunately, this information can be difficult or impossible to obtain from the condensed phase for many systems of interest due to the many body interactions present therein.

In order to circumvent these difficulties and acquire the information upon which improved IPESs can be based, I have spectroscopically studied simple model systems in which only pair-pair interactions are possible, the gas phase complexes $C_6H_6(NH_3)$,

$Na^+(H_2O)$, and $Na^+(NH_3)$. These complexes were formed in a supersonic jet expansion which also provided an ideal low temperature, collisionless environment for performing spectroscopic studies. The $C_6H_6(NH_3)$ dimer was probed with resonant two-photon ionization (R2PI) and microwave spectroscopies, which gave a high resolution structure for the complex, but little information on its intermolecular vibrational modes. Zero kinetic energy-pulsed field ionization (ZEKE-PFI) spectroscopy was used to study the $Na^+(H_2O)$ and $Na^+(NH_3)$ complexes, and, while the structures of the complexes were fully not determined, many of their intermolecular vibrational frequencies were measured.

1.2 Amino-Aromatic Hydrogen Bonding

The importance of hydrogen bonding in the structure and function of biological macromolecules has been appreciated for several decades. A conventional hydrogen bond is formed by a linear or nearly linear arrangement of the donating -OH or -NH group and the accepting electronegative atom, and typically has a strength of 2-7 kcal/mol [1]. Such bonds hold the two strands of DNA in the famed double helix geometry and are responsible for the formation of the α-helix and β-sheet structural motifs in proteins.

High resolution protein structures sometimes show evidence of less conventional hydrogen bonding interactions, among them the situation in which an aromatic ring acts as a hydrogen bond acceptor. In a study of drug binding to hemoglobin, for example, Perutz et al. observed that the amino group of asparagine pointed toward the π-cloud of a benzene ring on the drug, suggesting the participation of an amino-aromatic hydrogen bond in the drug binding [2]. Another occurrance of amino-aromatic hydrogen bonding was found in the binding of phosphotyrosyl peptides to the SH2 domain of v-src [3]. In this system, positively-charged amino groups of Lys and Arg bind to the phosphotyrosine ring, one on each side of the plane. These structures are shown in Figure 1.1.

Amino-aromatic hydrogen bonding within some proteins has been found to influ-

Figure 1.1: Amino-aromatic hydrogen bonds in the binding of (a) bezafibrate to hemoglobin (from Perutz et al. [2]), (b) a phosphotyrosyl peptide to the SH2 domain of v-src (from Waksman et al. [3]), and (c) acetylcholine to acetylcholinesterase (from Sussman et al. [9]).

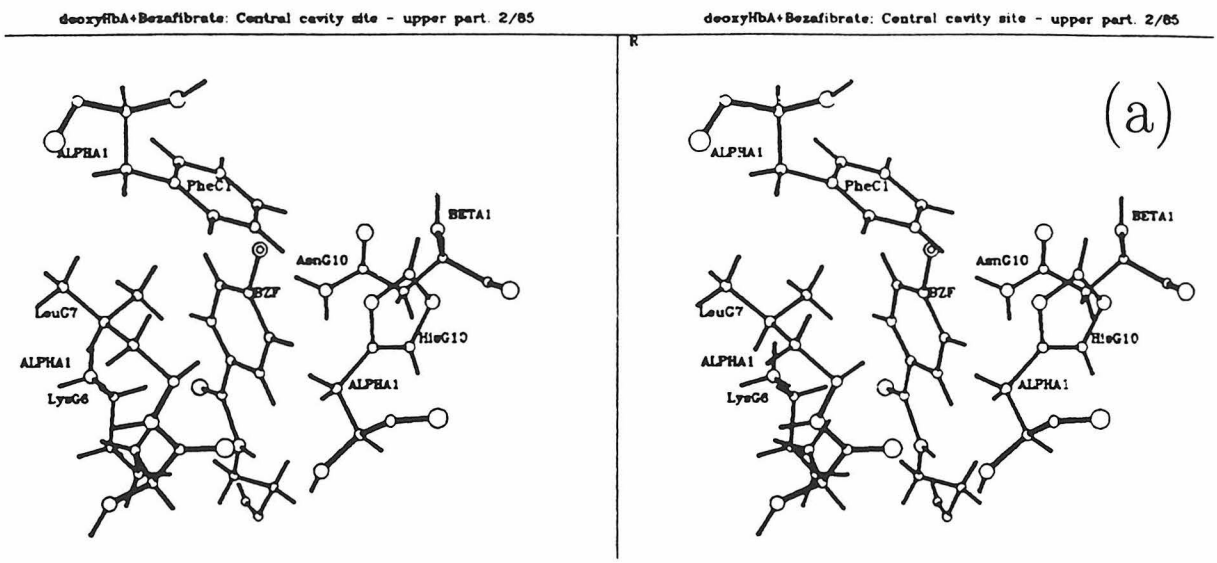
deoxyHbA+Bezafibrate: Central cavity site - upper part. 2/85
deoxyHbA+Bezafibrate: Central cavity site - upper part. 2/85
R
ALPHA1
PheC1
BETA1
AsnG10
BZF
LeuC7
HisG10
ALPHA1
LysG6
ALPHA1
(a)

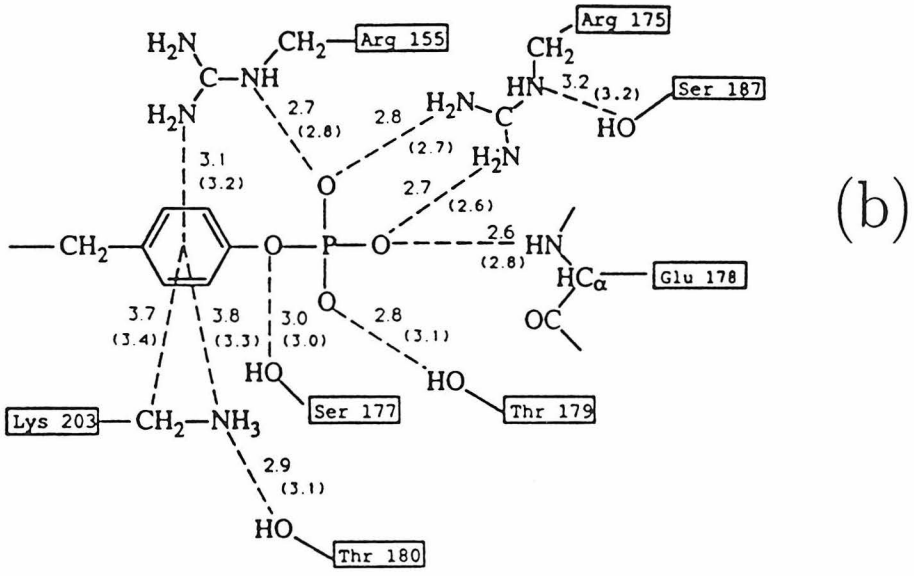
Arg 155
Arg 175
Ser 187
Glu 178
Ser 177
Thr 179
Lys 203
Thr 180
(b)

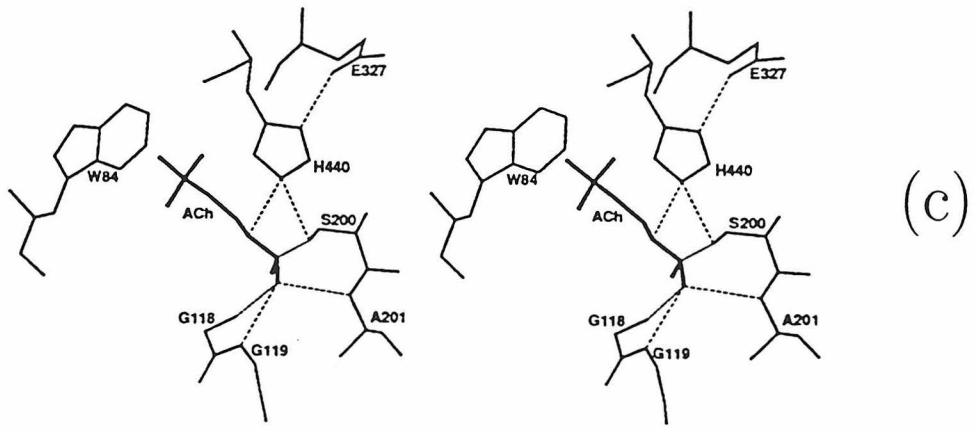
E327
H440
W84
ACh
S200
G118
A201
G119
(c)

ence their structure. Tüchsen and Woodward found that in the pancreatic trypsin inhibitor, an amide hydrogen bonds to each side of a phenylalanine ring [4]. Evidence of the hydrogen bonding in this case is purely structural, in that the amide groups are closer to the ring than the sum of the van der Waals distances. Burley and Petsko examined 33 protein structures and found that amino and aromatic groups interact more frequently than random, and that hydrogen bonded geometries are favored in the interaction [5]. Energetically, Loewenthal et al. studied the hydrogen bonding interaction between the NH of histadine and the indole ring of tryptophan and found the interaction strength to be only 1.4 kcal/mol [6]. Indeed, Mitchell et al. have pointed out that the neutral amino-aromatic hydrogen bonding is still quite rare because of the weakness of the interaction, being used only when conventional hydrogen bonding interactions are not possible [7].

Such "hydrogen bonding" is also important in the binding of acetylcholine to the active site of acetylcholinesterase. Following Dougherty's suggestion [8] that cation-π interactions, which have charge-induced dipole forces that can create substantially larger binding energies than are possible with neutral hydrogen bonds, are responsible for the binding of acetylcholine to acetylcholinesterase, Sussman et al. indeed found that the gorge leading to the active site contains many aromatic rings [9]. In the active site itself the tertiary ammonium group of acetylcholine forms hydrogen bonds with the indole ring of tryptophan, as shown in Figure 1.1c. Finally, there is also strong evidence that hydrogen bonding of acetylcholine's tertiary ammonium group to aromatic rings is important in its binding to the nicotinic acetylcholine receptor [10, 11].

Closely related to the issue of amino-aromatic hydrogen bonding is hydrogen bonding between aromatic groups and hydroxyl groups or water. Such hydrogen bonding has been shown to exist in model compounds. McPhail and Sim discovered an intramolecular hydrogen bond between a hydroxyl group and a benzene ring in a cyclic peptide [12]. Atwood et al. found that in some molecules which have cavities formed by aromatic rings, the water molecules in the cavities donate hydrogen bonds to the aromatic rings [13]. Even though the hydrophobic interaction generally forces aro-

matic groups to the interior region of proteins, it is now known that water molecules can move rapidly through certain protein structures, thereby leading to favorable hydrogen bonding interactions between water and interior aromatic groups.

As the strength of these hydrogen bonding interactions can be difficult to assess even in model systems, theoretical calculations often provide the only estimates of their magnitudes. Levitt and Perutz have estimated the strength of an NH-benzene hydrogen bond to be $\sim$3 kcal/mol, about half as strong as a typical hydrogen bond [14]. The calculations used to arrive at this value combined a Lennard-Jones 12-6 potential with the Coulomb interaction between the partial charges on the atoms. The distance between the benzene plane and the N atom varied from 2.9 to 3.6 Å. Although these results are very reasonable, some experimental verification of these findings is desirable.

The strongest foundation upon which IPESs describing pairwise amino-aromatic hydrogen bonding may be based is made up of experimental structural and vibrational data on complexes consisting only of two molecules, one with an amino group and the other with an aromatic ring. When complexes of this type are isolated in the gas phase and studied, the results are free from the effects of the external perturbations that complicate condensed phase measurements. In order to acquire such concrete experimental information on amino-aromatic hydrogen bonding, I have spectroscopically studied the model complex composed only of one benzene molecule and one ammonia molecule in the gas phase. Because the weakly-bound benzene-ammonia dimer is not stable at room temperature, the complex was formed and studied in the low temperature, collisionless environment provided by a supersonic jet expansion.

Numerous weakly bound complexes have been studied in supersonic jet expansions, and some complexes exhibiting hydrogen bond donation to benzene, such as the benzene-hydrogen chloride and benzene-water dimers, have been found. However, it is not obvious that the benzene-ammonia dimer should also have a hydrogen bonded structure. Indeed, Klemperer and coworkers have studied a wide variety of weakly bound complexes involving ammonia, and they did not find a single case in which ammonia donated a hydrogen bond, even when complexed with the strongest

acceptors [15]. The first question that must be answered, then, is whether or not the benzene-ammonia dimer can serve as a model of amino-aromatic hydrogen bonding.

The spectroscopic techniques used in this study of the benzene-ammonia dimer were resonant two-photon ionization (R2PI) and microwave spectroscopy. R2PI has previously been used by Bernstein's group to study this complex, but they did not use experimental conditions that allowed the spectral features of the complex to be isolated and identified [16]. The related benzene-water dimer has been the subject of an R2PI study by the Zwier group [17]. They obtained indirect evidence that the water donates a hydrogen bond to the benzene, but their spectral resolution did not allow them to confirm this. Although no microwave spectra of the benzene-ammonia dimer had been taken prior to this work, others in the Blake group used microwave spectroscopy to verify the existence of hydrogen bonding in the benzene-water dimer [18] and subsequently used a tunable far-infrared laser to study the vibrational modes of that complex [19]. Hopefully, such techniques will also be applied to the study of the benzene-ammonia dimer IPES.

1.3 Interactions of Alkali Metal Ions with Polar Molecules

The interactions between metal ions and polar molecules such as water are of fundamental importance to many areas. For example, such interactions influence the properties of electrolyte solutions and the rates of electron transfer reactions. In biological systems, many processes are based on the interaction between alkali ions and water or other molecules. For example, the Na^+/K^+ ATPase pump removes Na^+ from cells and imports K^+ into cells, maintaining the high intracellular K^+ and low intracellular Na^+ concentrations required by the cells. To accomplish this task, the ATPase membrane protein has sites of high Na^+ affinity on the interior of the cell membrane, and sites of high K^+ affinity on the exterior, which are able to remove the ions from the surrounding water. The ability of these binding sites to distinguish

between Na^+ and K^+ depends on the site structures and the energetics of removing the ions from water and placing them in the sites. Unfortunately, very little structural data for these binding sites is available at this time, and our understanding of the binding energetics is correspondingly low.

Signal transmission in nerve cells, accomplished by voltage-gated ion channel membrane proteins, also depends critically on the interaction between polar (and possibly non-polar) molecules and Na^+ and K^+ [20, 21, 22]. Upon opening, Na^+ channel proteins selectively allow Na^+ ions to flow into the cell, and K^+ channel proteins selectively allow K^+ to leave the cell. The ion selectively achieved by these proteins is determined not only by the interaction between the ion and the pore region of the protein, but also the water-cation and water-polar interactions in the pore. Other factors affecting selectivity are hydrogen bonding between the pore and the water molecules surrounding the ion, and the physical dimensions of the pore's selectivity filter. Selected illustrations of ion channels are shown in Figures 1.2a and 1.2b.

Although there is no high-resolution structural data available for ion channel pores, there is evidence which indicates that Na^+ channel pore dimensions are approximately 0.3 nm x 0.5 nm, making them larger than K^+ channel pores, which are believed to be 0.3 nm x 0.3 nm [23]. Na^+ pores are thought to be formed from the interaction of Na^+ with partially-negative oxygen atoms of such as those in carbonyl groups, while K^+ pores are believed to be formed via the cation-π interaction between K^+ and non-polar aromatic rings as shown in Figure 1.2c [24, 25, 26]. Recent theoretical results have suggested that the Na^+ channel pores must be large enough to allow a Na^+ ion along with its first solvation shell of three water molecules to pass through intact, and that Na^+ cannot pass through K^+ channel pores because the desolvation required to drive the Na^+ through the smaller pore is energetically prohibitive [27]. The results further suggest that K^+ cannot go through Na^+ channel pores because its interaction with H_2O is not strong enough to cause a displacement of the H_2O molecules in the pores, which are hydrogen-bonded to polar groups on the protein. However, since K^+ channels are not believed to have polar groups to which H_2O can

Figure 1.2: (a) Illustration of ion channel proteins embedded in a cell membrane [20]. (b) Cut-away illustration of an ion channel protein showing the water-filled pore and the selectivity filter [20]. (c) Illustration of the proposed selectivity filter in K^+ channel proteins (From Miller[26]). (d) Illustration of the K^+ binding site in DGD (From Miller[26]).

(a) (b)

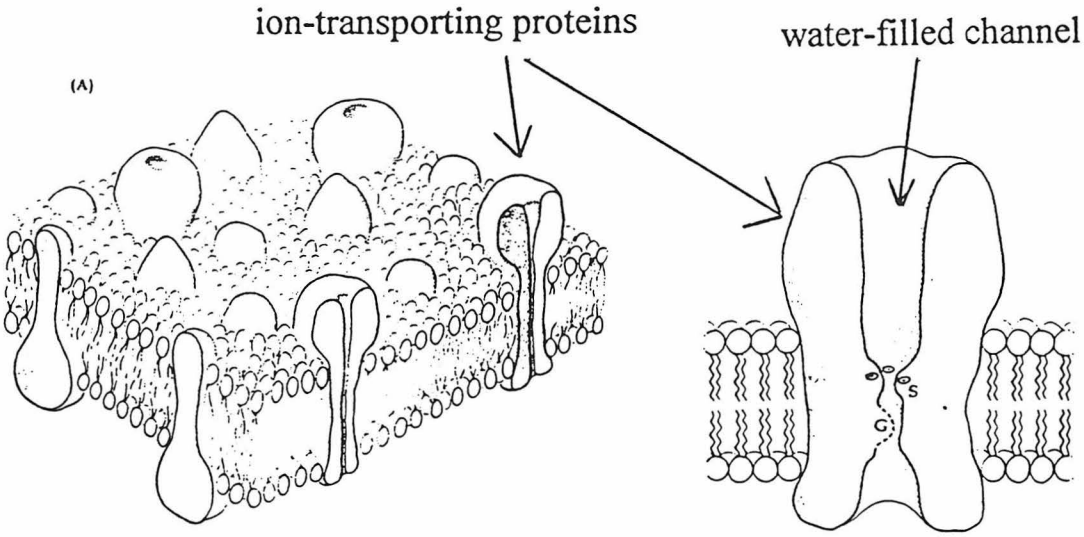

Ion channels in cell membrane select between Na^+ and K^+

(s) selectivity filter

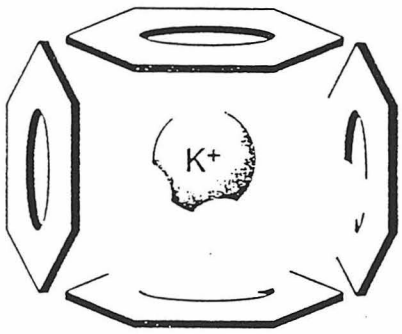

Proposed binding site

(c)

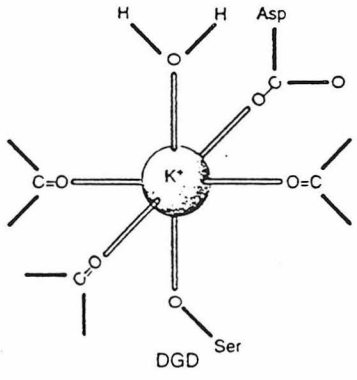

K^+ binding site

(d)

hydrogen bond, K^+ is able to displace water molecules in the pore and pass through it.

While structural data for ion channels is lacking, some insight may be gained from the recently determined structure of the K^+ binding site in another protein, the enzyme dialkylglycine decarboxylase (DGD), in which a K^+ ion in the site is coordinated by six oxygen atoms in an octahedral arrangement, as shown in Figure 1.2d [28]. Three oxygens are from carbonyl groups, and the other three are supplied by a carboxyl group, a hydroxyl group, and a water molecule. However, when a Na^+ ion occupies the site, the cavity shrinks to accomodate the smaller ion, forcing the hydroxyl oxygen out of the cavity and leaving the Na^+ coordinated by five oxygens in a distorted trigonal bipyramidal geometry. The site preferentially binds K^+, the selectivity being determined by the energetics of the interaction of the ions with the polar oxygen-containing groups as well as the energy of the overall protein structure.

Clearly, accurate potentials describing the interaction between alkali metal ions and water and between the ions and groups that might line ion channels are required in order to determine how ion channels and protein binding sites achieve selectivity. Although much has been learned about alkali ion hydration from thermochemical and transport data [29], neutron diffraction [30], Raman spectroscopy [31], and theoretical methods [32, 33, 34], the modeling of the complex environment inside the tiny ion channel pores and protein binding sites requires more accurate information on structure and energetics than these methods can provide. In order to have stringent guides for computational work, the IPES describing the interaction between an alkali ion and one water molecule must be determined with high accuracy, as must the IPESs describing alkali ion interactions with only a few solvent molecules.

The best way to acquire the necessary experimental data is through the spectroscopic study of isolated complexes composed only of an alkali metal ion and one or a few solvent molecules in the gas phase. While binding energies of complexes composed of Na^+ and a small number of water or ammonia molecules have been measured in high pressure mass spectrometry experiments [35, 36], the only measurements of vibrational frequencies of such complexes were made by Hertel and

coworkers, who measured the sodium-water and sodium-ammonia stretching frequencies in the 1:1 complexes [37, 38]. Although there is no direct structural data for any of these complexes, the results of numerous calculations of their structures agree quite well [39, 40, 41, 42]. However, accurate experimental structural data is still needed, because small geometry changes can have large consequences in constricted ion channels and binding sites.

As a step toward acquiring the necessary structural and vibrational data, I have used a "pick-up" source to create jet-cooled gas phase $Na(H_2O)$ and $Na(NH_3)$ complexes and ZEKE-PFI spectroscopy to study them. ZEKE-PFI spectroscopy, a powerful technique for obtaining high resolution spectra of molecular and cluster ions, is based on the detection of threshold photoelectrons generated in the laser ionization of their neutral precursors [43]. With this technique, several vibrational frequencies of the complexes were measured, and some structural information derived.

An outline of the remainder of this thesis is as follows. The experimental techniques and apparatus used in this work are described in Chapter 2. The results of the R2PI and microwave experiments on the benzene-ammonia dimer are presented in Chapter 3, while the results of the ZEKE-PFI experiments on the $Na(H_2O)$ and $Na(NH_3)$ complexes are presented in Chapter 4. Conclusions and directions for future work are given in Chapter 5. Appendices are then included which discuss the G_{36} molecular symmetry group used in the work on the benzene-ammonia dimer and operational details for the experimental apparatus.

Bibliography

[1] G.C. Pimentel and A.L. McClellan, *The Hydrogen Bond*, Freeman, San Francisco, 1960.

[2] M.F. Perutz, G. Fermi, D.J. Abraham, C. Poyart, and E. Bursaux, *J. Am. Chem. Soc.*, 108:1064, 1986.

[3] G. Waksman, D. Kominos, S. Robertson, N. Pant, D. Baltimore, R. Birge, D. Cowburn, H. Hanafusa, B. Mayer, M. Overduin, M. Resh, C. Rios, L. Silverman, and J. Kuriyan, *Nature*, 358:646, 1992.

[4] E. Tüchsen and C. Woodward, *Biochemistry*, 26:1918, 1987.

[5] S.K. Burley and G.A. Petsko, *FEBS Lett.*, 203:139, 1986.

[6] R. Loewenthal, J. Sancho, and A.R. Fersht, *J. Mol. Biol.*, 224:759, 1992.

[7] J.B.O. Mitchell, C.L. Nandi, S. Ali, I.K. McDonald, J.M. Thornton, S.L. Price, and J. Singh, *Nature*, 366:413, 1993.

[8] D.A. Dougherty and D.A. Stauffer, *Science*, 250:1558, 1990.

[9] J.L. Sussman, M. Harel, F. Frolow, C. Oefner, A. Goldman, L. Toker, and I. Silman, *Science*, 253:872, 1991.

[10] M. Dennis, J. Giraudat, F. Kotzyba-Hilbert, M. Goeldner, C. Hirth, J.Y. Chang, C. Lazure, M. Chrétien, and J.P. Changeux, *Biochemistry*, 27:2346, 1988.

[11] J.L. Galzi, F. Revah, D. Black, M. Goeldner, C. Hirth, and J.P. Changeux, *J. Biol. Chem.*, 265:10430, 1990.

[12] A.T. McPhail and G.A. Sim, *Chem. Commun.*, 125, 1965.

[13] J.L. Atwood, F. Hamada, K.D. Robinson, G.W. Orr, and R.L. Vincent, *Nature*, 349:683, 1991.

[14] M. Levitt and M.F. Perutz, *J. Mol. Biol.*, 201:751, 1988.

[15] D.D. Nelson, Jr., G.T. Fraser, and W. Klemperer, *Science*, 238:1670, 1987.

[16] J. Wanna, J.A. Menapace, and E.R. Bernstein, *J. Chem. Phys.*, 85:1795, 1986.

[17] A.J. Gotch and T.S. Zwier, *J. Chem. Phys.*, 96:3388, 1992.

[18] S. Suzuki, P.G. Green, R.E. Bumgarner, S. Dasgupta, W.A. Goddard III, and G.A. Blake, *Science*, 257:942, 1992.

[19] Sakae Suzuki, *Towards a More Quantitative Understanding of Intermolecular Interactions: Biologically Significant Intermolecular Clusters*, Ph.D. thesis, California Institute of Technology, 1996.

[20] J.G. Nicholls, A.R. Martin, and B.G. Wallace, *From Neuron to Brain: A Cellular and Molecular Approach to the Function of the Nervous System*, Sinauer Associates, Sunderland, MA, 1992.

[21] C. Miller, *Science*, 252:1092, 1991.

[22] W.A. Catterall, *Science*, 242:50, 1988.

[23] B. Hille, *Ionic Channels of Excitable Membranes*, Sinauer, Sunderland, MA, 1992.

[24] L. Heginbotham and R. MacKinnon, *Neuron*, 8:483, 1992.

[25] R.A. Kumpf and D.A. Dougherty, *Science*, 261:1708, 1993.

[26] C. Miller, *Science*, 261:1692, 1993.

[27] L. Degreve, S.M. Vechi, and C. Quintale, Jr., *Biochim. Biophys. Acta*, 1274:149, 1996.

[28] M.D. Toney, E. Hohenester, S.W. Cowan, and J.N. Jansonius, *Science*, 261:756, 1993.

[29] J.O.M. Bockris and A.K.N. Reddy, *Modern Electrochemistry*, Vol.1,Plenum, New York, 1970.

[30] E. Kálmán and G. Pálinkás in *The Chemical Physics of Solvation*, part B, ed. by R.R. Dogonadze,E. Kálmán, A.A. Kornyshev, and J. Ulstrup, Elsevier, Amsterdam 1988.

[31] W. Rudolph, M.H. Brooker and C.C. Pye, *J. Phys. Chem.*, 99:3793, 1995.

[32] L. Degreve and C. Quintale, Jr., *Electrochim. Acta*, 38:1405, 1992.

[33] L. Perera and M.L. Berkowitz, *J. Chem. Phys.*, 95:1954, 1991.

[34] M. Migliore, S.L. Fornili, E. Spohr, G. Palinkas, and K. Heinzinger, *Z. Naturforsch*, 41a:826, 1986.

[35] I. Džidić and P. Kebarle, *J. Phys. Chem.*, 74:1466, 1970.

[36] A.W. Castleman, Jr., P.M. Holland, D.M. Lindsay and K.I. Peterson, *J. Am. Chem. Soc.*, 100:6039, 1978.

[37] C.P. Schulz, R. Haugstätter, H.U. Tittes and I.V. Hertel, *Phys. Rev. Letters*, 57:1703, 1986.

[38] C. Nitsch, C.P. Schulz, A. Gerber, W. Zimmermann-Edling and I.V. Hertel, *Z. Physik D*, 22:651, 1992.

[39] C.W. Bauschlicher, Jr., S.R. Langhoff, H. Partridge, J.E. Rice and A. Komornicki, *J. Chem. Phys.*, 95:5142, 1991.

[40] K. Hashimoto and K. Morokuma, *J. Am. Chem. Soc.*, 116:11436, 1994.

[41] K. Hashimoto and K. Morokuma, *J. Am. Chem. Soc.*, 117:4151, 1995.

[42] J.C. Greer, C. Hüglin, I.V. Hertel and R. Ahlrichs, *Z. Physik D*, 30:69, 1994.

[43] K. Müller-Dethlefs and E.W. Schlag, *Ann. Rev. Phys. Chem.*, 42:109, 1991.

Chapter 2 Experimental Methods

2.1 Introduction

The experiments presented in Chapters 3 and 4 involved three general steps: first, making the complexes, second, verifying the existence of the complexes and third, acquiring spectra of the complexes. Each is described in detail below. Briefly, the complexes were formed in supersonic jet expansions of the appropriate gases. Their existence was verified with a photoionization time-of-flight mass spectrometer (TOFMS). Spectra of the benzene-ammonia dimer were obtained with R2PI spectroscopy and microwave spectroscopy. While R2PI was put to some use in the study of the sodium-water and sodium-ammonia complexes, ZEKE-PFI spectroscopy was the main technique employed because it gives spectra of the ionized complexes, which were of the most interest. Since all three steps demand a vacuum environment, the complexes were formed and studied in a differentially-pumped vacuum apparatus comprised of three chambers.

2.2 Complex Formation and Identification

2.2.1 Complex Formation

Due to their instability at room temperature, the weakly-bound complexes were formed in a supersonic jet expansion (SJE) [1, 2]. A SJE is created as a gas expands from a reservoir of high pressure into vacuum through an orifice having a diameter much larger than the mean free path of the gas molecules in the reservoir. Usually, the molecule of interest is seeded in argon or helium. As the gas expands, the molecules experience many collisions in the orifice and just beyond it, in which internal molecular energy is converted to translational energy. Translational cooling

is achieved because the molecules in the SJE have a very narrow velocity distribution. Cooling of the molecular internal degrees of freedom enhances aggregation, and complexes which would be unstable at room temperature are formed. Besides providing an intense cluster source, SJEs also offer a collisionless, low-temperature environment in which molecular spectra are greatly simplified.

The SJE formed in the source chamber was skimmed by a 2 mm diameter skimmer (Beam Dynamics) 5-10 cm downstream of the nozzle, making a collimated cluster beam in the probe chamber where the complexes were ionized. The ZEKE-PFI apparatus was contained in this chamber, to which was attached the third chamber, the flight tube of the TOF.

2.2.2 Complex Identification with the TOFMS

Laser-ionization TOF mass spectrometry was used to verify the existence of the complexes in the molecular beam. Single-photon ionization was used for the $Na(H_2O)$ and $Na(NH_3)$ complexes, while R2PI was employed in the experiments on the benzene-ammonia dimer. The TOFMS was also crucial in isolating spectra of the benzene-ammonia dimer by R2PI, since mass resolution assured that the R2PI signal was from the correct complex.

The TOFMS was a commercial angular reflectron [3, 4] instrument from R.M. Jordan Co. It housed a microchannel plate (MCP) detector at the end of the 1.1 m flight tube for use as a standard TOFMS when it was not used in the reflectron mode (which was usually the case). A Wiley-McClaren ion source [5], located 50 cm from the pulsed nozzle, was used to achieve spatial and temporal focusing. A 4 mm x 1 mm skimmer (Beam Dynamics) placed just before the ion source created a narrow strip of clusters between the extraction grids and limited the amount of gas entering the TOF. The extraction field of 315 V/cm and the acceleration field of 3000 V/cm were obtained by holding the repeller plate at 4200 V and the extraction grid at 3800 V. The Einzel lens was not used. The MCP detector was operated at a voltage of 1800 $\pm$ 300 V, depending on the signal strength. A set of VXY deflector plates

was used to guide the ions to ensure that they hit the MCP detector. For molecules traveling at the molecular beam speed, large ions with long flight times will travel farther along the molecular beam direction (perpendicular to the TOF in this case) while in the flight tube than will small ions and may therefore miss the detector. For the benzene-ammonia complex in a helium expansion, VXY = 0 was good, while for the sodium complexes in an argon expansion, VXY2 = 80-100 V worked best. The output signal from the detector was sent to an EG&G 9301 preamplifier ($\times$10 gain) and from there to a LeCroy 9400A digital oscilloscope.

2.2.3 Vacuum Apparatus

Each chamber was pumped by a diffusion pump (DP), and the diffusion pumps were backed by an Edwards EM2-275 mechanical pump. The source chamber was pumped by an unbaffled Varian VHS-10 DP , the probe chamber by a Varian VHS-6 DP with a water-cooled baffle, and the TOFMS was pumped by an Edwards DIFFSTAK 100 DP, also with a water baffle. Typical operating pressures in the source, probe, and TOF chambers were 5×10^{-5} Torr, 5×10^{-7} Torr, and 5×10^{-8} Torr, respectively. The roughing line was 4″ i.d. PVC pipe which ran from the roughing pump to the 10″ DP, and 2″ PVC pipe was connected from that point to the other DP outlets. Pneumatic gate valves were placed between the chambers and their DPs. To protect the chambers, an interlock system was used to turn off the DPs and close the gate valves in the event of excessive pressure or loss of cooling water. This circuit is described in Appendix B.

2.3 Experimental Methods Used on the Benzene-Ammonia Dimer

2.3.1 R2PI Experiments

The first technique used to study the $C_6H_6(NH_3)$ complex was resonant two-photon ionization (R2PI). In these experiments, laser radiation with a photon energy greater than one-half of the ionization potential (IP) of the complexes intersected the molecular beam in the ionization region of the TOFMS. While molecules can be ionized by a nonresonant two-photon process, the ionization is 3-4 orders of magnitude more efficient when the laser frequency is resonant with a transition to an excited electronic eigenstate of the molecule. By detecting the ion of interest with the TOFMS as the laser frequency is scanned, the electronic absorption spectrum of the molecule may be obtained.

The benzene in the $C_6H_6(NH_3)$ complex was ionized with R2PI using its S_1 state ($^1B_{2u}$ symmetry), which lies 38086 cm^{-1} above the ground state ($^1A_{1g}$ symmetry) [6], as the intermediate resonance, as shown in Figure 2.1. Although the $S_1 \leftarrow S_0$ transition is forbidden by symmetry, strong transitions to vibrational states of e_{2g} symmetry in the S_1 state occur because they "borrow" intensity from the S_3 ($^1E_{1u}$) $\leftarrow S_0$ transition through a Herzberg-Teller vibronic coupling mechanism. Consequently, the first strong band in the $S_1 \leftarrow S_0$ spectrum of free benzene does not correspond to the 0_0^0 transition, but rather to the 6_0^1 transition, since the ν_6 vibrational mode possess e_{2g} symmetry. This well-characterized transition is suitable for R2PI of benzene because it occurs at an energy of 38606 cm^{-1} [7], which is greater than one-half of the IP of benzene (74555 cm^{-1}) [8]. Since the lifetime of the 6^1 level is 79 ns [9], there were no complications from lifetime broadening. The 6_0^1 transition was used in all of the R2PI experiments on the benzene-ammonia dimer.

$C_6H_6(NH_3)$ complexes were formed by expanding a mixture of He, C_6H_6 (0.05%-0.2%), and NH_3 (0.01%-0.3%) at a total pressure of 23 psig through a piezoelectric-driven pulsed nozzle. The valve, designed by Proch and Trickl [10], had a 1 mm

Figure 2.1: Partial energy level diagram of benzene emphasizing states involved in the R2PI process via the S_1 electronic state.

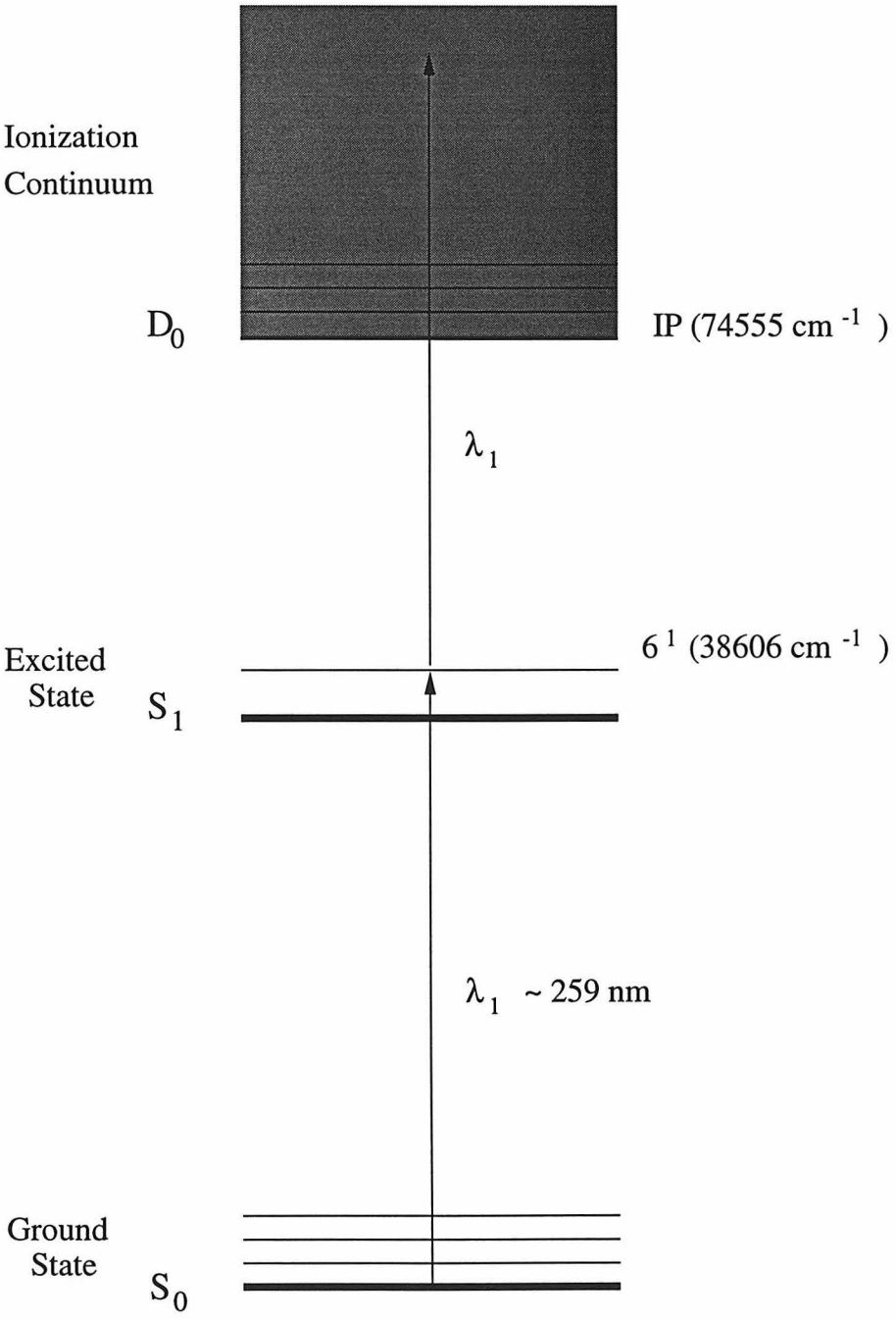
Ionization
Continuum
D_0
IP (74555 cm $^{-1}$)
λ_1
Excited
State
S_1
6^1 (38606 cm $^{-1}$)
λ_1 ~ 259 nm
Ground
State
S_0

diameter orifice and an open time of ~200 μs. The driver circuit developed by Johnson was used [11]. The rotational temperature of the complexes formed in this expansion was ~1 K. The gas mixing ratios were controlled by three mass flow controllers (MFCs) from MKS. One controller regulated the helium carrier gas flow, another regulated the flow of a helium-benzene mix obtained by bubbling He through room-temperature benzene, and the third controlled the flow of a 50:1 He:NH_3 mixture. The gas flow rate through the pulsed nozzle was low compared to the flow rates that the MFCs could accurately regulate, so the total flow was increased by discarding most of the gas mixture between the MFCs and the pulsed nozzle. This allowed the NH_3 to be accurately diluted, an essential step in eliminating interfering signals from larger $C_6H_6(NH_3)_n$ clusters.

In the benzene-ammonia experiments, a XeCl excimer laser (Lambda Physik LPX 120) was used to pump a dye laser (Lambda Physik Fl 3002E) at a repetition rate of 50 Hz. The bandwidth of the dye laser's output is nominally 0.2 cm^{-1}. In some experiments, this was narrowed to 0.04 cm^{-1} by using an intracavity etalon with a free spectral range of 1 cm^{-1} and a finesse of 25. Coumarin 503 dye was used in the dye laser, the output of which was frequency doubled with an angle-tuned BBO crystal, giving 0.1-1 mJ of UV light. A Pellin-Broca harmonic separator removed the remaining fundamental from the beam. Fused silica prisms were used to steer the UV beam to the vacuum apparatus, entering via a fused silica window located on top of the chamber, directly above the ionization region of the mass spectrometer. No focusing optics were necessary. A schematic of the R2PI experimental apparatus is shown in Figure 2.2.

2.3.2 Microwave Experiments

Microwave data for the benzene-ammonia dimer were recorded with two spectrometers, one a direct absorption microwave (DAMW) spectrometer at Caltech and the other a Fourier transform microwave (FTMW) spectrometer at NIST. Both instruments have been described in the literature [12, 13], and Suzuki has discussed their

Figure 2.2: Schematic of the experimental apparatus used in R2PI studies of the benzene-ammonia dimer.

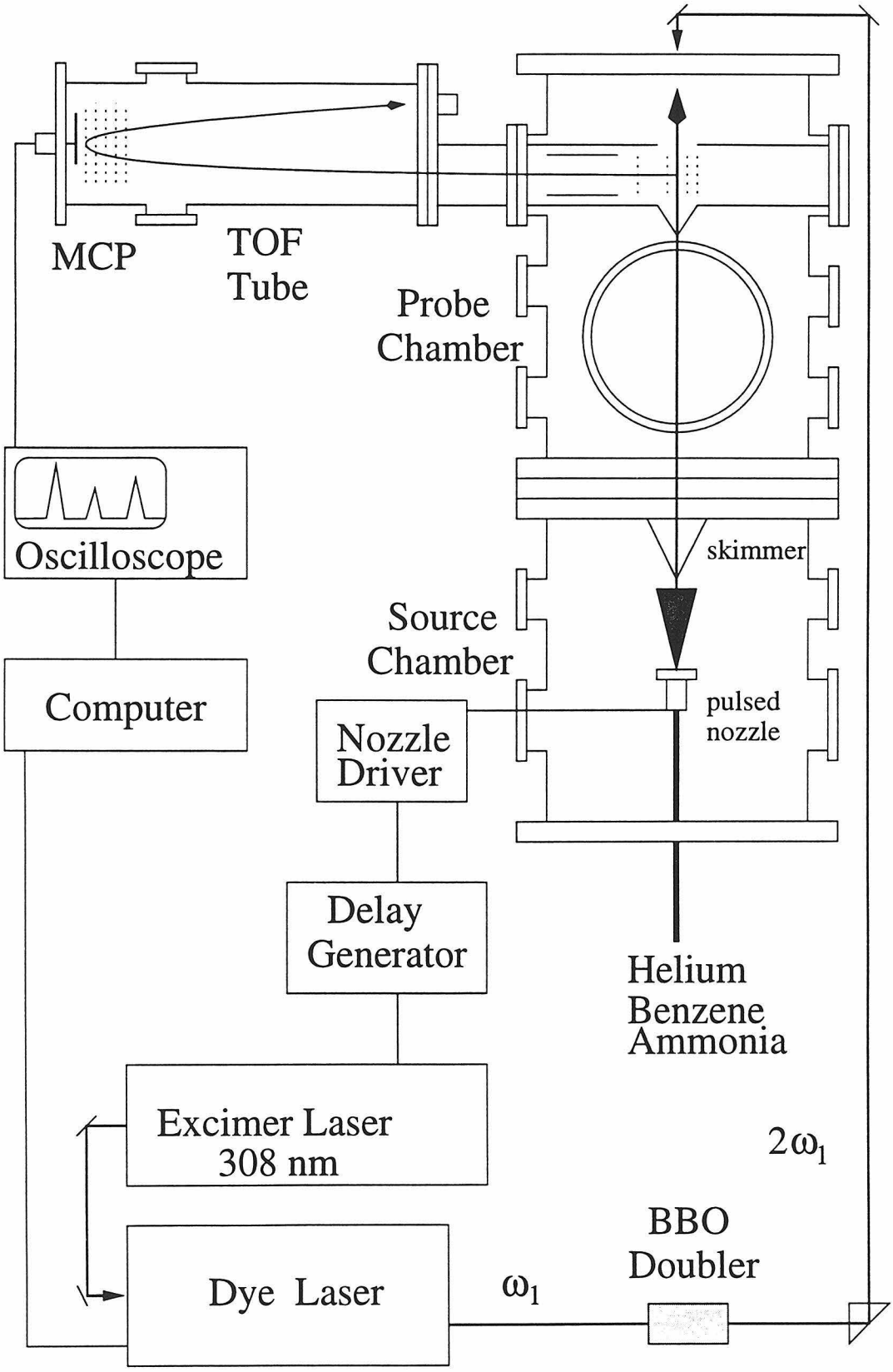
MCP
TOF
Tube
Probe
Chamber
skimmer
Source
Chamber
pulsed
nozzle
Oscilloscope
Computer
Nozzle
Driver
Delay
Generator
Helium
Benzene
Ammonia
Excimer Laser
308 nm
$2\omega_1$
BBO
Doubler
Dye Laser
ω_1

use in the study of the related benzene-water dimer [14]. Only a very brief description of the experiments will be given here.

The DAMW spectrometer, which employed Stark modulation, can scan large regions quickly and autonomously, and first detected benzene-ammonia rotational transitions. A gas mix of 1% benzene and ammonia each in argon (backing pressure 10 psig) was expanded through a 50 mm $\times$0.025 mm slit nozzle into vacuum. Microwave radiation propagated perpendicular to the gas flow and parallel to the slit nozzle. The Stark modulation field was a 100 kHz square wave with a magnitude of 12 V/cm. After passing through the SJE, the microwaves impinged on a detector, the output of which was routed to a lock-in amplifier. The resolution was 1 MHz, and the signal-to-noise ratio was barely good enough to detect the absorption of the benzene-ammonia dimer.

The resolution of the DAMW was sufficient to measure accurately the B rotational constant for the benzene-ammonia dimer, but it was not good enough to resolve the nuclear quadrupole coupling splittings. Once an accurate predicted spectrum was available, the FTMW instrument, which has extremely high sensitivity and a resolution of $\sim$10 kHz but rather slow scanning speeds, was used to measure this and also the dipole moment of the complex. The gas flow through this system is also substantially less than that for the DAMW spectrometer, so it was also used to record data for the isotopic species $C_6H_6(^{15}NH_3)$ and $C_6H_6(^{14}ND_3)$.

2.4 Experimental Methods Used to Study Sodium-Water and Sodium -Ammonia Complexes

2.4.1 ZEKE-PFI Spectroscopy

ZEKE-PFI spectroscopy was used to obtain vibrational frequencies and some structural information for the $Na^+(H_2O)$ and $Na^+(NH_3)$ complexes. The ability of ZEKE-PFI spectroscopy to give high resolution spectra of molecular and cluster ions is well-documented [15, 16, 17, 18]. ZEKE-PFI electrons are generated only when the

laser photon energy is a few cm^{-1} less than the energy required to reach a quantum state of the ion, as illustrated in Figure 2.3. In this situation, high principal quantum number Rydberg states are created, which have long lifetimes. After a delay of 1-3 μs during which kinetic electrons exit the extraction region, a small voltage is applied to one extraction plate, creating an electric field which ionizes the high-n Rydberg states and accelerates the ZEKE-PFI electrons toward an MCP detector, giving zero-background detection of the threshold photoelectrons.

High-n Rydberg states of the Na atoms in the complexes were populated by single-photon excitation using tunable UV light, and, in the complexes with ammonia, by a two-color (1+1′) excitation process using visible photons. The first transition in this two-color process is the analogue of the 3p←3s transition of the free Na atom. Two-color excitation gave access to states that could not be reached by single-photon excitation.

2.4.2 The Pick-Up Source

Since sodium and water cannot be co-expanded from the same reservoir, $Na(H_2O)$ and $Na(NH_3)$ complexes were formed in a "pick-up" source, similar to that used by Hertel and coworkers [19, 20]. A SJE containing either pure NH_3 or H_2O seeded in Ar was crossed by an effusive beam of Na atoms. Collisions entrained the Na atoms in the SJE, where a small fraction of them formed complexes. The aperture of the Na oven, heated to 630 K, was 5 mm below and 5 mm downstream of the orifice of the pulsed valve (General Valve, series 9, high temperature version, 0.8 mm nozzle diameter). A drawing of this source is shown in Figure 2.4. A General Valve was used instead of the piezoelectric valve because heating of the valve by the nearby Na oven caused the piezoelectric valve to perform poorly. The rotational temperature of the complexes formed in this source was ~100 K.

Complexes with water were formed by expanding 1 atm. of water vapor with 1.5 atm. of argon carrier gas, while complexes with ammonia were formed by expanding 3 atm. of ammonia neat. For these expansion gas mixtures, optimum cluster signal was

Figure 2.3: Energy levels involved in the generation of ZEKE-PFI signal. The top of each shaded area represents an ionization limit of the molecule when no electric field is applied, while the bottom of each shaded area represents the lowered ionization limit in the pulsed electric field. With no field applied, laser radiation populates the Rydberg states within the shaded areas. After a delay of 1-3 μs, the electric field is pulsed on, ionizing the molecules and generating ZEKE-PFI electrons, which are detected.

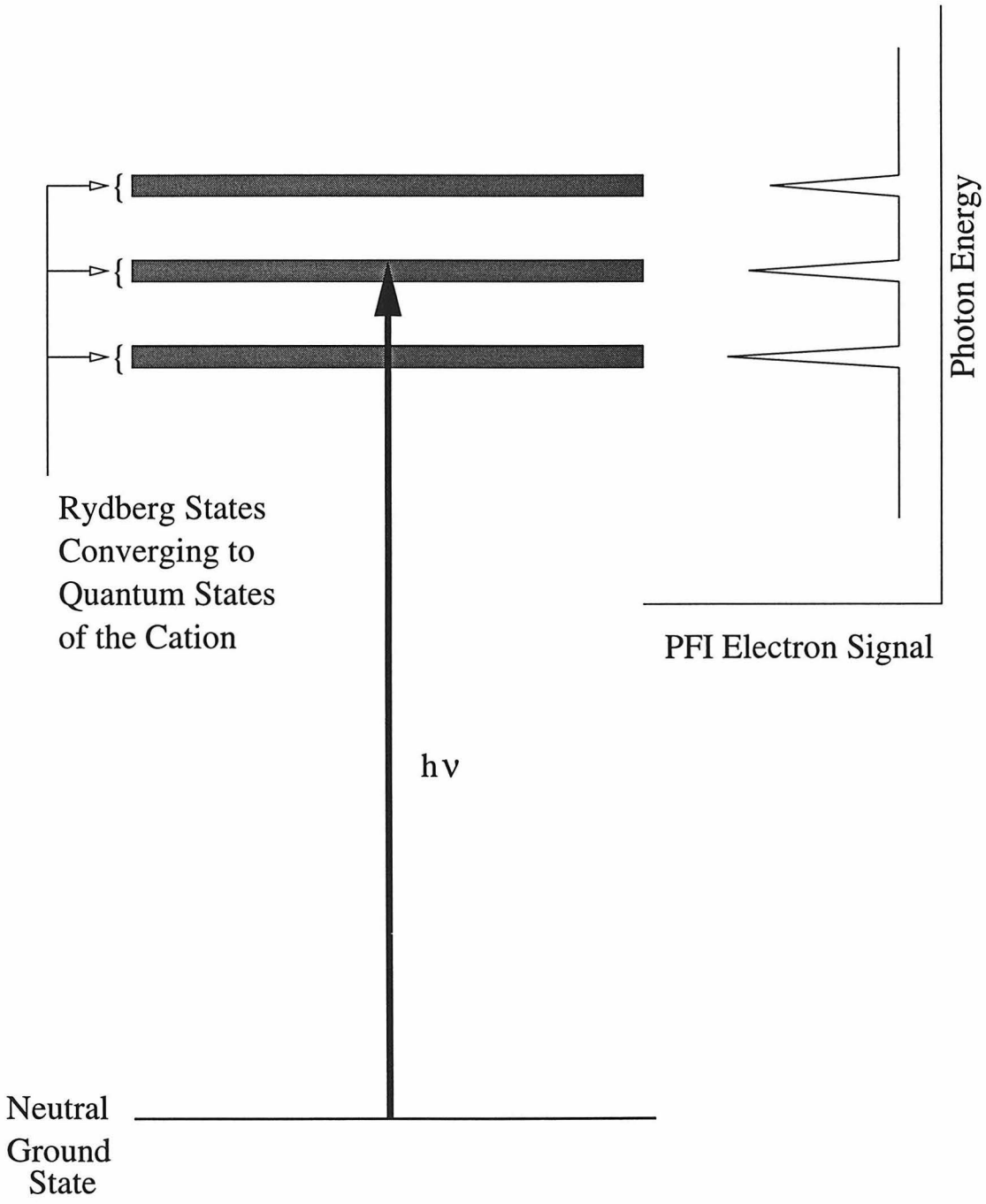
Photon Energy
Rydberg States
Converging to
Quantum States
of the Cation
PFI Electron Signal
hν
Neutral
Ground
State

Figure 2.4: Schematic of the sodium cluster pick-up source. The heating blocks are shown in a "cut away" fashion to expose the sodium oven and the cartridge heaters.

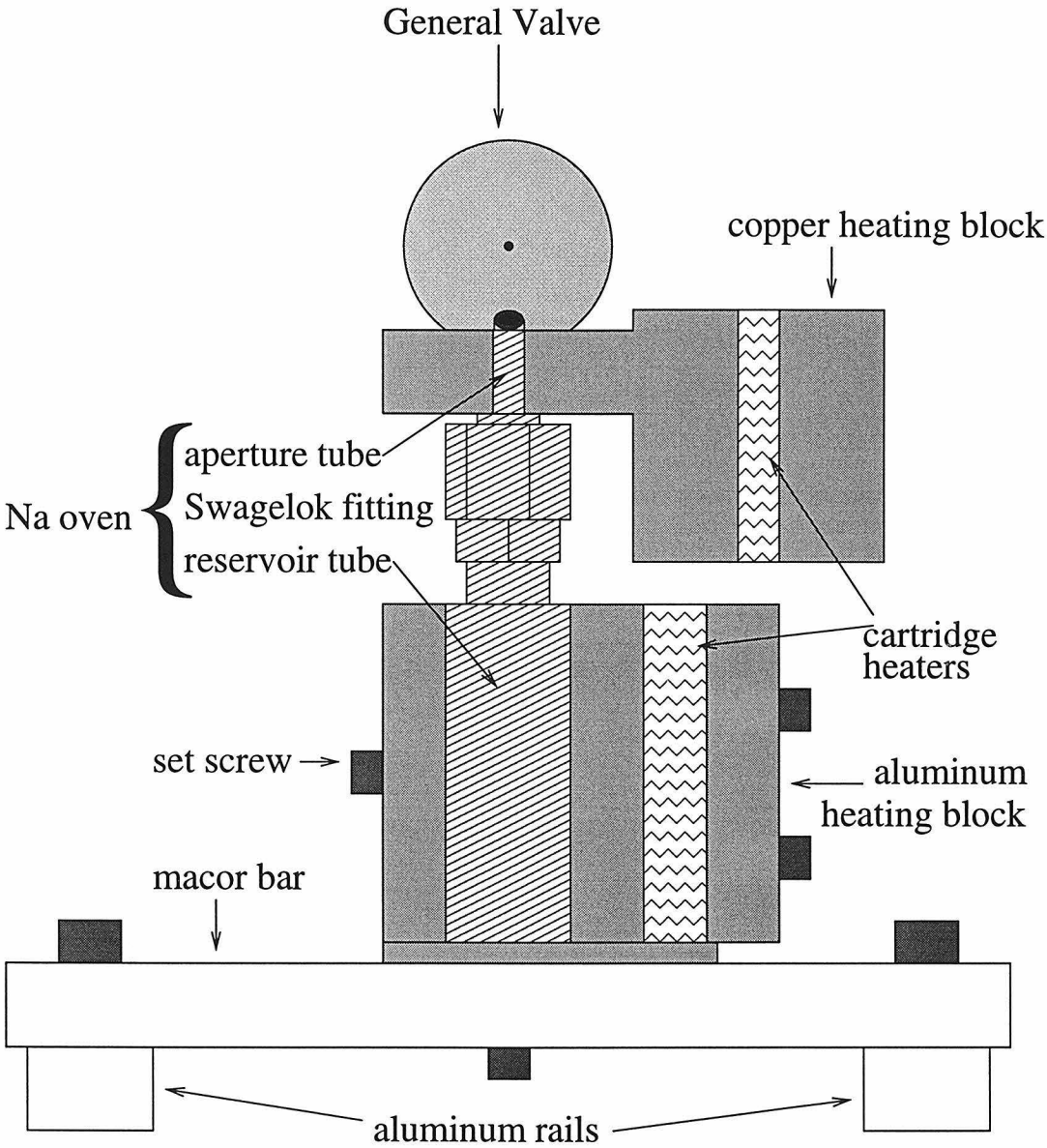
General Valve
copper heating block
Na oven
aperture tube
Swagelok fitting
reservoir tube
cartridge
heaters
set screw
aluminum
heating block
macor bar
aluminum rails

obtained by minimizing the flow through the pulsed valve. This was done by keeping the voltage applied to the valve as low as possible. The number of 1:1 complexes ionized per laser shot was ~250.

For complexes with water, the argon carrier gas was passed through a water reservoir behind the General Valve. The reservoir and valve were independently heated in the same manner as the sodium oven, described below, with the valve being kept hotter than the reservoir. When the sodium oven was on, it alone heated the valve, the face of which was covered with aluminum foil, to a temperature over 100° C. The carrier gas tubing leading into the reservoir was Teflon, which thermally isolated the reservoir from the chamber.

2.4.3 The Sodium Oven

The stainless steel sodium oven consisted of two parts, the reservoir and the aperture tube, which were connected by a Swagelok fitting. The reservoir was made by drilling a 12 mm diameter hole in a rod 0.75″ in diameter and 2″ long, and welding a Swagelok fitting (0.375″ diameter) to it. The aperture tube was made from a 0.375″ diameter rod which fit into the Swagelok connector. The lower half of the tube had an o.d. of 0.375″ and an i.d. of 0.290″, while the rest of the tube had an o.d. of 0.173″ and an i.d. of 0.125″. The tip was ground at an angle to minimize obstruction of the gas flow from the pulsed General Valve.

The oven's reservoir and aperture tube were heated independently with cartridge resistance heaters (Omega). The sodium reservoir was placed in a hole in an aluminum block, onto which a 0.375″ o.d. cartridge heater (200W) was clamped by another piece of aluminum, in a carefully-reamed 0.375″ diameter hole. The aperture tube was clamped in a hole between two copper plates, as was a 0.25″ diameter cartridge heater (150 W). The oven was supported by a macor bar to prevent heat conduction to the chamber.

In typical sodium ovens having much smaller apertures, the aperture must be kept hotter than the reservoir to prevent clogging. While clogging of our large-aperture

oven was not a problem, the aperture was kept ~20° C hotter than the reservoir to keep the part of the oven not in contact with either heating block from getting too cold. Typically, the reservoir was held at 365° C (Na vapor pressure 0.1 Torr) and the aperture at 385° C. This gave ~10 hours of stable operation when the oven was filled. The temperatures were maintained by temperature controllers from Omega (model CN76133). The cartridge heater for each heating block was connected to a controller via an electrical feedthrough, and a chromel-alumel thermocouple was attached to the block, with its wires connected to the temperature controller via a thermocouple feedthrough.

Finally, a bit of advice on preventing heater burnout. The heater block must make contact with as much of the cartridge as possible, or the cartridge will overheat in spots and burn out. The cartridge hole should be reamed. Also, one must ensure that the heating block has enough mass to carry heat away from the cartridge. Small heating blocks lead to burnout. Lastly, the temperature should be turned up slowly (10-20° C intervals every few minutes) because the temperature will usually overshoot the new setting and create a hot spot near the cartridge, resulting in burnout.

2.4.4 The ZEKE-PFI Apparatus

The heart of the ZEKE-PFI apparatus, a drawing of which is shown in Figure 2.5, consisted of extraction grids, a μ-metal flight tube, and an MCP detector. The extraction grids were the same as those used in the TOFMS, but the electrons were extracted in the direction opposite to the TOFMS. A third grid was placed 3 mm outside the extraction region to provide additional acceleration for the electrons. A μ-metal flight tube was attached to the ion source to provide shielding against magnetic fields. Finally, the MCP detector was placed on a flange attached to the probe chamber, directly opposite the TOFMS.

Grid B was held at ground, while grid A was connected to the voltage pulse circuit. The pulse circuit, a schematic of which is shown in Figure 2.6, was an inverting amplifier containing a CLC 400 op amp. Typically, a -4 V output pulse 10 μs long

Figure 2.5: Schematic of the ZEKE-PFI apparatus.

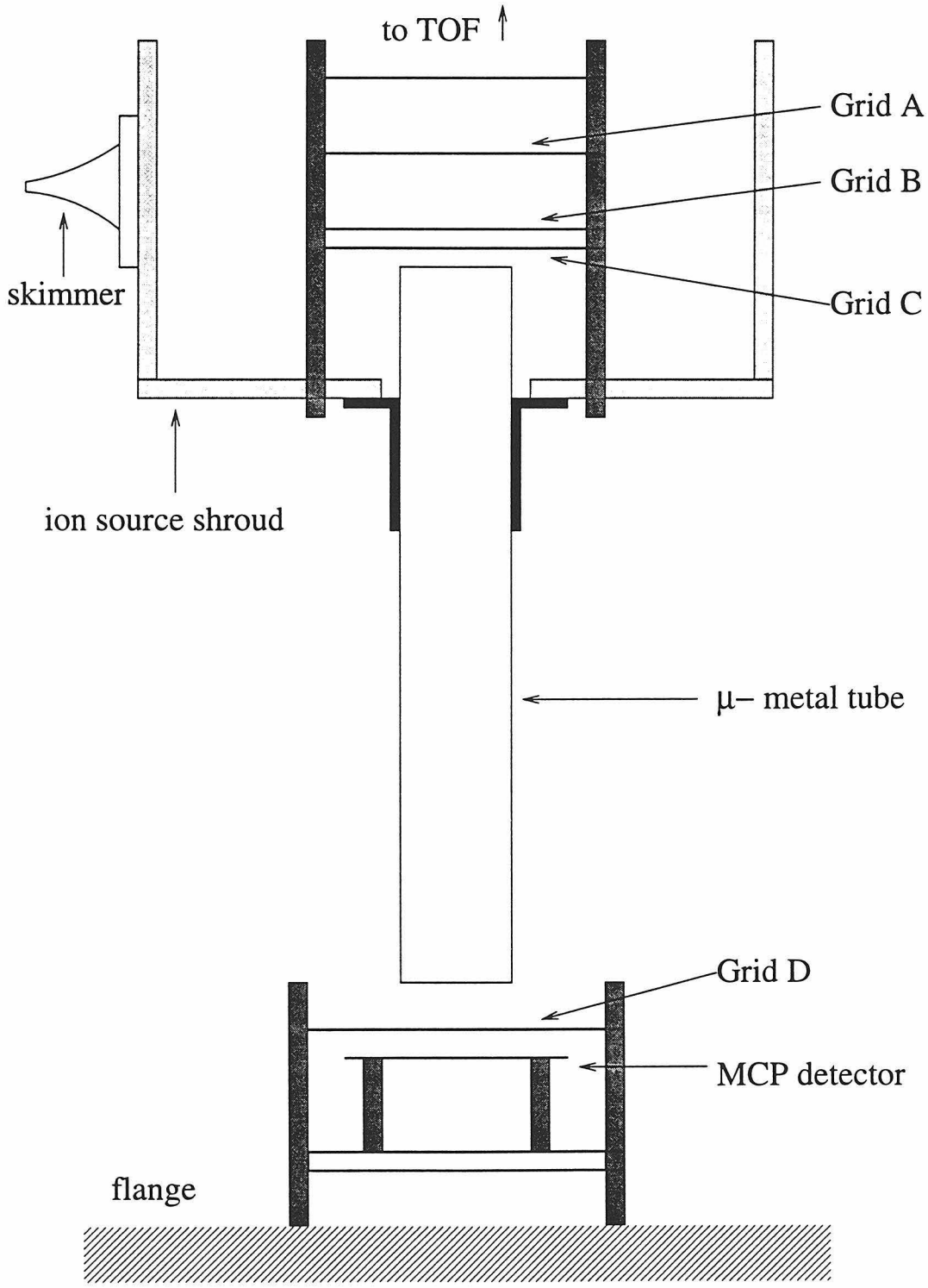
to TOF
Grid A
Grid B
Grid C
skimmer
ion source shroud
μ– metal tube
Grid D
MCP detector
flange

and having a risetime of ~80 ns was used in the experiments, but by selecting different resistors for the circuit, smaller pulses were generated. The offset null of the op amp was used to keep the grid as close to ground as possible when no pulse was applied. Grid C, 3 mm from grid B, was held at a potential of 9 V (provided by batteries) to give the electrons additional acceleration. The μ-metal flight tube was held at this same potential. Grid D, just in front of the detector, was floated because this increased the signal by a factor of ~2. Initially, a set of deflector plates was attached where grid C is, to ensure that the electrons hit the detector. This was later found to be unnecessary. We achieved an excellent S/N ratio with the present arrangement, but it could be improved by using either deflector plates or voltage pulses on grid C to eliminate interference from kinetic electrons.

High voltage for the dual MCP detector was provided by a Stanford Research Systems PS 325 power supply. The output of the supply, typically 1800-2000 V, was connected to a voltage divider circuit, a schematic of which is shown in Figure 2.7b, so the appropriate potential difference would be placed across each MCP. The maximum input voltage is 2400 V, at which the voltage across each MCP is 1000 V, the highest allowed value, and the current is 400 μA. The potential difference of 400 V between grid D and the first MCP gives the ZEKE-PFI electrons sufficient energy to generate secondary electrons when they strike the MCP. As it is important that the resistors in the circuit be rated for the voltages across them, high-voltage resistors from Caddock were used. Finally, the voltage should be applied to the MCPs slowly (100 V steps) so as not to damage them.

The anode was held at a potential 200-300 V higher than the last MCP to ensure that the secondary electrons would hit it. This was done by connecting the anode via a low-pass filter to the VR1 output of the Jordan Co. TOFMS power supply and applying the correct voltage. Since this voltage is too high to connect to the oscilloscope, a high-pass filter was employed so only the ac signal would reach the processing electronics. The circuit is shown in Figure 2.7a. Mica capacitors, rated for 3000 V, were used because they perform well at high frequency.

When the operating voltages are applied to the ZEKE-PFI apparatus, ZEKE-PFI

Figure 2.6: (a) Schematic of the circuit used to generate negative voltage pulses in ZEKE-PFI experiments. (b) Timing of the pulsed electric field relative to the time at which the laser intersects the molecular beam.

(a)

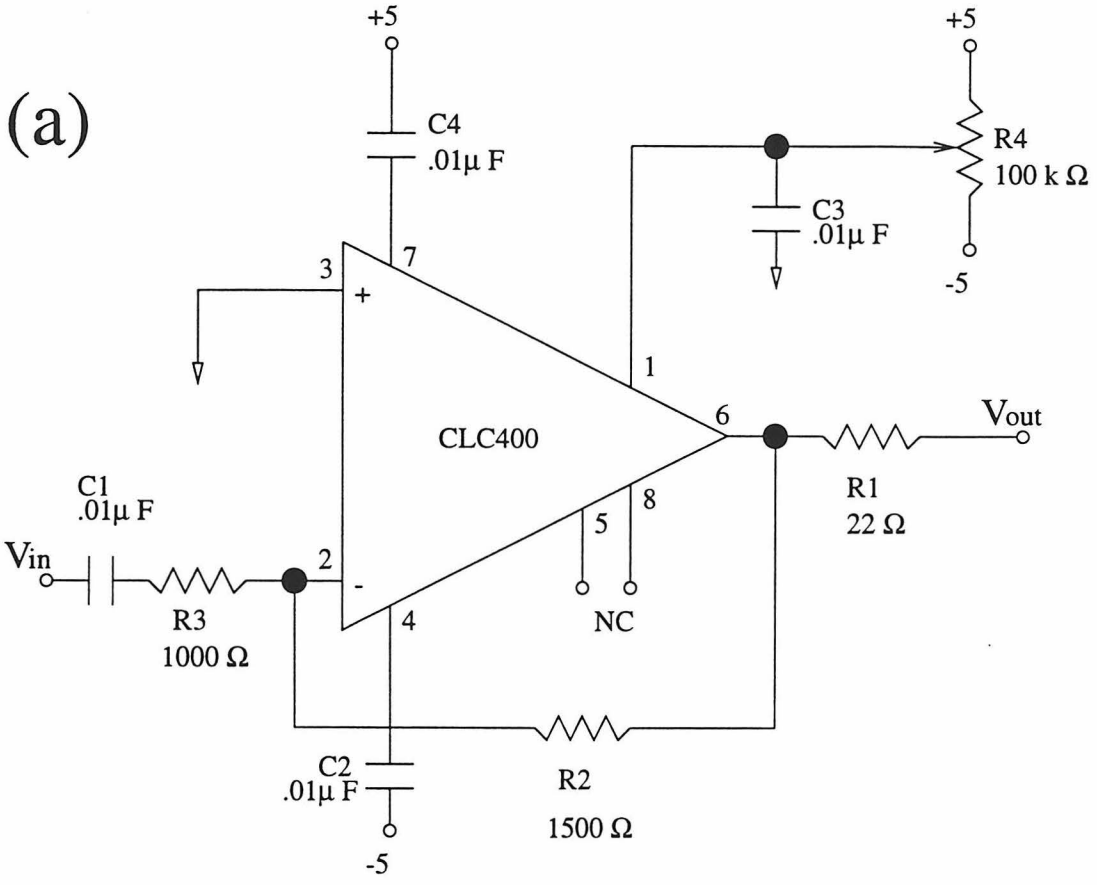
+5
C4
.01µ F
+5
R4
100 k Ω
C3
.01µ F
-5
3
7
+
1
6
Vout
CLC400
C1
.01µ F
5
8
R1
22 Ω
Vin
2
-
R3
1000 Ω
4
NC
C2
.01µ F
R2
1500 Ω
-5

(b)

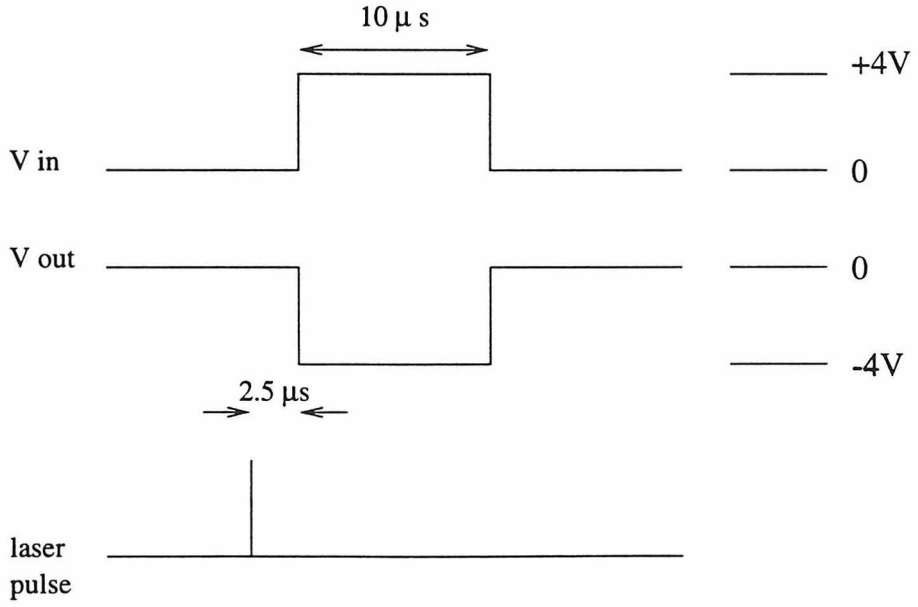
10 µ s
+4V
V in
0
V out
0
-4V
2.5 µs
laser
pulse

electrons, or immediate electrons, for that matter, are not initially observable because of stray charge build-up on the apparatus, especially after operating the TOFMS. The procedure for removing the stray charge is given in Appendix B. After following this procedure, the signal, an oscilloscope trace of which is shown in Figure 2.8, is stable, but the S/N ratio sometimes improves after a few hours of use.

2.4.5 Lasers and Optics

In the ZEKE-PFI experiments, a Nd:YAG laser (Continuum YG 681) pumped one or two Fl 3002E dye lasers at 30 Hz. One dye laser, which used Coumarin 540A dye pumped by the 3rd harmonic of the Nd:YAG, was used in the single-photon experiments, its fundamental output frequency doubled with a BBO crystal. The fundamental output obtained from this dye laser, now using Coumarin 460 dye, was employed in the second excitation step in the two-color experiments. The other dye laser, which utilized Styryl 9 dye pumped by the 2nd harmonic of the Nd:YAG, supplied the first photon in the two-color experiments. The excitation laser beam entered the ionization region via a sapphire window on the top of the chamber, while the ionizing laser beam entered through a sapphire window at the end of the chamber, along the molecular beam axis. No focusing optics were used. The wavelengths of the dye lasers were calibrated with a wavemeter (Burleigh WA-4500A) and corrected to their vacuum values. Peak heights were not corrected for the variations of laser power with wavelength, which were sometimes large. A schematic of the entire ZEKE-PFI experimental apparatus is shown in Figure 2.9

2.5 Data Acquisition and Laser Scanning

The data collection procedure involved stepping a dye laser's frequency, averaging the ion or electron signal from a few hundred laser shots with a digital oscilloscope (LeCroy 9400A), and transferring the data to a personal computer (PC, from Compaq) for further processing. The laser scanning and oscilloscope were controlled by

Figure 2.7: (a) Schematic of the filter circuits connected to the anode in ZEKE-PFI experiments. (b) Schematic of the voltage divider circuit used to apply the correct voltages to the MCP detectors in ZEKE-PFI experiments.

(a)

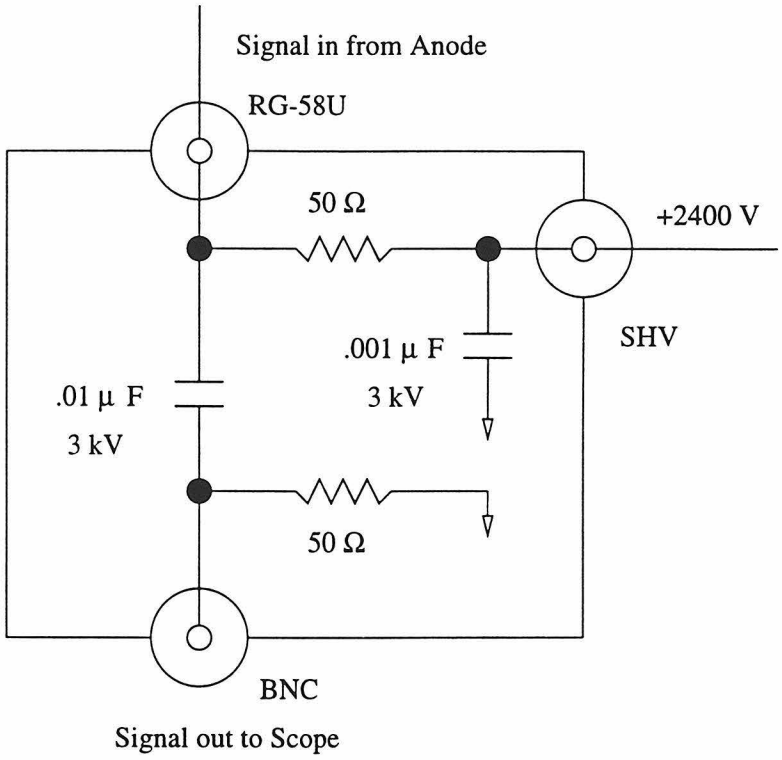
Signal in from Anode
RG-58U
50 Ω
+2400 V
SHV
.001 μ F
3 kV
.01 μ F
3 kV
50 Ω
BNC
Signal out to Scope

(b)

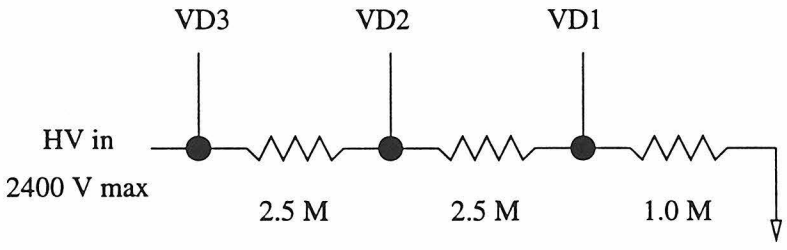
VD3
VD2
VD1
HV in
2400 V max
2.5 M
2.5 M
1.0 M

Figure 2.8: Oscilloscope traces of (A) ZEKE-PFI signal and (B) the leading edge of the voltage pulse used to create the pulsed electric field.

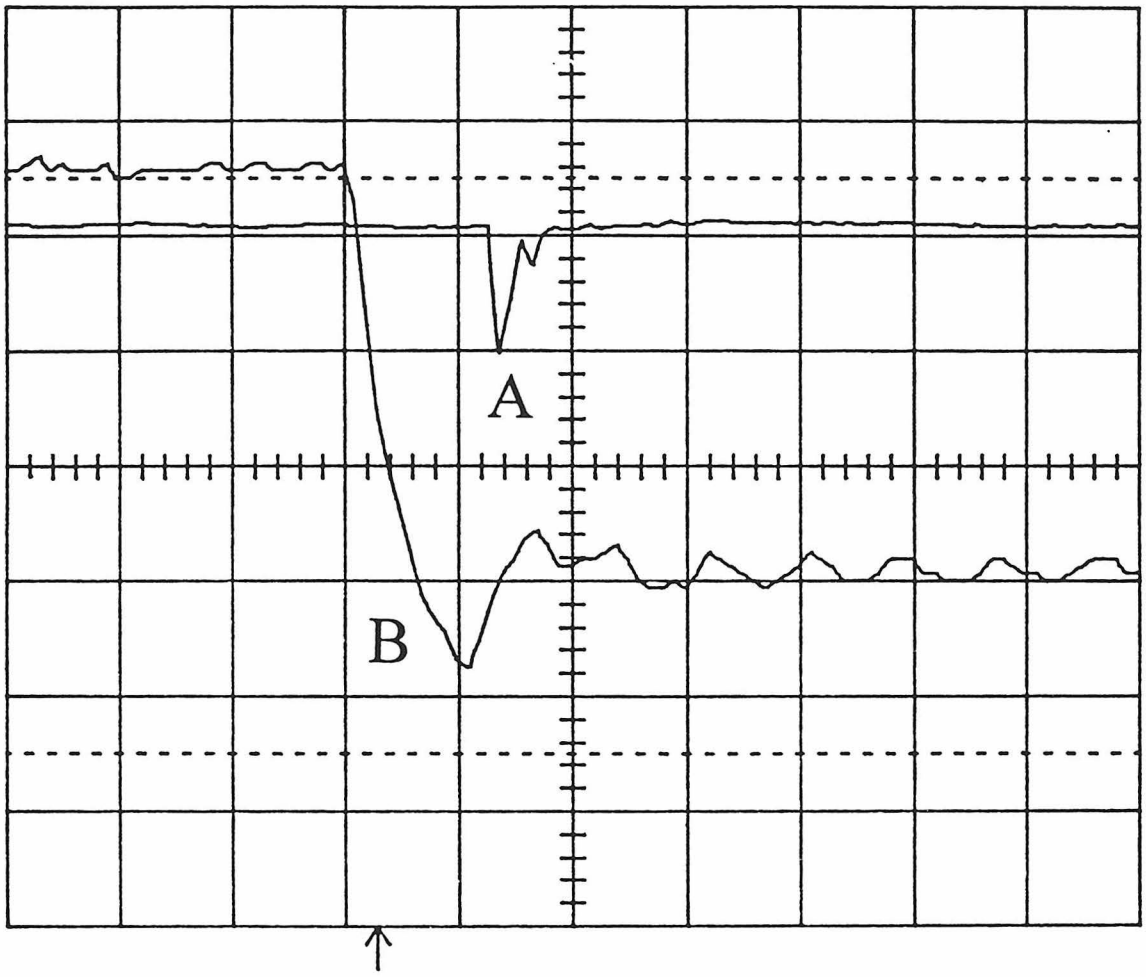

Ch 1 2 V =
T/div .1 µs Ch 2 20 mV 50 Ω

Figure 2.9: Schematic of the complete experimental apparatus used in ZEKE-PFI experiments on $Na(H_2O)$ and $Na(NH_3)$.

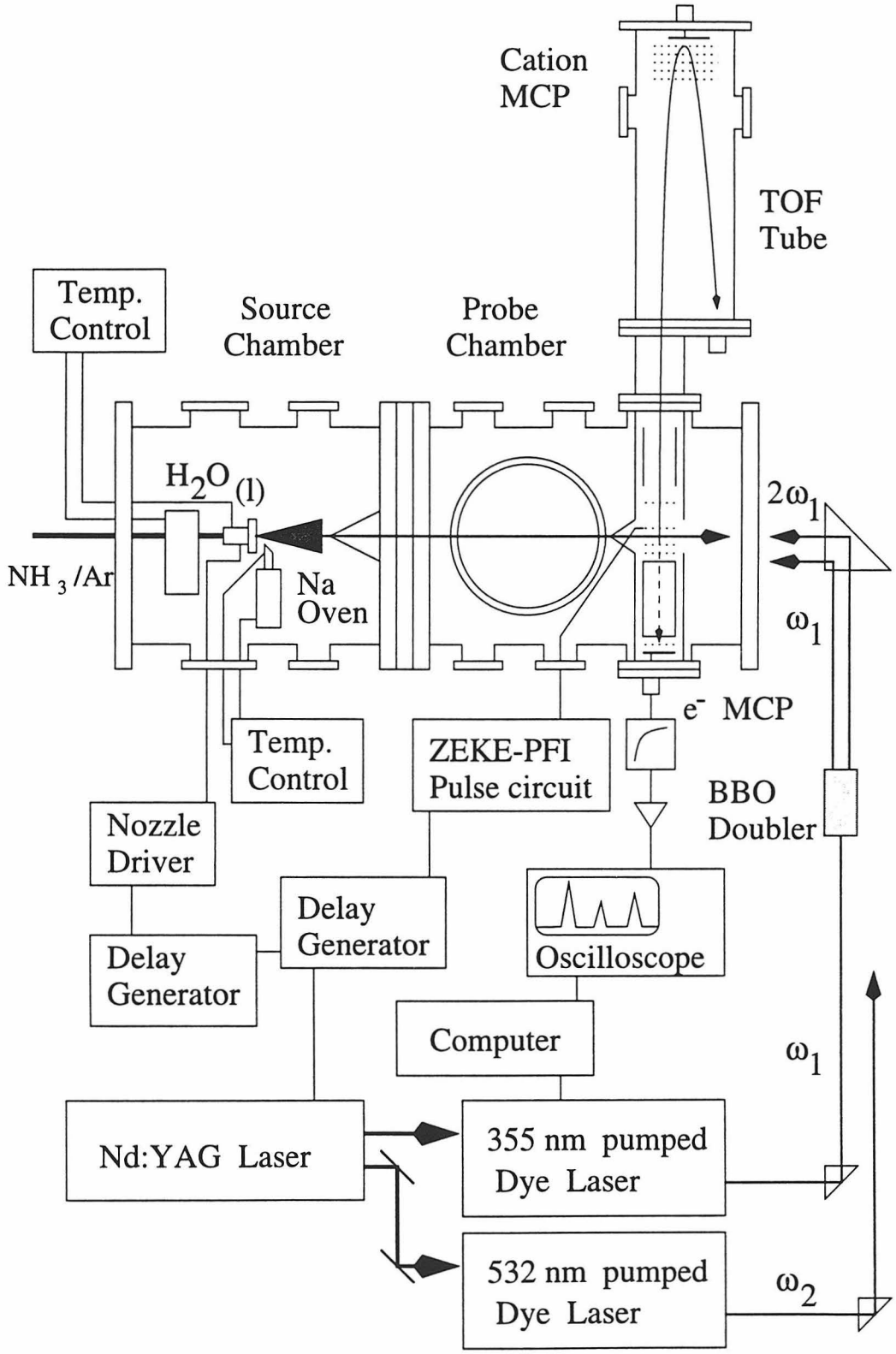
Cation
MCP
TOF
Tube
Temp.
Control
Source
Chamber
Probe
Chamber
$H_2O_{(l)}$
$2\omega_1$
NH_3 /Ar
Na
Oven
ω_1
e^- MCP
Temp.
Control
ZEKE-PFI
Pulse circuit
BBO
Doubler
Nozzle
Driver
Delay
Generator
Oscilloscope
Delay
Generator
Computer
ω_1
Nd:YAG Laser
355 nm pumped
Dye Laser
532 nm pumped
Dye Laser
ω_2

the PC, with communication between devices conducted via a GPIB bus (National Instruments). The data collection software is listed in Appendix B.

The method by which the laser frequency, doubling crystal position, and etalon position were scanned under computer control is described in the Lambda Physik manual. The doubling crystal angle as a function of wavelength may be described by a function given in the manual, but this was not used. Instead, several calibration points were taken over the scan range and entered into the program, with linear interpolation used between the points.

The amplified signal was connected to the oscilloscope with 50 Ω termination and was digitized at 10 ns intervals. The oscilloscope was triggered by the signal from a photodiode in mass spectrometry experiments, and by the ionization voltage pulse in ZEKE-PFI experiments. The signal was averaged in function E or F on the oscilloscope. Data processing on the PC involved adding the points in the signal peak and subtracting the background. In mass spectrometry experiments, the program located and processed the peaks for any desired number of masses, while in ZEKE-PFI experiments or REMPI studies in which only one time (mass) was of interest, the single peak was processed. The processed data was stored in a file on the PC's hard drive, and, for most experiments, the entire oscilloscope waveform at each laser step was stored as well.

A digital delay generator (SRS DG-535) served to synchronize the laser pulses with the molecular beam pulses. This was very straightforward in the benzene-ammonia R2PI experiments, since the excimer laser and pulsed valve driver could each be externally triggered with 5V TTL pulses. Synchronization in the ZEKE-PFI experiments was a bit more involved and required two DG-535 delay generators. The General Valve driver circuit did not work well when externally triggered (see Appendix B), so it was operated in an internal trigger mode at 30 Hz, and was used to control the timing sequence. The valve driver triggered a DG-535 which, after the appropriate delay, triggered another DG-535 which in turn triggered the Nd:YAG laser and the ZEKE-PFI pulse circuit.

Bibliography

[1] R.E. Smalley, L. Wharton, and D.H. Levy, *Acc. Chem. Res.*, 10:139, 1977.

[2] R.E. Smalley, D.H. Levy, and L. Wharton, *J. Chem. Phys.*, 64:3266, 1976.

[3] V.I. Karataev, B.A. Mamyrin, and D.V. Shmikk, *Sov. Phys.-Tech. Phys.*, 16:1177, 1972.

[4] B.A. Mamyrin, V.I. Karataev, D.V. Shmikk, and V.A. Zagulin, *Sov. Phys.-JETP*, 37:45, 1973.

[5] W.C. Wiley and I.H. McLaren, *Rev. Sci. Instrum.*, 26:1150, 1955.

[6] J.H. Callomon, T.M. Dunn, and I.M. Mills, *Phil. Trans. R. Soc. Lond.*, 259:499, 1966.

[7] E. Riedle, Th. Knittel, Th. Weber, and H.J. Neusser, *J. Chem. Phys.*, 91:4555, 1989.

[8] L.A. Chewter, M. Sander, K. Müller-Dethlefs, and E.W. Schlag, *J. Chem. Phys.*, 86:4737, 1987.

[9] K.G. Spears and S.A. Rice, *J. Chem. Phys.*, 55:5561, 1971.

[10] D. Proch and T. Trikl, *Rev. Sci. Instrum.*, 60:713, 1989.

[11] Matthew S. Johnson, *Spectroscopy of Reactive Molecules and Clusters*, Ph.D. thesis, California Institute of Technology, 1996.

[12] R.E. Bumgarner and G.A. Blake, *Chem. Phys. Letters*, 161:308, 1989.

[13] R.D. Suenram F.J. Lovas, G.T. Fraser, J.Z. Gillies, C.W. Gillies, and M. Onda, *J. Molec. Spectrosc.*, 137:127, 1989.

[14] Sakae Suzuki, *Towards a More Quantitative Understanding of Intermolecular Interactions: Biologically Significant Intermolecular Clusters*, Ph.D. thesis, California Institute of Technology, 1996.

[15] K. Müller-Dethlefs, M. Sander, and E.W. Schlag, *Z. Naturforsch.*, A39:1089, 1984.

[16] G. Reiser, W. Habenicht, K. Müller-Dethlefs, and E.W. Schlag, *Chem. Phys. Letters*, 152:119, 1988.

[17] K. Müller-Dethlefs and E.W. Schlag, *Ann. Rev. Phys. Chem.*, 42:109, 1991.

[18] R. Lindner, H.J. Dietrich and K. Müller-Dethlefs, *Chem. Phys. Letters*, 228:417, 1994.

[19] C.P. Schulz, R. Haugstätter, H.U. Tittes and I.V. Hertel, *Phys. Rev. Letters*, 57:1703, 1986.

[20] C. Nitsch, C.P. Schulz, A. Gerber, W. Zimmermann-Edling and I.V. Hertel, *Z. Physik D*, 22:651, 1992.

Chapter 3 Structure of the Benzene-Ammonia Dimer

3.1 Introduction

The results of R2PI-TOFMS and microwave spectroscopy experiments performed on the benzene-ammonia dimer in order to determine its suitability as a model of amino-aromatic hydrogen bonding in proteins will be presented in this chapter. R2PI-TOFMS experiments were done first because of the ability of this technique to verify the existence of the complex via mass spectrometry, and because this technique has high sensitivity as a result of zero-background ion-counting detection. This was very helpful because, compared to many other complexes, the benzene-ammonia complex is not formed in great numbers. Also, rapid scanning was possible because only moderate resolution was achievable with the dye laser that was used. Microwave spectroscopy was employed next because the high spectral resolution achievable in the microwave region allowed an accurate determination of the "structure" of the complex.

In the work presented here, the benzene molecule in the complex is ionized with R2PI using the S_1 state as the intermediate resonance. The transition to the doubly degenerate 6^1 level is a perpendicular transition, and the rotational constants of benzene in both the ground and S_1 6^1 states are well known [1]. In general, vibronic energy levels and IPs are not changed drastically when benzene forms a weakly bound complex [2], so the vibronic spectroscopy of the complex benzene-ammonia was nearly the same as for free benzene. However, the rotational structure of the vibronic transitions was changed dramatically, and it provided information on the structure of the complex.

R2PI-TOFMS experiments have previously been performed on the benzene-ammonia

complex by Bernstein's group [3]. However, their spectrum, obtained by recording the $C_6H_6{}^+(NH_3)$ ion signal, contained contributions from clusters of the form $C_6H_6(NH_3)_n$ as a result of fragmentation, rendering them unable to accurately identify the 6_0^1 transition of the benzene-ammonia dimer and determine its structure. The ability of the R2PI method to give structural information on similar complexes has been demonstrated in Zwier's study of the benzene-water complex [4]. They found that the water was located above the benzene plane, on the benzene C_6 axis, with a center of mass separation of 3.3 Å. The water was found to undergo free internal rotation, which allowed the complex to maintain high symmetry. Although much evidence supporting a structure in which the water acted as a proton donor was found, the spectral resolution was insufficient to determine the location of the water protons.

Prior to this work, no microwave experiments on the benzene-ammonia dimer had been reported. However, microwave and far-infrared spectroscopic studies of the benzene-water dimer have been done by the Blake group [5]. The microwave studies showed that this is a hydrogen-bonded complex, with the water located on the benzene C_6 axis, its protons pointing toward the benzene π-cloud and the water C_2 axis tilted 20° from the benzene C_6 axis. Further understanding of the IPES of this "floppy" complex was provided by the high resolution far-infrared absorption experiments, which to date have identified an intermolecular bending vibrational mode in $C_6H_6(D_2O)$ [6].

3.2 R2PI-TOFMS Results

When laser radiation with a wavelength of 260 nm intersected the molecular beam (benzene and ammonia seeded in helium) in the ionization region of the TOFMS, a mass spectrum such as that shown in Figure 3.1 was observed. The peak at 12.25 μs arises from $C_6H_6^+$, and the peaks at 13.52, 14.68, and 15.75 μs are $C_6H_6{}^+(NH_3)_n$ clusters with n= 1,2, and 3, respectively. The mass peaks of the clusters disappeared when either benzene or ammonia was removed from the gas mixture.

The peak corresponding to the $C_6H_6(NH_3)$ mass (95 mass units) was then mon-

Figure 3.1: Oscilloscope trace of the signal from the TOFMS showing clusters of ammonia with benzene.

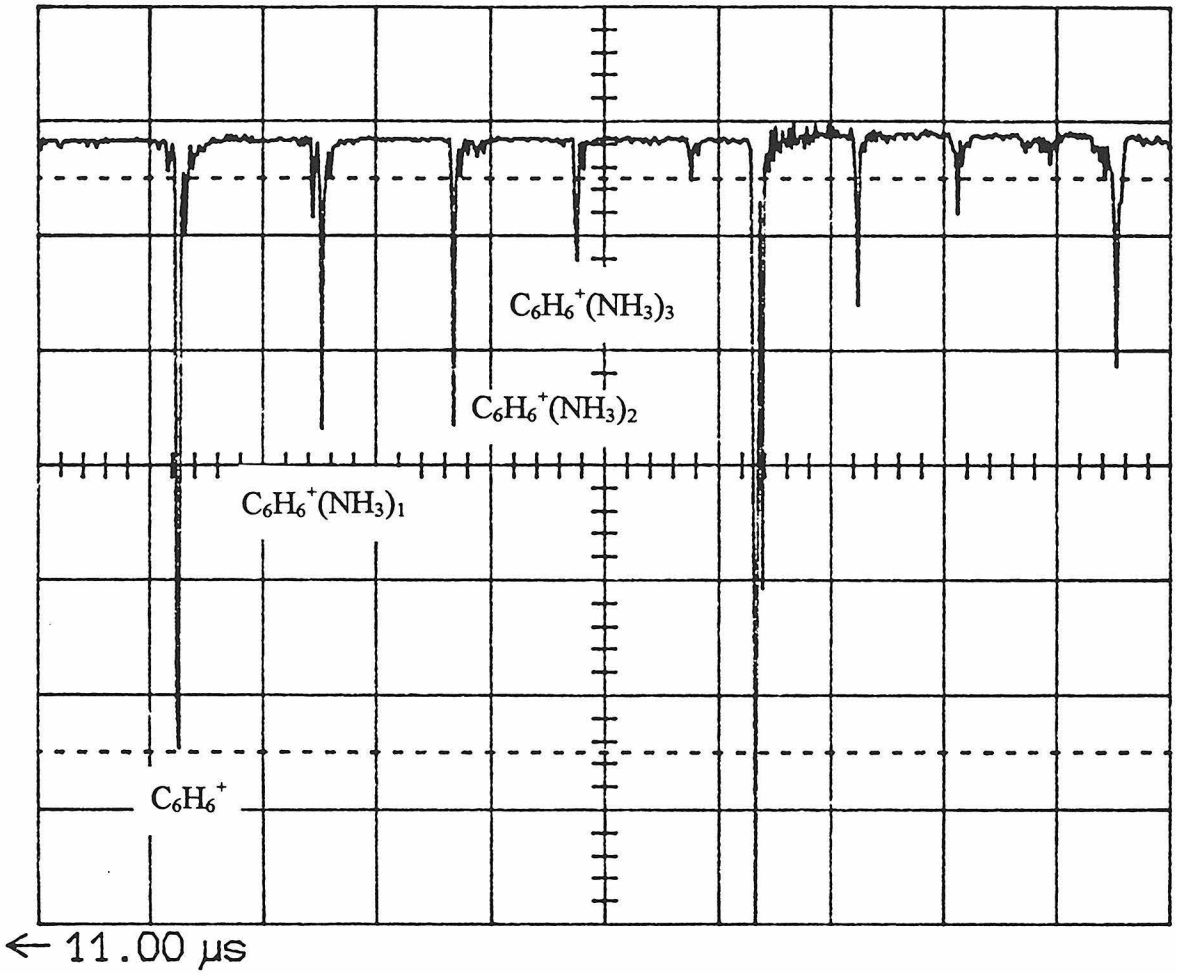
$C_6H_6^+(NH_3)_3$
$C_6H_6^+(NH_3)_2$
$C_6H_6^+(NH_3)_1$
$C_6H_6^+$
← 11.00 µs
Ch 1 10 mV ~
T/div 1 µs Ch 2 5 mV 50Ω

itored as a function of laser wavelength, resulting in the spectrum shown in Figure 3.2a. The structure is very broad and complex, similar to that observed by Bernstein. Since fragmentation of larger clusters can produce signal at the $C_6H_6(NH_3)$ mass, spectra were recorded at much lower ammonia concentrations to reduce the fragmentation signal. One such spectrum is shown in Figure 3.2b, where it can be seen that most of the signal disappeared, leaving primarily two strong peaks located 52.5 and 56.25 cm^{-1} higher in energy than the benzene 6_0^1 transition. There is possibly a third peak 44.25 cm^{-1} above the benzene 6_0^1 transition. These peaks are assigned to the 6_0^1 transition of the benzene in the benzene-ammonia dimer.

Peaks that appear at these same positions are also prominent in the spectrum of the benzene mass channel (78 mass units) shown in Figure 3.2c. They do not appear unless ammonia is in the beam. This gives additional support to the assignment of these peaks to the benzene-ammonia dimer, since larger clusters would probably lose an ammonia molecule, not the benzene cation, in the fragmentation process.

The fragmentation of the 1:1 complex following ionization is evidence of a hydrogen bonded structure. The partially positive hydrogens, adjacent to the benzene ring, are repelled by the $C_6H_6^+$ ion. This is consistent with the results of Zwier, who observed efficient (80%) fragmentation of the benzene-water complex [4]. While the neutral complex may have a hydrogen bonded structure, the most stable structure in the ionized complex has the ammonia nitrogen, not the protons, pointing toward the benzene. Because of this large geometry change the ionizing photon placed the complexes in highly vibrationally excited states with up to 2000 cm^{-1} of internal energy. Attempts to reduce the fragmentation by using two-color ionization to limit the amount of internal energy available to the ionized complex were unsuccessful, since the large geometry change between the neutral complex and the ionized complex results in a small Franck-Condon factor for ionization to the ground vibrational state of the cation.

The spectrum in Figure 3.2b shows a short progression in a van der Waals mode of the complex, which has a frequency of $\sim$35 cm^{-1}. Although this mode cannot be identified at this time, its frequency is comparable to the frequencies of the van

Figure 3.2: Signal observed in the $C_6H_6(NH_3)$ and C_6H_6 mass channels as the laser frequency was scanned in the region of the 6_0^1 transition of free benzene (this occurs at 0 cm^{-1} on the horizontal axis). (a) Signal in the $C_6H_6(NH_3)$ mass channel with a benzene concentration of 0.2% and an ammonia concentration of 0.27%. (b) Signal in the $C_6H_6(NH_3)$ mass channel with a benzene concentration of 0.2% and an ammonia concentration of 0.007%. (c) Signal in the benzene mass channel with conditions the same as in (a). The arrows designate the peaks assigned to the 6_0^1 transition of the $C_6H_6(NH_3)$ complex.

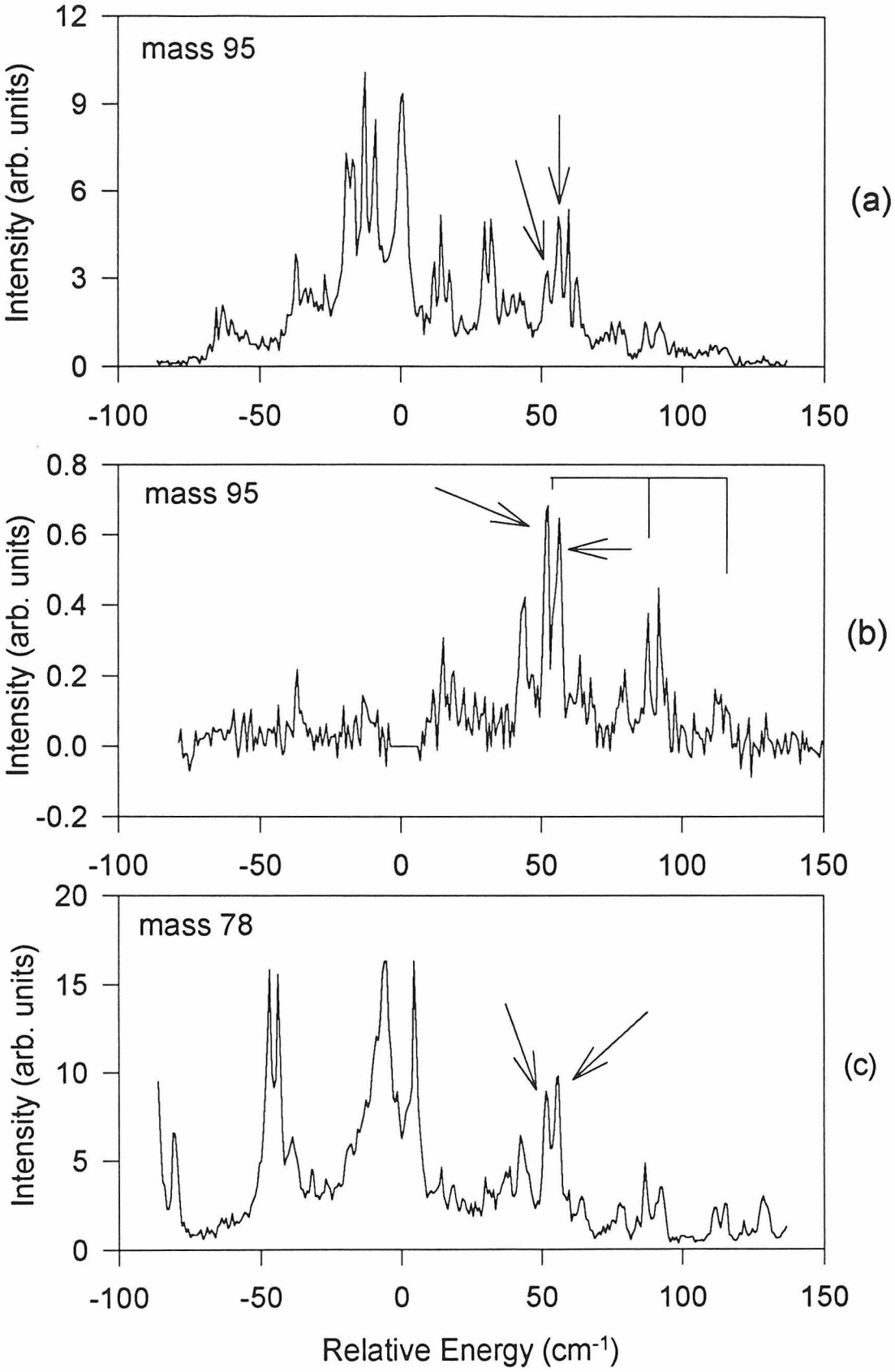
mass 95
Intensity (arb. units)
12
9
6
3
0
-100
-50
0
50
100
150
(a)
mass 95
Intensity (arb. units)
0.8
0.6
0.4
0.2
0.0
-0.2
(b)
mass 78
Intensity (arb. units)
20
15
10
5
0
(c)
Relative Energy (cm-1)

der Waals modes of the benzene-water complex which have been measured by R2PI, Raman, and far-IR spectroscopy [4, 7, 6].

Spectra of the benzene-ammonia 6_0^1 peaks taken with higher resolution (0.8 cm^{-1}) are shown in Figure 3.3a, while a spectrum of the same transition of $C_6H_6(ND_3)$ is shown in Figure 3.3b. The existence of two peaks rather than just one is believed to result from the metastable J=1, K=1 (E symmetry) rotational state of NH_3 (or ND_3). This rotational state cannot cool in the supersonic jet expansion to the J=0, K=0 (A symmetry) rotational state because the nuclear spin states associated with these rotational levels have different symmetries, and they are not interconverted in the supersonic expansion. When the rotationally excited NH_3 forms a complex, the rotation becomes either free or hindered internal rotation. If m is the quantum number for internal rotation, J=1,K=1 becomes the m=1 state, the m=0 state resulting from complexation of ground state NH_3. R2PI spectra of benzene-water also showed two peaks for the 6_0^1 transition, one produced by the analogous metastable rotational level of water complexing to form the m=1 internal rotor state, and the other corresponding to the m=0 state [4]. The selection rule in the transitions of concern here is Δm=0 [4], and two peaks result because the internal rotation in the m=1 state slightly changes the energetics of the interaction with benzene due to the anisotropy of the IPES.

A spectrum of the free benzene 6_0^1 transition is shown in Figure 3.4a. The strongest peaks result from transitions involving the lowest rotational levels allowed by symmetry restrictions [8]. These transitions are labeled in the figure. The structure of the corresponding transition of the benzene-ammonia dimer is very similar to that of the free benzene transition, showing three strong peaks in the R branch, a Q branch, and two peaks in the P branch. The fact that the complex's transition has the same general structure as the free benzene transition is strong evidence that the complex has C_6 symmetry on a vibrationally averaged basis as a result of free internal rotation of the ammonia on the benzene C_6 axis.

Due to their limited resolution, these spectra cannot give an accurate structure for the complex. However, rotational band contour analysis was performed to verify general structural features, such as the location of NH_3 above the benzene plane and

Figure 3.3: R2PI spectra of the 6_0^1 transition of (a) $C_6H_6(NH_3)$ and (b) $C_6H_6(ND_3)$.

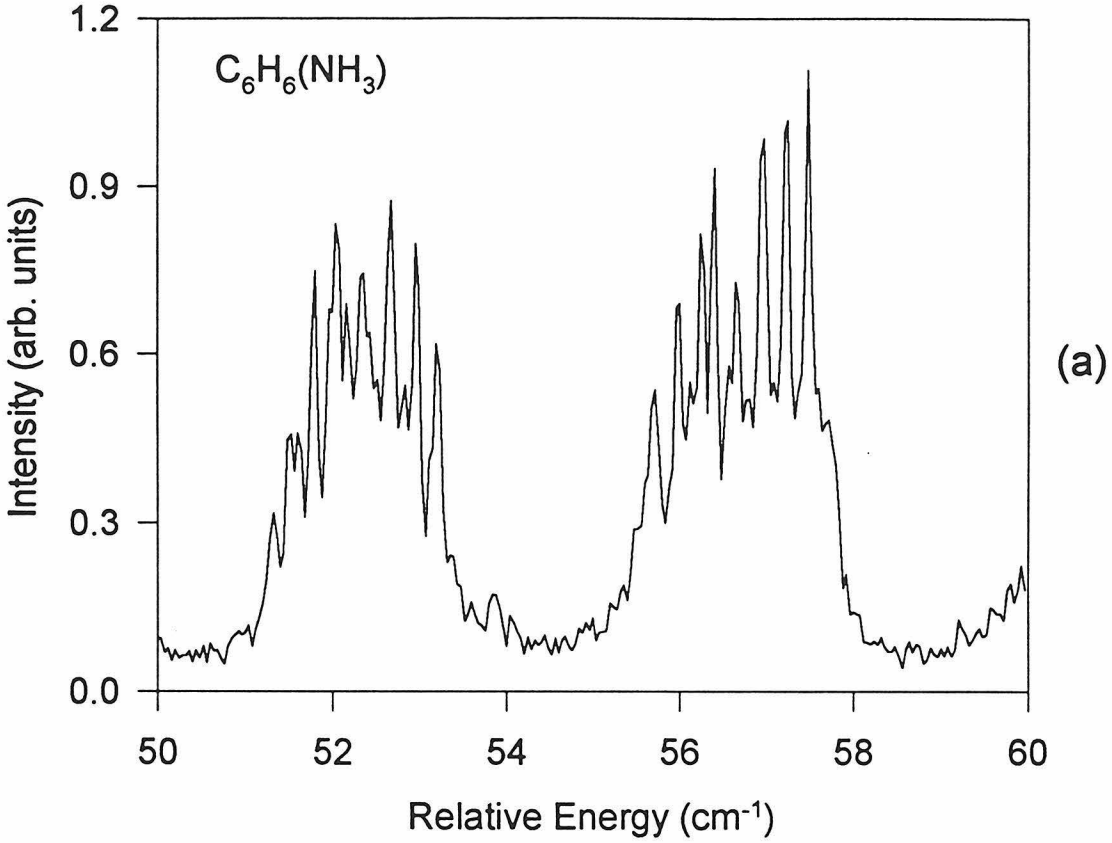
C6H6(NH3)
Intensity (arb. units)
1.2
0.9
0.6
0.3
0.0
50
52
54
56
58
60
Relative Energy (cm-1)
(a)

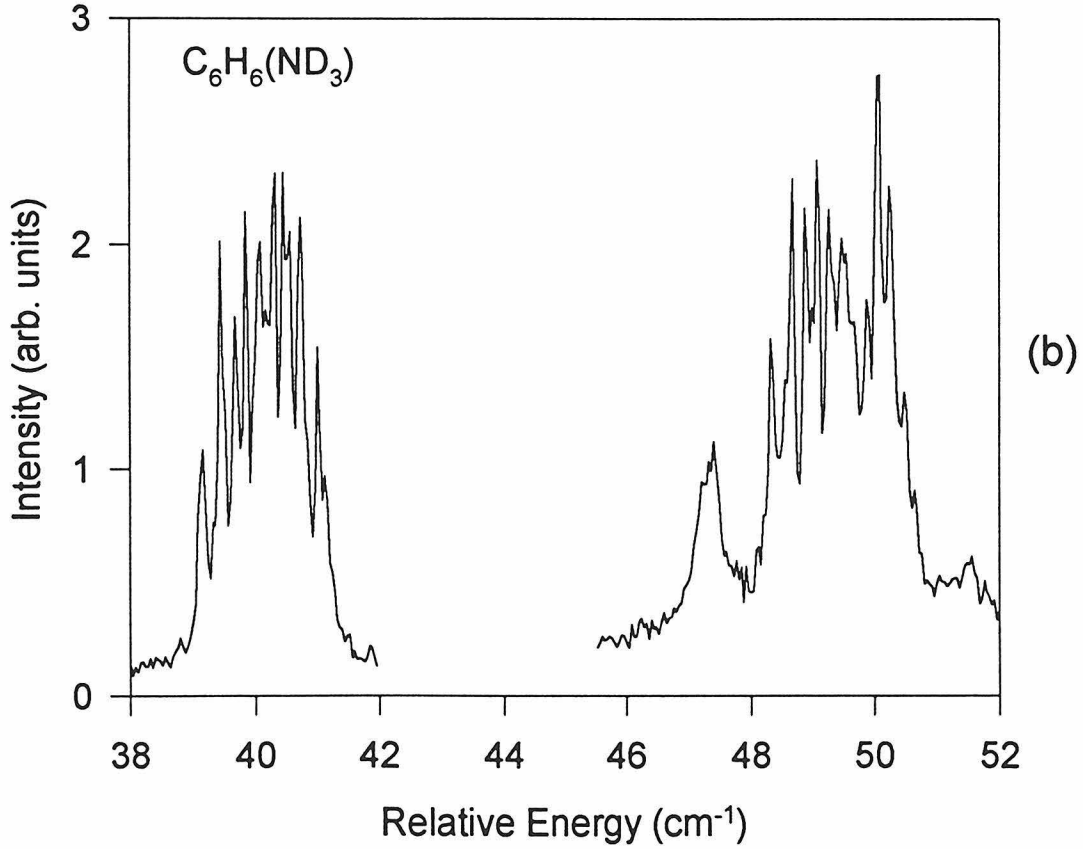
C6H6(ND3)
Intensity (arb. units)
3
2
1
0
38
40
42
44
46
48
50
52
Relative Energy (cm-1)
(b)

Figure 3.4: (a) R2PI spectrum of the 6_0^1 transition of C_6H_6. The labels of the transitions most responsible for the major peaks are given in the form ${}^{\Delta K}\Delta J_K^{(J)}$ where K and J are the quantum numbers of rotational angular momentum. (b) Experimental and calculated R2PI spectra of the 6_0^1 transition of $C_6H_6(NH_3)$.

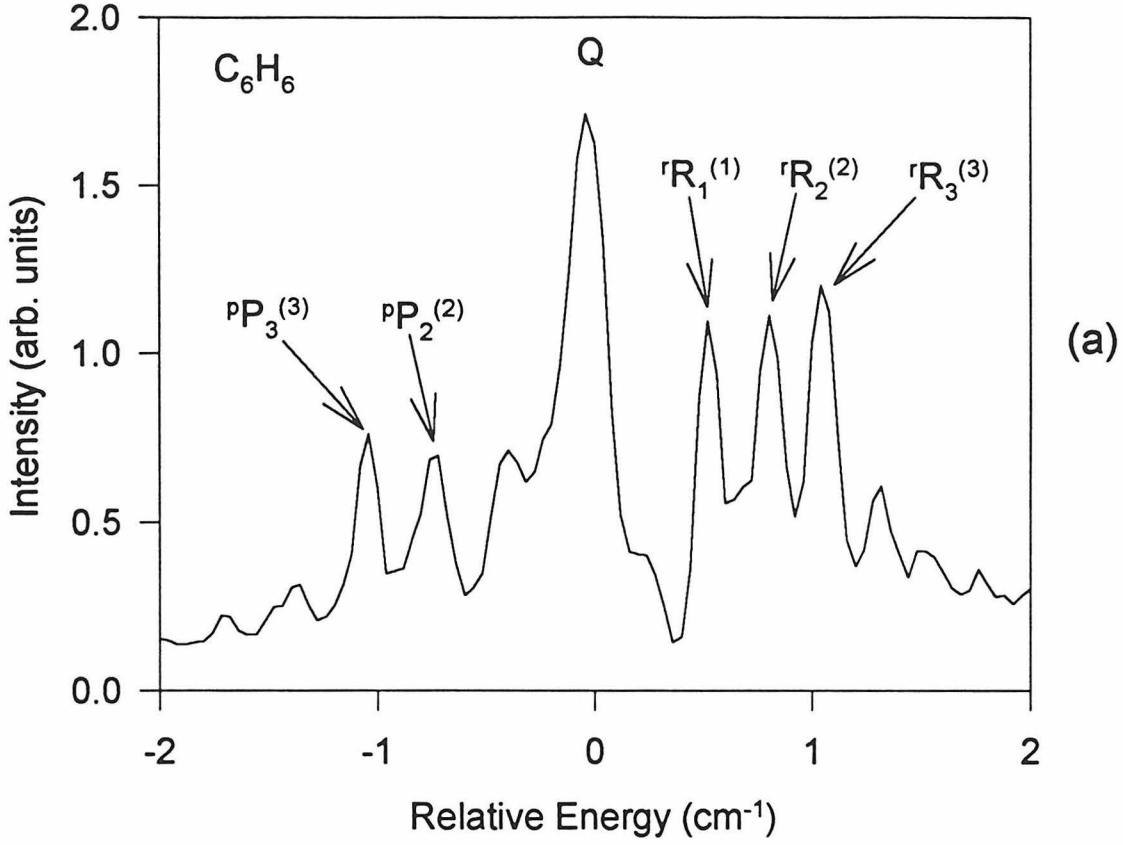
2.0
1.5
1.0
0.5
0.0
Intensity (arb. units)
C6H6
Q
rR1(1)
rR2(2)
rR3(3)
pP3(3)
pP2(2)
-2
-1
0
1
2
Relative Energy (cm-1)

(a)

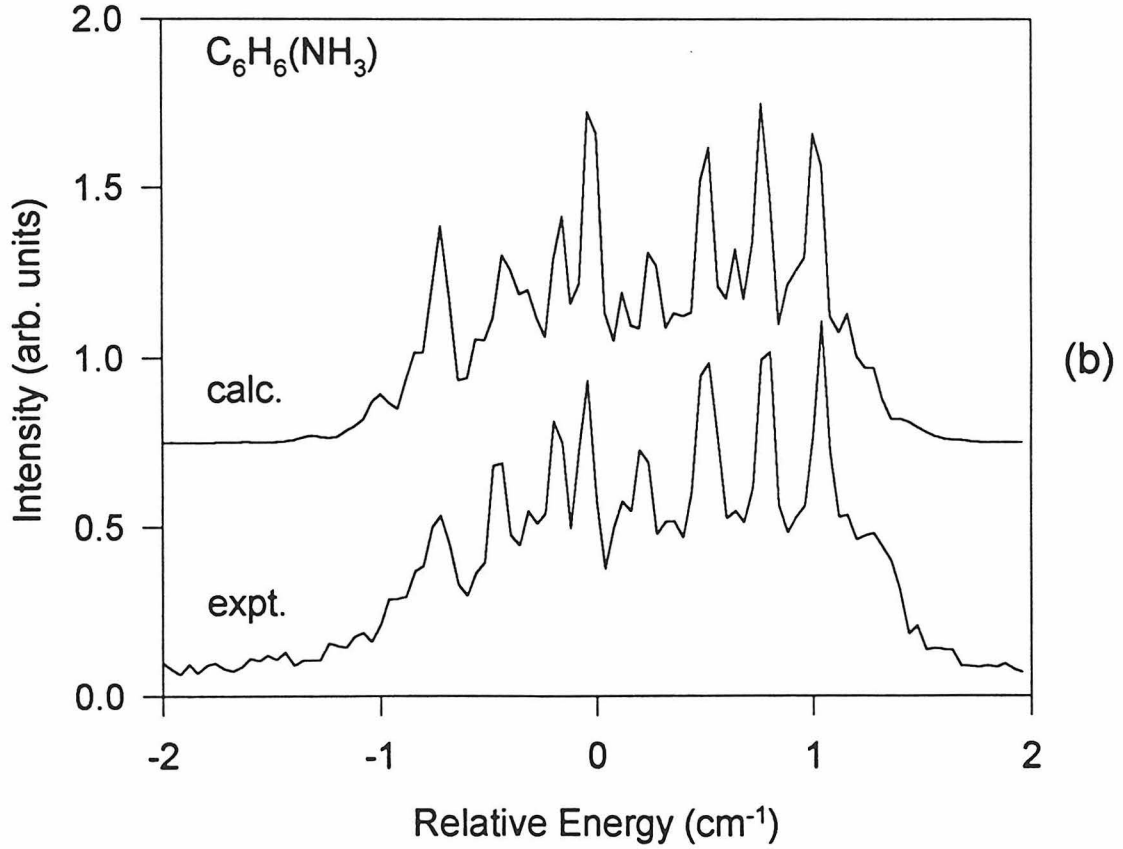
2.0
1.5
1.0
0.5
0.0
Intensity (arb. units)
C6H6(NH3)
calc.
expt.
-2
-1
0
1
2
Relative Energy (cm-1)

(b)

Table 3.1: Nuclear spin statistical weights of $C_6H_6(^{14}NH_3)$.

Rotational State	Γ_{rot}	m=0	m=±1
k=0,J even	A_1	40	44
k=0, J odd	A_2	40	44
k=6q±1	E_5	88	76
k=6q±2	E_6	72	100
k=6q±3	$B_1 + B_2$	112	72
k=6q±6	$A_1 + A_2$	80	88

the existence of free internal rotation. Unfortunately, the ammonia protons cannot be located at this level of resolution, and verification of hydrogen bonding must be addressed by the microwave work which follows.

Due to the probable existence of free or nearly free internal rotation in the complex, the nuclear spin statistical weights used in the fitting were determined using the G_{36} molecular symmetry group [9]. In this group, rotations of the monomers about their symmetry axes are considered feasible, while rotations about their other axes, and inversion of ammonia, are not feasible. A more detailed discussion of the G_{36} molecular symmetry group and the calculation of the nuclear spin statistical weights is presented in Appendix A. The nuclear spin statistical weights of the benzene-ammonia rotational levels are given in Table 3.1.

One of the observed bands should correspond to the m=0 internal rotor state, and the standard symmetric top energy level expression

$$E = BJ(J+1) + (A_f - B)k^2 - 2\zeta k A_f \tag{3.1}$$

was used to fit this rotational contour [2]. A_f is the rotational constant of the benzene frame about its C_6 axis, and ζ is the coriolis coupling parameter for the 6^1 vibrational level in the S_1 state of the complex. If the internal rotation is free, the A_f rotational constant of the complex should be the same as the C rotational constant of free benzene. Using the C rotational constants for the S_0 and S_1 states of benzene, the S_0 B rotational constant determined from the microwave experiments described below,

Table 3.2: Spectroscopic constants of benzene-ammonia.

Complex	A′ (cm^{-1})	A″ (cm^{-1})	B′ (cm^{-1})	B″ (cm^{-1})	ζ
$C_6H_6(^{14}NH_3)$	0.0906	0.0948	0.0640	0.0630	-0.48
$C_6H_6(^{14}ND_3)$	0.0906	0.0948	0.0578	0.0578	-0.58

and selection rules appropriate for a perpendicular transition of a symmetric top, the rotational band contour shown in Figure 3.4b resulted. The fitted parameters were the S_1 B rotational constant and the S_1 6^1 Coriolis coupling parameter, which was expected to be nearly the same as that of free benzene. A rotational temperature of 1 K was used. All of the parameters used in the fitting are listed in Table 3.2. This fit is not unique, as different combinations of A′ and the Coriolis parameter can be used to fit the main peaks, and an adequate fit could be obtained with a range of B values. However, the fact that an excellent fit was obtained with the C rotational constants of free benzene and a Coriolis parameter close to that of benzene support a structure in which the ammonia resides above the benzene plane, on the C_6 axis, undergoing free or nearly free internal rotation.

3.3 Results of Microwave Experiments

In order to "locate" the ammonia protons, high resolution pure rotational microwave spectra of the complexes were taken. Spectra of the J=6←5 and J=7←6 transitions of $C_6H_6(^{14}NH_3)$ were taken with the Caltech Stark modulation microwave absorption spectrometer, which had a resolution of 1 MHz. A list of the lines is given in Table 3.3.

The transitions were fit with the standard symmetric top equation

$$\nu(J \rightarrow J-1) = 2J(B - D_{JK}K^2) - 4D_J J^3 \tag{3.2}$$

and the fitted parameters are shown in Table 3.4. If the ammonia protons are assumed to point toward the benzene π-cloud with the monomer symmetry axes collinear, an

Table 3.3: Frequencies of rotational transitions observed with DAMW spectroscopy for $C_6H_6(^{14}NH_3)$.

Transition (J',K' ← J'',K'')	Frequency (MHz)
6,1 ← 5,1	22663.74
6,2 ← 5,2	22660.50
6,3 ← 5,3	22654.98
6,4 ← 5,4	22647.30
6,5 ← 5,5	22637.42
7,2 ← 6,2	26435.70
7,3 ← 6,3	26429.26
7,4 ← 6,4	26420.30
7,5 ← 6,5	26408.74
7,6 ← 6,6	26394.70

Table 3.4: Spectroscopic fits to m = 0 microwave data

Complex	B(MHz)	D_J(kHz)	D_{JK}(kHz)	σ(MHz)
$C_6H_6(^{14}NH_3)$	1,889.026 (3)	4.03 (4)	91.52 (9)	0.038
$C_6H_6(^{15}NH_3)$	1,830.4272 (7)	3.87 (3)	89.50 (6)	0.003
$C_6H_6(^{14}ND_3)$	1,732.986 (7)	3.77 (3)	127.79 (51)	0.030

approximate value of R_{cm-cm} of 3.55 Å was obtained from the B rotational constant.

Based on predictions from this initial fit, spectra of the J=3←2 and J= 4←3 transitions of the C_6H_6-$^{14}NH_3$, -$^{15}NH_3$, and -^{14}ND3 isotopic species were taken with the FTMW instrument at NIST. The data were fit with the same symmetric top equation and the parameters determined thereby are found in Table 3.4. All of the transitions located thus far are in the m=0 internal rotor state. No m=1 transitions, such as the ones found for the benzene-water complex, have been found for the benzene-ammonia complex, but they are not needed in the structure determination. The isotope data allowed both R_{cm-cm} and θ to be determined from the following formula [10]:

$$I_{bb(C_6H_6-NH_3)} = \mu R^2_{(cm-cm)} + I_{bb(NH_3)}\langle 1 + cos^2\theta\rangle/2 + I_{cc(NH_3)}\langle sin^2\theta\rangle/2 + I_{bb(C_6H_6)} \quad (3.3)$$

Table 3.5: Frequencies of benzene-ammonia rotational transitions observed with FTMW spectroscopy (MHz).

Transition (J',K' ← J'',K'')	$C_6H_6(^{14}NH_3)$	$C_6H_6(^{15}NH_3)$	$C_6H_6(^{14}ND_3)$
3,0 ← 2,0	11333.713	10982.143	10397.520
3,1 ← 2,1	11333.153	10981.607	10396.773
3,2 ← 2,2	11331.492	10979.999	10394.406
4,0 ← 3,0	15111.130	14642.449	13862.910
4,1 ← 3,1	15110.440	14641.709	13861.890
4,2 ← 3,2	15108.223	14639.558	13858.865
4,3 ← 3,3	15104.563	14635.983	13853.723

I_{bb} is the moment of inertia of the designated molecule about its b axis, and I_{cc} is the moment of inertia about the c axis. μ is the pseudodiatomic reduced mass. Assuming that the distance from the nitrogen atom to the benzene plane R_{N-Bz} was the same for all three isotopic species led to independent constraints on R_{N-Bz} and θ, which were found to be $R_{N-Bz} = 3.590 \pm 0.005$ Å and $\theta = 59 \pm 5°$, as shown in Figure 3.5.

Additional structural information was obtained from the nuclear quadrupole coupling constant of the ammonia nitrogen and from the measured dipole moment of the complex. The J=3←2, K=2 transition was used to determine the a-axis projection of the quadrupole coupling constant. The hyperfine component transitions are given in Table 3.6. Using the formula

$$eQq_{aa} = eQq_{NH_3}\langle[3cos^2\theta - 1]/2\rangle \tag{3.4}$$

the angle θ between the C_3 axis of NH_3 and the C_6 axis of C_6H_6 was found to be 57.6 ± 0.3°. The a-component of the dipole moment of the complex, obtained from the Stark shift of the K=0 lines in a static electric field, is 1.142 Debye. The transition frequencies are listed in Table 3.7. Using the formula

$$\mu_a(C_6H_6 - NH_3) = \mu_{ind} + \mu_{NH_3}\langle cos\theta\rangle \tag{3.5}$$

Figure 3.5: Plot of R_{N-Bz} as a function of θ for $C_6H_6(^{14}NH_3)$, $C_6H_6(^{15}NH_3)$, and $C_6H_6(^{14}ND_3)$, from equation 3.3.

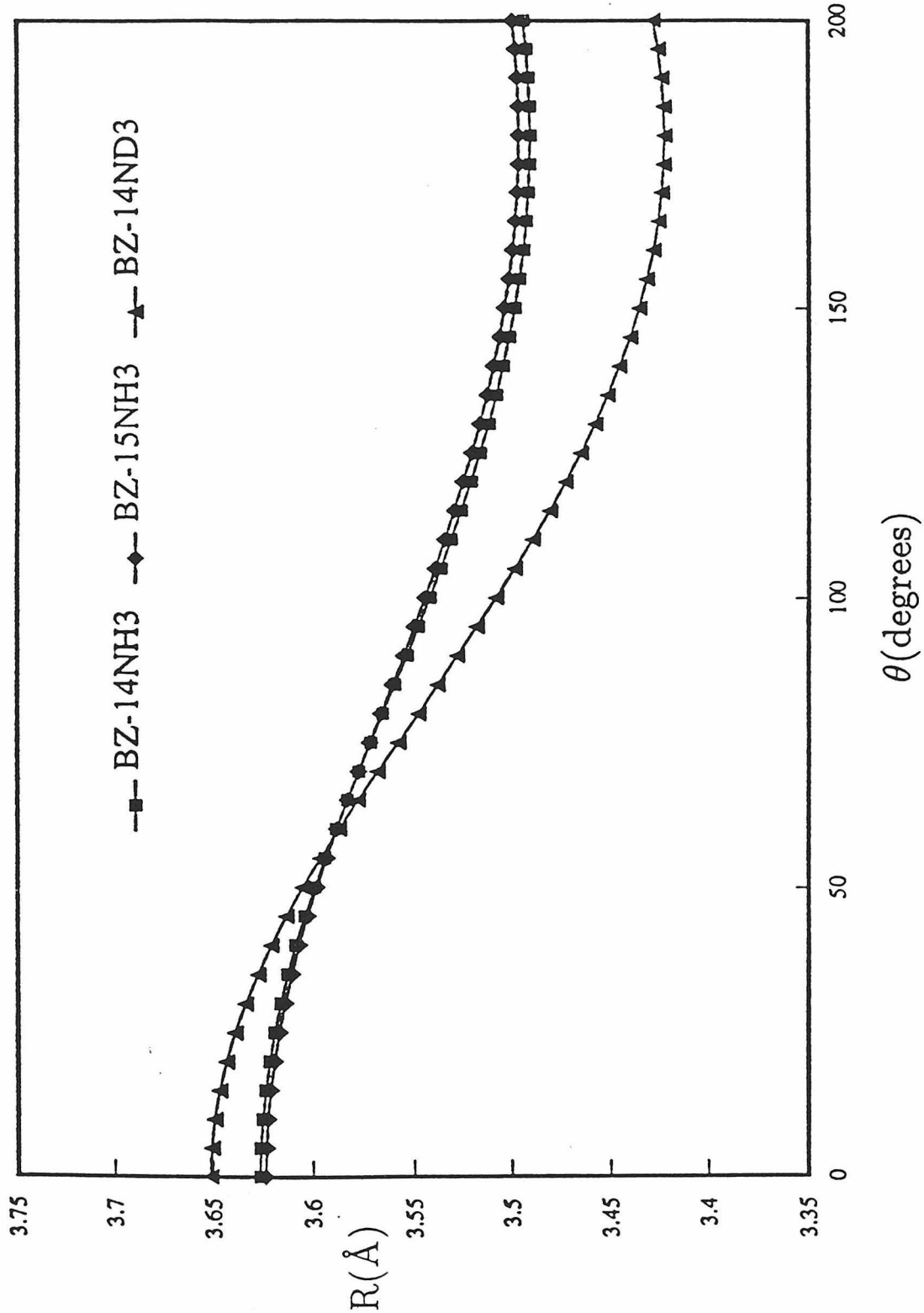
BZ-14NH3
BZ-15NH3
BZ-14ND3
R(Å)
θ(degrees)
3.75
3.7
3.65
3.6
3.55
3.5
3.45
3.4
3.35
0
50
100
150
200

Table 3.6: Hyperfine components of the J=3←2, K=2 transition of $C_6H_6(^{14}NH_3)$.

Transition ($F' \leftarrow F''$)	Frequency (MHz)
$2 \leftarrow 1$	11331.445
$3 \leftarrow 2$	11331.588
$4 \leftarrow 3$	11331.494

and the θ value determined from the nuclear quadrupole coupling constant, μ_{ind}, the induced dipole moment, was found to be 0.3 Debye, which is consistent with estimates based on the dipole moment of ammonia and the polarizability of benzene when θ is 60°. For a range of ± 0.1 Debye in μ_{ind}, a θ value of 60 ± 5°. was obtained. A drawing of the structure of the benzene-ammonia dimer is shown in Figure 3.6.

The agreement of these values indicates that the protons are "bound" to the π-cloud, or that the anisotropy of the intermolecular potential along the θ coordinate is large. In complexes with more isotropic potentials, such as Ar-NH_3, the θ values determined from the dipole moment and nuclear quadrupole coupling constant do not agree very well, since the dipole moment varies as $\langle cos\theta \rangle$, while the nuclear quadrupole coupling constant is weighted by $\langle cos^2\theta \rangle^{1/2}$ [11]. Finally, it should be noted that the *individual* protons of the NH_3 cannot be located since it is a symmetric top.

This same general structure has been found for the C_6H_6-HCl [12], C_6H_6-HF [13], and C_6H_6-H_2O [5, 4] hydrogen-bonded dimers. The HCl, HF, and H_2O were above the benzene plane, on the C_6 axis, with the protons pointing toward the benzene. These complexes, like C_6H_6-NH_3, exhibit symmetric top ground state spectra as a result of internal rotation or vibrational averaging that maintains symmetry about the benzene C_6 axis.

The value of R_{cm-cm} is larger for the benzene-ammonia dimer than for the benzene-water dimer, and the estimated dissociation energy D_0 of 1.4 kcal/mol, obtained from D_J and a Lennard-Jones radial potential, is smaller. This is consistent with the gas phase acidities of NH_3 and H_2O. Ab initio calculations performed at the MP2/6-31G** level support the general structure of the benzene-ammonia dimer, giving an

Figure 3.6: Coordinate system and structure of the benzene-ammonia dimer.

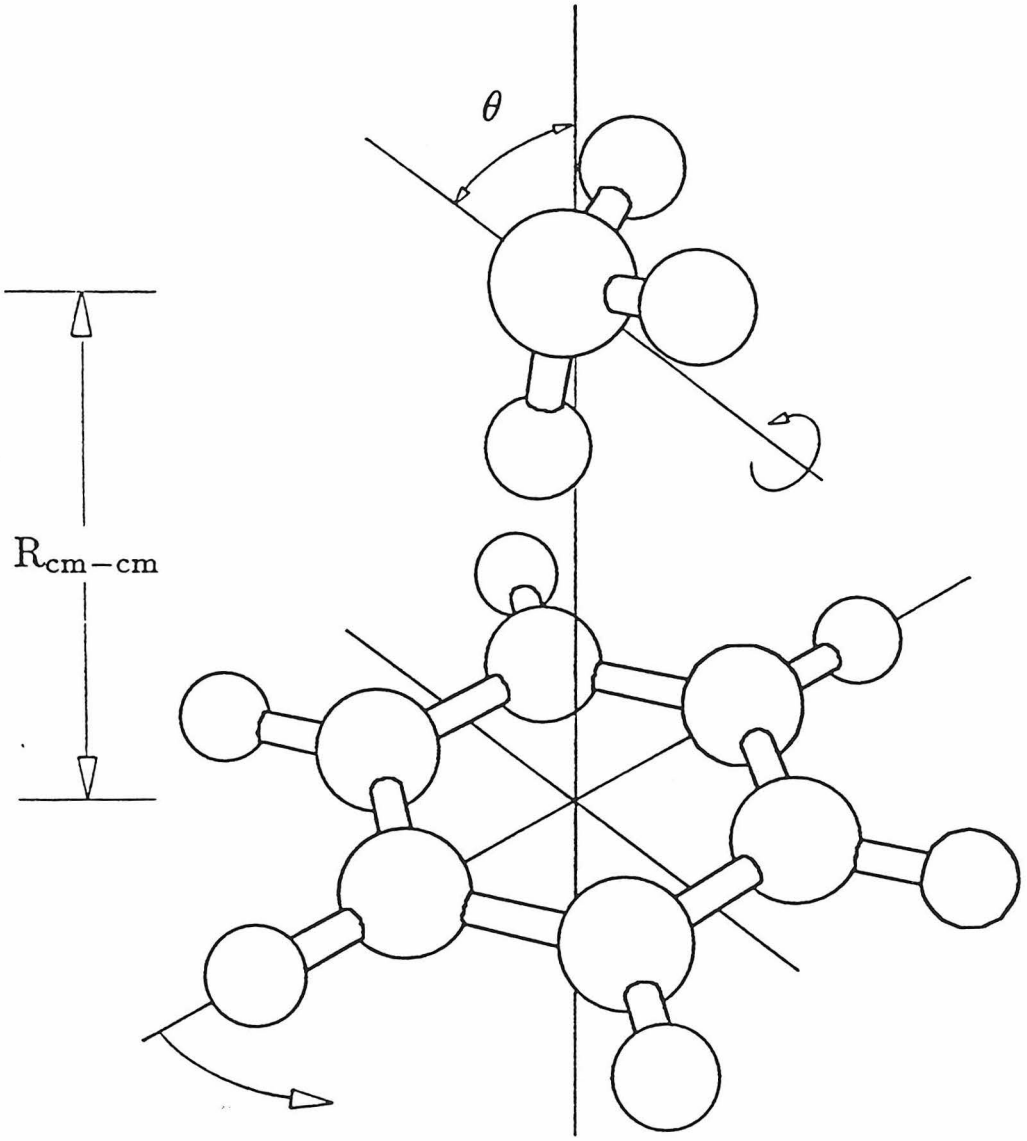
θ
R_{cm-cm}

Table 3.7: Stark field data for the benzene-ammonia rotational transitions observed with FTMW spectroscopy (MHz). The electric field was applied between plates having an effective separation of 33.8685 cm.

Transition ($J',M'_J \leftarrow J'',M''_J$)	E (kV)	$C_6H_6(^{14}NH_3)$	$C_6H_6(^{15}NH_3)$
3,0 ← 2,0	0	11333.714	10982.143
3,0 ← 2,0	4		10982.094
3,0 ← 2,0	5		10982.0755
3,0 ← 2,0	6	11333.64399	10982.048
3,0 ← 2,0	7		10982.020
3,0 ← 2,0	8	11333.57088	10981.9798
3,0 ← 2,0	10	11333.4900	
3,1 ← 2,1	0	11333.714	10982.143
3,1 ← 2,1	4	11333.69620	10982.125
3,1 ← 2,1	5		10982.118
3,1 ← 2,1	6	11333.68055	10982.110
3,1 ← 2,1	8	11333.67000	10982.090
3,1 ← 2,1	10	11333.67920	
3,2 ← 2,2	0	11333.714	10982.143
3,2 ← 2,2	4		10982.232
3,2 ← 2,2	5		10982.269
3,2 ← 2,2	6		10982.3135
3,2 ← 2,2	7		10982.383
3,2 ← 2,2	8		10982.460
3,2 ← 2,2	10		

R_{cm-cm} of 3.43 Å, a θ of 52°, and D_e of 2.4 kcal/mol [14]. The energy difference between structures in which one proton points toward the benzene and two protons point toward the benzene is only 35 cm^{-1}, a value comparable to the zero point energy.

3.4 Conclusions

The results of these experiments show that the benzene-ammonia dimer has a structure in which the NH_3 serves as the hydrogen bond donor and the C_6H_6 as the hydrogen bond acceptor, and can thus serve as a model of amino-aromatic hydrogen bonding interactions in condensed phase systems. While much structural information has been obtained here, and interaction strengths have been estimated, it is only a first step, one that serves as a foundation upon which future spectroscopic investigations of the benzene-ammonia IPES can be based.

Bibliography

[1] E. Riedle, Th. Knittel, Th. Weber, and H.J. Neusser, *J. Chem. Phys.*, 91:4555, 1989.

[2] Th. Weber, A.M. Smith, E. Riedle, H.J. Neusser, and E.W. Schlag, *Chem. Phys. Letters*, 175:79, 1990.

[3] J. Wanna, J.A. Menapace, and E.R. Bernstein, *J. Chem. Phys.*, 85:1795, 1986.

[4] A.J. Gotch and T.S. Zwier, *J. Chem. Phys.*, 96:3388, 1992.

[5] S. Suzuki, P.G. Green, R.E. Bumgarner, S. Dasgupta, W.A. Goddard III, and G.A. Blake, *Science*, 257:942, 1992.

[6] Sakae Suzuki, *Towards a More Quantitative Understanding of Intermolecular Interactions: Biologically Significant Intermolecular Clusters*, Ph.D. thesis, California Institute of Technology, 1996.

[7] P.M. Maxton, M.W. Schaeffer, and P.M. Felker, *Chem. Phys. Letters*, 241:603, 1995.

[8] S.M. Beck, M.G. Liverman, D.L. Monts, and R.E. Smalley, *J. Chem. Phys.*, 70:232, 1979.

[9] P.R. Bunker, *Molecular Symmetry and Spectroscopy*, Academic Press, Orlando, FL, 1979.

[10] G.T. Fraser, F.J. Lovas, R.D. Suenram, D.D. Nelson, Jr., and W. Klemperer, *J. Chem. Phys.*, 84:5983, 1986.

[11] D.D. Nelson, Jr., G.T. Fraser, K.I. Peterson, K. Zhao, and W. Klemperer, *J. Chem. Phys.*, 85:5512, 1986.

[12] W.G. Read, E.J. Campbell, and G. Henderson, *J. Chem. Phys.*, 78:3501, 1983.

[13] F.A. Baiocchi, J.H. Williams, and W. Klemperer, *J. Phys. Chem.*, 87:2079, 1983.

[14] D.A. Rodham, S. Suzuki, R.D. Suenram, F.J. Lovas, S. Dasgupta, W.A. Goddard III, and G.A. Blake, *Nature*, 362:735, 1993.

Chapter 4 ZEKE-PFI Spectroscopy of the $Na(H_2O)$ and $Na(NH_3)$ Complexes

4.1 Introduction

Alkali metal ions solvated by water and other polar molecules have received considerable attention [1, 2, 3, 4, 5] due to their importance in many chemical and biological systems, the central nervous system being a prime example. An accurate description of the manner in which the alkali ion-solvent and solvent-solvent interactions change within the solvation shells as a function of ionic radius is required to explain phenomena such as ion selectivity in membrane channels [6], but adequately detailed information is difficult to obtain from condensed phase measurements. Consequently, many researchers have studied gas phase clusters comprised of a metal ion attached to a few solvent molecules, since they form more accessible models of solution behavior.

Most of the experimental information available on clusters of the type $Na^+(H_2O)_n$ and $Na^+(NH_3)_n$ has been obtained via high pressure mass spectrometry. Specifically, by measuring the equilibrium constants for the reactions $Na^+(M)_n \leftrightarrow Na^+(M)_{n-1} + M$, where M is water or ammonia, the Kebarle and Castleman groups have determined the binding energies of the solvent molecules to the clusters as a function of n [7, 8]. As expected, the intermolecular potential wells are deeper than those of neutral hydrogen-bonded clusters such as $C_6H_6(NH_3)$ due to the ion-dipole character of the forces involved. The experimental binding energies also agree well with the results of numerous theoretical studies [9, 10, 11] for the range of n for which theoretical work has been done, namely $n \leq 6$. However, in the case of $Na^+(NH_3)_n$ clusters there is some disagreement on the number of solvent molecules required to fill the first solvation shell. The equilibrium constant data indicate that five molecules fill the shell [8], but the theoretical work of Hashimoto and Morokuma suggests that only four molecules

occupy the shell [11].

Further complicating the picture are mass spectrometric experiments recently performed by the Lisy group which suggest that six NH_3 molecules actually fill the first solvation shell in gas phase sodium-ammonia clusters [12]. They used infrared photons from a CO_2 laser to pump an ammonia vibrational mode in the clusters and mass spectrometry to detect predissociation products. Only clusters with more than six ammonia molecules fragmented, suggesting that the first six ammonia molecules are more strongly bound and form the first solvation shell. Although this method is somewhat indirect, no other spectroscopic information on the structures of these clusters has yet been obtained.

Indeed, while quantitative intermolecular potential energy surfaces (IPESs) can be obtained from high resolution spectra of the cluster intermolecular vibrational modes, as has been demonstrated in the case of hydrogen-bonded dimers [13], the absence of such data has thus far prevented the determination of the IPESs of $Na^+(H_2O)_n$ and $Na^+(NH_3)_n$ clusters. Indeed, the only measurements of intermolecular vibrational modes of such clusters were made by Hertel and co-workers, who determined the sodium ion-molecule stretching vibrational frequencies for the 1:1 complexes of Na^+ with water and ammonia from photoionization efficiency (PIE) spectra of the neutral dimers [14, 15]. Unfortunately, they were not able to measure the sodium ion-molecule bending vibrational frequencies or vibrational frequencies for any larger clusters, and the low resolution achieved in PIE spectroscopy did not allow the resolution of rotational levels needed for structural determination.

Neutral clusters composed of an alkali metal atom and solvent molecules are also of interest in their own right because of their utility in the study of electron solvation [16, 17, 18, 19, 20]. In this context, it is interesting to note that the ionization energies (IE) of clusters with $n \leq 20$ determined from PIE spectra reveal that while the $Na(NH_3)_n$ IEs decreased monotonically with n, those for $Na(H_2O)_n$ decreased until n = 4, whereupon they reached the bulk value and remained essentially constant [21]. Misaizu et al. found the same trends in the IEs of clusters of cesium atoms with water or ammonia [22].

Theoretical studies have offered two possible explanations for the different IE behavior of sodium-water and sodium-ammonia clusters. Using local spin density functional theory, Barnett and Landman [23] found that the Na atoms in $Na(H_2O)_n$ clusters with $n \geq 4$ are surrounded by H_2O molecules and that the Na 3s electron is partially removed from the atom and delocalized in a "surface Rydberg-like state." They claim that delocalization would not occur to the same extent in $Na(NH_3)_n$ clusters with $n \leq 30$, and that the cluster IEs will change until this size is reached. In an ab initio MO study, Hashimoto and Morokuma [10, 11] found that the Na atom is surrounded by NH_3 molecules and that the 3s electron is partially delocalized in large clusters, but in large $Na(H_2O)_n$ clusters they predict the Na atom is attached to the surface of a water cluster with the 3s electron located outside the water cluster and the IE largely unaffected by the addition of water molecules. Unfortunately, no direct structural evidence for either the neutral or ionized clusters has been obtained, and much more vibration-rotation data is needed to characterize their IPESs.

As a step toward a general description of alkali metal-solvent interactions, this study of 1:1 complexes of sodium with water or ammonia in the gas phase has been conducted using ZEKE-PFI photoelectron spectroscopy. It is well documented that the IEs of neutral clusters and the rovibrational energy levels of the ionized clusters can be measured more accurately with ZEKE-PFI spectroscopy than with energy resolved photoelectron or PIE spectroscopies [24, 25, 26, 27]. From the ZEKE-PFI spectra improved IEs for the $Na(H_2O)$and $Na(NH_3)$ dimers and improved sodium ion-molecule stretching vibrational frequencies for the ionized complexes have been obtained. Using two-photon ZEKE-PFI spectroscopy, the intermolecular bending vibrational frequencies for the $Na^+(NH_3)$ and $Na^+(ND_3)$ complexes have been measured for the first time. The intensities of certain vibrational bands in the two-photon ZEKE-PFI spectra were unexpectedly high, a result that is explained by vibronic coupling in the intermediate $\tilde{A}$ state. Finally, the rotational structure observed in the ZEKE-PFI spectra is discussed. Although complete rotational resolution was not achieved, the relative changes in the sodium-molecule bond lengths that occur with ionization have been determined from the rotational structure in the spectra.

4.2 Results and Discussion

Photoionization mass spectra showing that $Na(H_2O)_n$ and $Na(ND_3)_n$ complexes were indeed formed in the pick-up source and reach the ionization region of the TOFMS/ZEKE-PFI apparatus are shown in Figures 4.1 and 4.2. Laser light at 277 nm was used to ionize the Na in the complexes. The peak in both spectra at 6.68 μs is due to Na^+. In Figure 4.1, taken with water in the expansion mixture, the peaks at 8.92, 10.7, 12.22, 13.58, and 14.81 μs correspond to $Na(H_2O)_n$ complexes with n=1-5, respectively. In Figure 4.2, taken with an ND_3 expansion, the peaks at 9.12, 11.06, and 12.69 μs represent $Na(ND_3)_n$ complexes with n=1-3, respectively.

Single-photon ZEKE-PFI spectra of $Na(H_2O)$ and $Na(D_2O)$ are presented in Figure 4.3, while those for $Na(NH_3)$ and $Na(ND_3)$ are shown in Figure 4.4. The first and most intense peak in each spectrum is assigned to the $\Delta v = 0$ transition from the neutral complex's vibronic ground state to the vibronic ground state of the cation. This transition is denoted by 0_0^{0+}. Here the notation $\nu_{v''}^{v'}$ is such that the leading number refers to the vibrational mode involved in the transition, with the subscript and superscript denoting the vibrational quantum number in the lower and upper state, respectively. Quantum numbers of cations are followed by a plus symbol. The vibronic ground states of the neutral and ionized $Na(NH_3)$ and $Na(ND_3)$ complexes are predicted to have A_1 symmetry in the C_{3v} point group [28], while the vibronic ground states of the neutral and ionized $Na(H_2O)$ and $Na(D_2O)$ complexes are thought to have A_1 symmetry in the C_{2v} point group. Adiabatic ionization energies of 35323 ± 10 cm^{-1} for $Na(H_2O)$, 35249 ± 10 cm^{-1} for $Na(D_2O)$, 34435 ± 10 cm^{-1} for $Na(NH_3)$, and 34368 ± 10 cm^{-1} for $Na(ND_3)$ are derived from the spectra. While ZEKE-PFI spectroscopy is capable of giving more accurate IEs, the uncertainties of these values are large because of as yet unresolved rotational structure in the peaks and because no correction has been made for the lowering of the IE by the extraction field. The field-induced shift of the IE is denoted by ΔE and is given in cm^{-1} by $\Delta E = aF^{1/2}$ where F is the electric field in V/cm and a is a constant that generally falls between 2 and 6 [27]. However, I have not accurately determined the constant a for the com-

Figure 4.1: Oscilloscope trace of the signal from the TOFMS showing clusters of water with sodium.

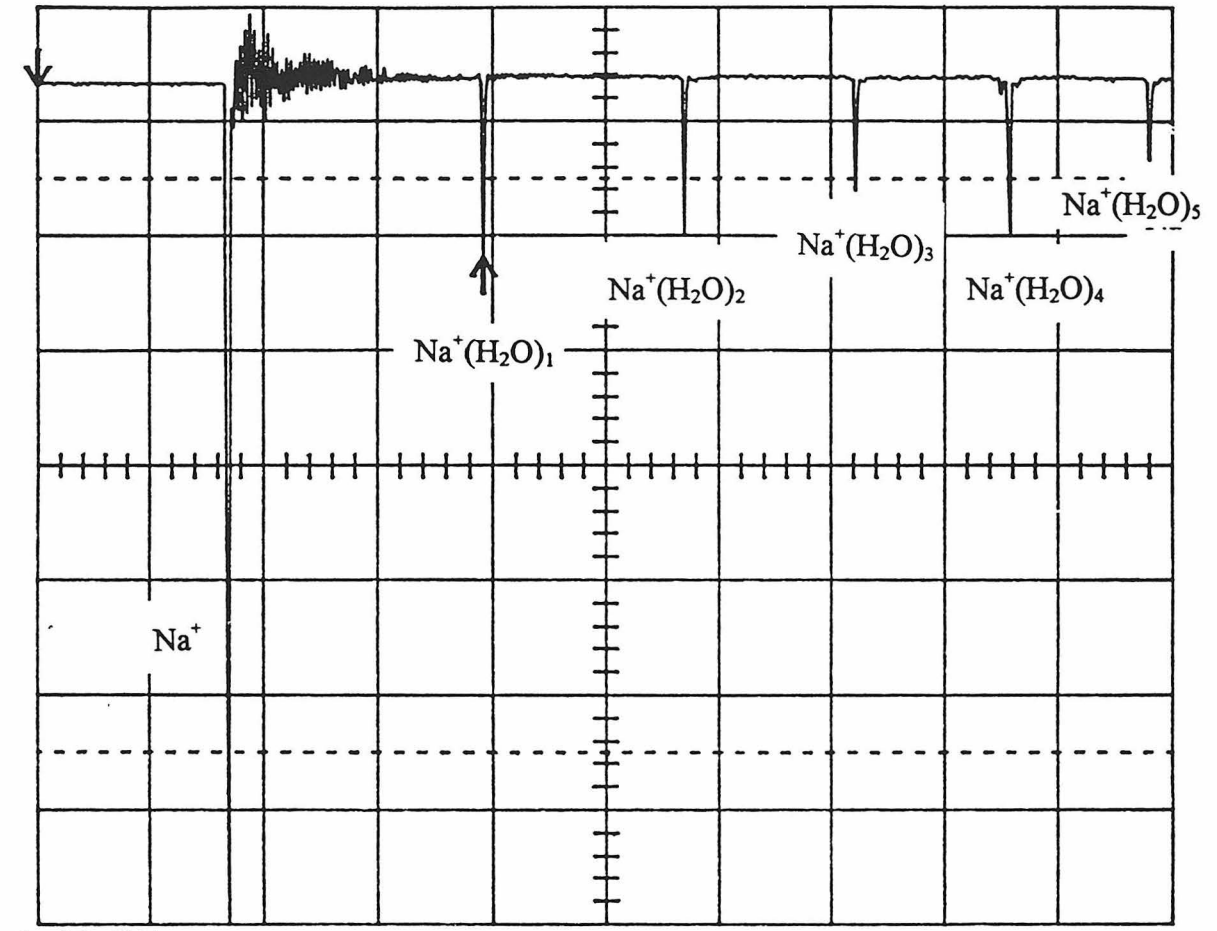

← 5.00 µs

Δt 3.92 µs

Ch 1 .1 V =
T/div 1 µs Ch 2 .2 V 50 Ω

Figure 4.2: Oscilloscope trace of the signal from the TOFMS showing clusters of ND_3 with sodium.

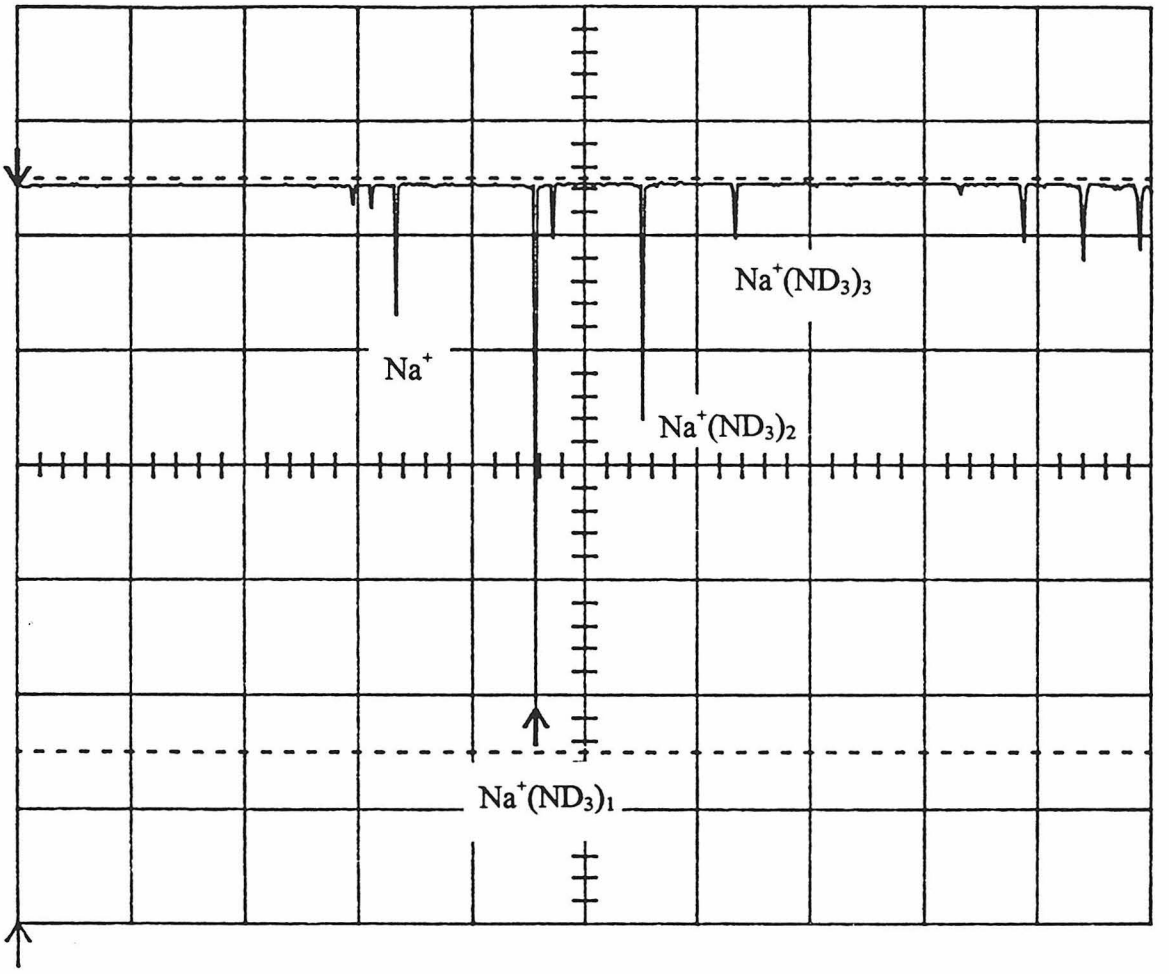

Δt 9.12 μs

Ch 1 50 mV =
T/div 2 μs Ch 2 .2 V 50 Ω

plexes in this study. The adiabatic IEs for $Na(H_2O)$ and $Na(NH_3)$ are, nevertheless, in excellent agreement with values obtained from PIE spectra by Schulz et al. and Nitsch et al. [14, 15] and with calculated values [10, 11, 23], while the adiabatic IEs of the deuterated complexes are shifted $\sim$70 cm^{-1} to lower frequency because of the changes in their zero point vibrational energies.

I assign the other peaks in these single-photon ZEKE-PFI spectra to transitions involving the sodium ion-molecule stretching and bending vibrational modes. The $Na(NH_3)$ and $Na(ND_3)$ complexes each have three vibrational modes of a_1 symmetry and three vibrational modes of e symmetry [29]. The sodium-ammonia stretching mode is the lowest frequency mode of a_1 symmetry and is denoted by ν_3, while the doubly degenerate sodium-ammonia bending mode is the lowest frequency mode of e symmetry and is denoted by ν_6. The $Na(H_2O)$ and $Na(D_2O)$ complexes also have six vibrational modes, three of which have a_1 symmetry. The sodium-water stretching mode is the lowest frequency mode of a_1 symmetry and is again denoted by ν_3. There are two nondegenerate sodium-water bending modes, one with b_1 symmetry and the other of b_2 symmetry, which are the lowest frequency non-totally symmetric modes in the complexes [9]. They are denoted by ν_5 and ν_6 , but I will hereafter refer to the bending modes only as ν_6 since, on account of spectral resolution or transition strength, only single peaks associated with the bending vibration were observed in the spectra, and no distinction between ν_5 and ν_6 could be made.

Following the 0_0^{0+} peak, each spectrum shows a short progression in ν_3. The frequencies of ν_3 are found to be 300 $\pm$ 5 cm^{-1} for $Na^+(H_2O)$, 296 $\pm$ 5 cm^{-1} for $Na^+(D_2O)$, 305 $\pm$ 5 cm^{-1} for $Na^+(NH_3)$, and 286 $\pm$ 5 cm^{-1} for $Na^+(ND_3)$. The $Na^+(H_2O)$ and $Na^+(NH_3)$ stretching frequencies are in excellent agreement with the values found by Schulz et al. and Nitsch et al. [14, 15], and the $Na^+(H_2O)$ frequency is also very close to that calculated previously [9, 23]. A summary of all the vibrational frequencies measured in this study may be found in Table 4.1. Unresolved rotational structure in the ZEKE-PFI peaks and the poorer signal-to-noise ratios of the higher peaks in the stretching mode progressions prevented me from measuring accurate anharmonicities. The lengths of the progressions in ν_3 indicate that the complexes

Figure 4.3: Single-photon ZEKE-PFI spectra of (a) $Na(H_2O)$ and (b) $Na(D_2O)$.

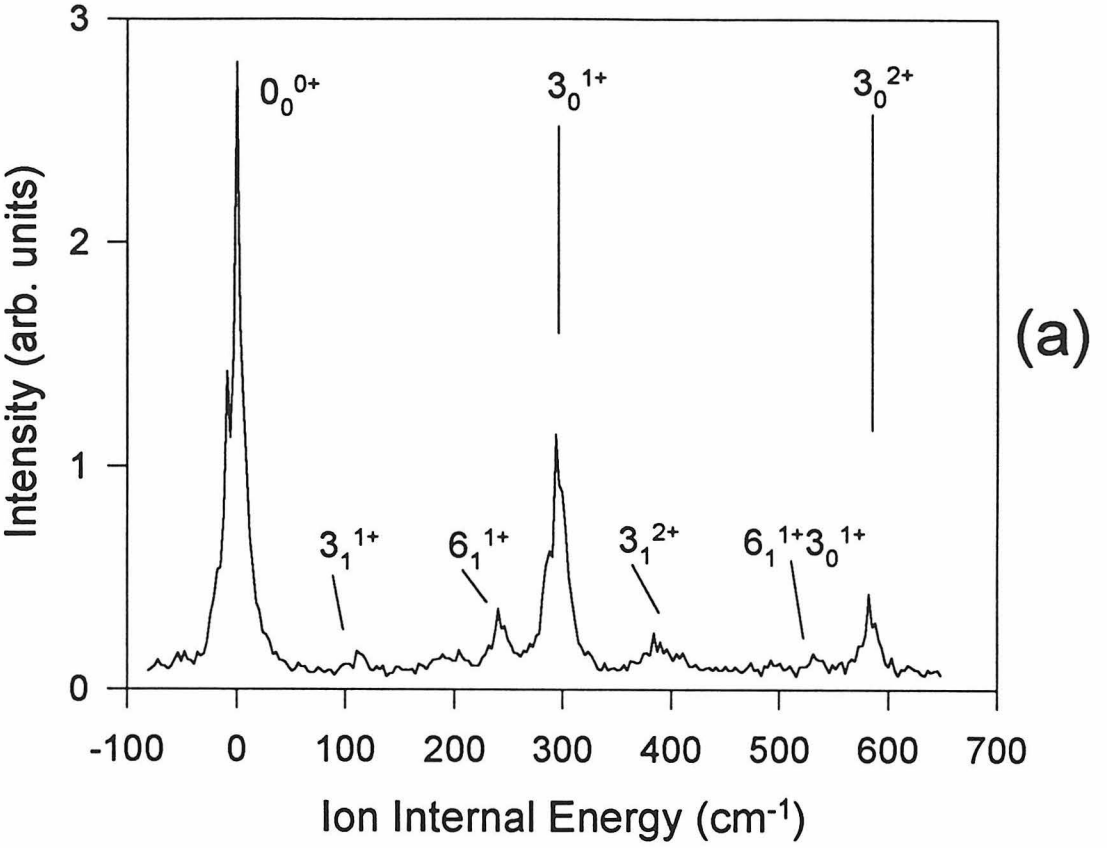
Intensity (arb. units)
Ion Internal Energy (cm-1)
0 0 0+
3 0 1+
3 0 2+
3 1 1+
6 1 1+
3 1 2+
6 1 1+ 3 0 1+
(a)

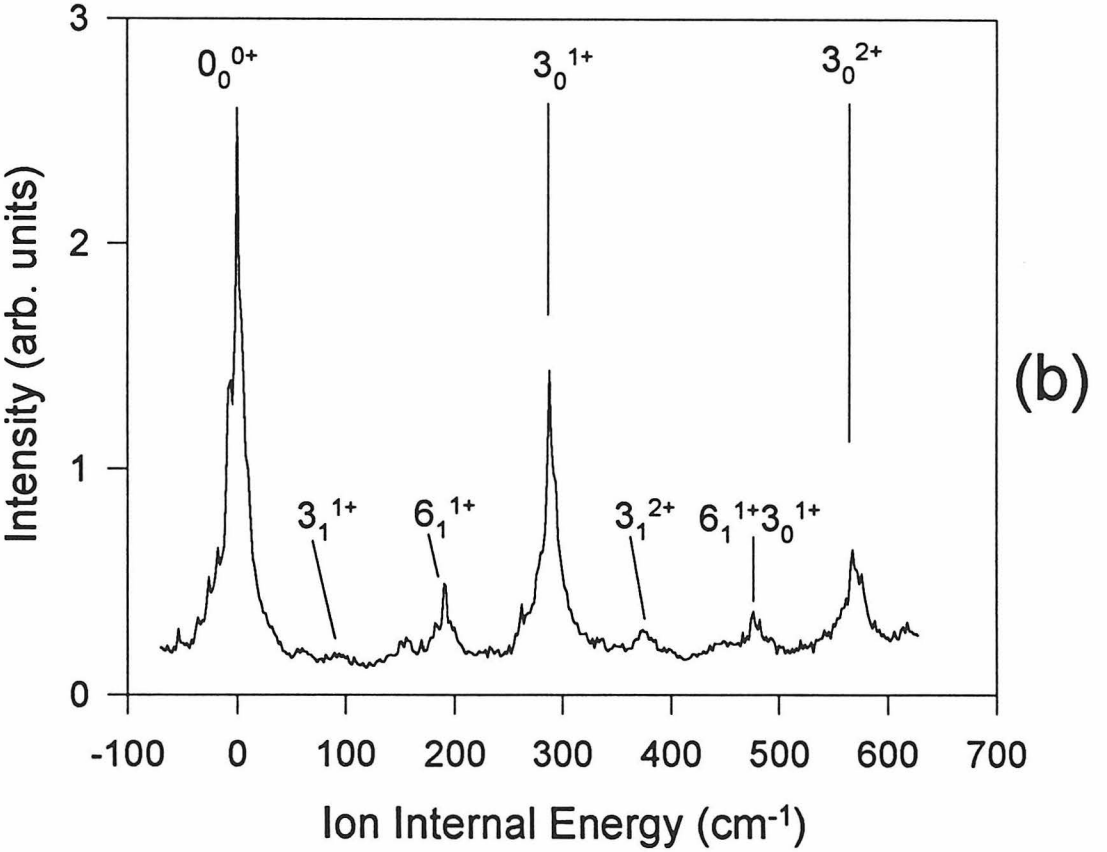
Intensity (arb. units)
Ion Internal Energy (cm-1)
0 0 0+
3 0 1+
3 0 2+
3 1 1+
6 1 1+
3 1 2+
6 1 1+ 3 0 1+
(b)

Figure 4.4: Single-photon ZEKE-PFI spectra of $Na(NH_3)$ and $Na(ND_3)$.

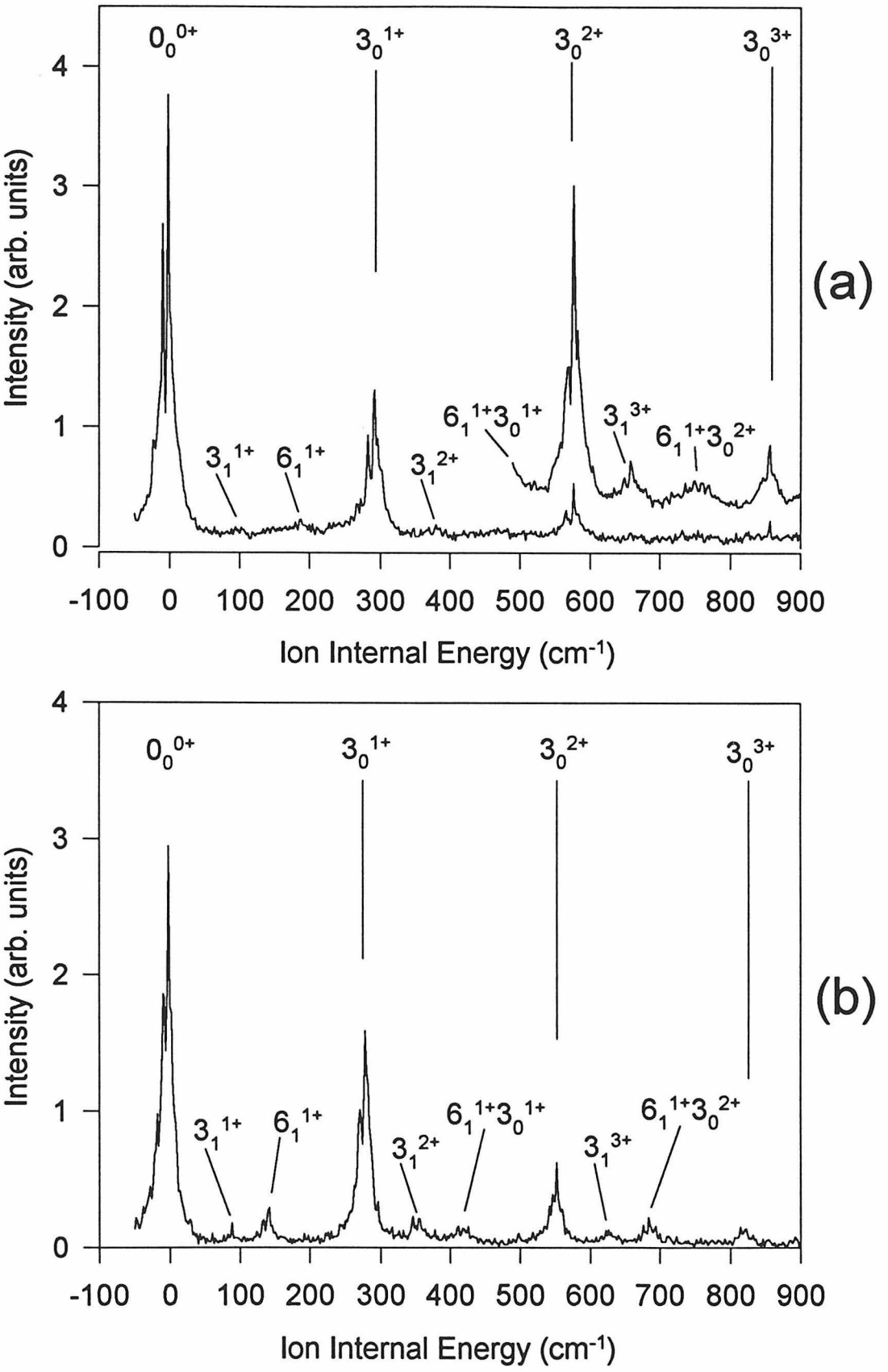
0_0^{0+}
3_0^{1+}
3_0^{2+}
3_0^{3+}
3_1^{1+}
6_1^{1+}
3_1^{2+}
$6_1^{1+}3_0^{1+}$
3_1^{3+}
$6_1^{1+}3_0^{2+}$
Intensity (arb. units)
Ion Internal Energy (cm^{-1})
(a)
(b)

Table 4.1: Ionization energies (IE), intermolecular stretching vibrational frequencies (ν_3), and intermolecular bending vibrational frequencies (ν_6) determined with ZEKE-PFI spectroscopy.

	$Na(H_2O)$	$Na(D_2O)$	$Na(NH_3)$	$Na(ND_3)$
IE (cm^{-1})	35323	35249	34435	34368
ν_3^+ (cm^{-1})	300	296	305	286
ν_3 (cm^{-1})	207	206	215	196
ν_6^+ (cm^{-1})	—	—	468	340
ν_6 (cm^{-1})	—	—	278	200
(ν_6^+-ν_6) (cm^{-1})	240	190	190	140

experience significant but not extremely large contractions of the sodium ion-molecule bond lengths upon ionization, also in agreement with theory. The calculated Na-O bond lengths for the $Na(H_2O)$ and $Na^+(H_2O)$ complexes are 2.355 Å and 2.23 Å, respectively [10], while the $Na(NH_3)$ and $Na^+(NH_3)$ bond lengths are predicted to be 2.526 Å and 2.365 Å [28].

The strongest peaks in the spectra in Figures 4.3 and 4.4 are most likely produced by the ionization of neutral complexes in their vibronic ground states. There are, however, weaker peaks that may plausibly be attributed to the ionization of vibrationally excited neutral complexes (the vibrational temperature is estimated to be at least 100 K). In each spectrum, the 0_0^{0+} peak and the peaks in the progression in ν_3 are each followed by two very weak peaks at higher energy. I assign these peaks to two sets of hot bands, one set produced by the ionization of neutral complexes from the ν_3 state, the other produced by complexes with ν_6 initially populated. The energy levels involved in these transitions are shown in Figure 4.5.

The small peaks that appear ~100 cm^{-1} above the 0_0^{0+} peaks of all four complexes probably arise from $\Delta v = 0$ transitions that originate from the $v = 1$ level of ν_3. If this assignment is correct, the energy difference between the 3_1^{1+} hot band and the 0_0^{0+} peak is determined by the difference between the frequency of ν_3 in the neutral complex and the frequency of ν_3 in the ionized complex. The frequencies of ν_3 in the ionized complexes, listed in Table 4.1, are ~300 cm^{-1}, while in the neutral $Na(H_2O)$ and $Na(NH_3)$ complexes ν_3 has a frequency of ~185 cm^{-1} [29]. The 3_1^{1+} transition

Figure 4.5: Partial energy level diagram showing the transitions responsible for the peaks observed in the single-photon ZEKE-PFI spectra of $Na(H_2O)$ and $Na(NH_3)$. Solid arrows indicate cold bands while dashed arrows indicate hot bands.

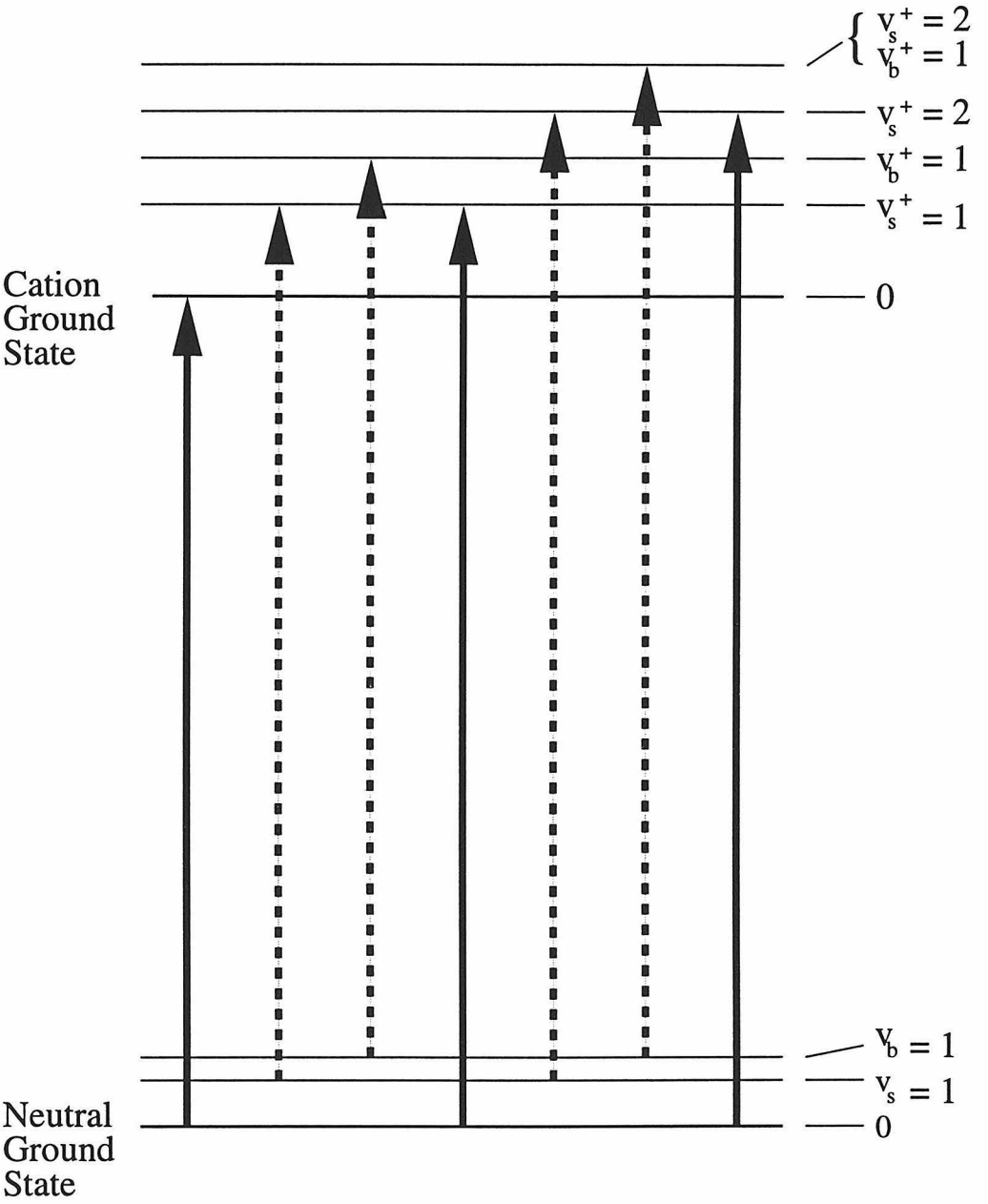
$v_s^+ = 2$
$v_b^+ = 1$
$v_s^+ = 2$
$v_b^+ = 1$
$v_s^+ = 1$
Cation
Ground
State
0
$v_b = 1$
$v_s = 1$
Neutral
Ground
State
0

should therefore appear $\sim$100 cm^{-1} higher in energy than the 0_0^{0+} transition, as observed. The shift is roughly the same for the deuterated complexes because isotopic substitution does not cause a large change in the pseudo-diatomic stretching reduced mass. A progression in ν_3 is built upon the 3_1^{1+} false origin.

The Na(H_2O) spectrum exhibits a weak peak 240 cm^{-1} above the 0_0^{0+} peak, while the Na(NH_3) spectrum shows a weak peak 190 cm^{-1} above its 0_0^{0+} origin. I attribute these peaks to $\Delta v = 0$ transitions, but now originating from the $v = 1$ level of ν_6. Such an assignment is supported by the Na(D_2O) and Na(ND_3) data, in which these 6_1^{1+} hot bands are located only $\sim$190 cm^{-1} and $\sim$140 cm^{-1} above the respective 0_0^{0+} peaks. This isotopic reduction of the energy difference between the 6_1^{1+} and 0_0^{0+} transitions, by almost a factor of $1/\sqrt{2}$, is expected for a vibrational mode involving primarily the motion of the hydrogen atoms. In the Na(NH_3) and Na(ND_3) spectra, only a single peak associated with ν_6 is expected, since ν_6 is doubly degenerate. On the other hand, the Na(H_2O) and Na(D_2O) spectra might be expected to show one peak for each of the two nondegenerate intermolecular bending vibrational modes. The spectra in Figure 4.3 hint at the existence of a second very weak peak that could be assigned as a false origin associated with another bending mode, but the signal-to-noise ratios were too poor to clarify this matter. Progressions in ν_3 are then built upon the 6_1^{1+} false origins.

In order to measure the frequency of ν_6 for the $Na^+(NH_3)$ and $Na^+(ND_3)$ complexes, which could not be obtained from the single-photon ZEKE-PFI spectra alone, I performed ZEKE-PFI experiments using resonant two-color (1+1′) photoionization via the $\tilde{A}\ ^2E$ state. The $\tilde{A}\ ^2E$ excited electronic state of Na(NH_3) has been studied theoretically by Greer et al. and experimentally by Nitsch et al. [28, 29]. A spectrum containing several vibrational bands of the Na(ND_3) $\tilde{A}\ ^2E \leftarrow \tilde{X}\ ^2A_1$ transition, obtained by resonant two-color (1+1′) photoionization spectroscopy, is shown in Figure 4.6a. The peaks are assigned to the following modes: 0_0^0 at 12250 cm^{-1}, 6_0^1 at 12470 cm^{-1}, 3_0^1 at 12550 cm^{-1}, and $6_0^1 3_0^1$ at 12750 cm^{-1}. The 6_0^1 and 3_0^1 peaks are well resolved in this spectrum, but could not be isolated in Nitsch et al.'s spectrum of the $\tilde{A}\ ^2E \leftarrow \tilde{X}\ ^2A_1$ transition of Na(NH_3) because the frequencies of ν_6 and ν_3 in

this state and isotopomer are almost the same. This near degeneracy led Nitsch et al. to assign peaks at higher energy to a progression in ν_6, but the $6_0^1 3_0^1$ transition in my spectrum of $Na(ND_3)$ shows that there is a progression in ν_3 built on the 6^1 level, not a progression based solely on the ν_6 bending vibrational mode.

The 6_0^1 transition would be forbidden if the Born-Oppenheimer and Condon approximations were rigorously satisfied. In such a case, the transition moment integral M is given by

$$M = \langle \psi_e'' \mid e\mathbf{r} \mid \psi_e' \rangle \langle \psi_{v''}'' \mid \psi_{v'}' \rangle \tag{4.1}$$

where ψ_e'' and ψ_e' are the electronic wave functions for the initial and final states, respectively, $\psi_{v''}''$ and $\psi_{v'}'$ are the corresponding vibrational wave functions, and $e\mathbf{r}$ is the electric dipole moment operator. The integral containing the product of the vibrational wave functions is zero by symmetry, because $e \otimes a_1$ does not contain the a_1 symmetry element. However, the 6_0^1 transition may become allowed by vibronic coupling, in which case the transition moment integral cannot be separated into electronic and vibrational components, and is given instead by

$$M = \langle \psi_{ev}'' \mid e\mathbf{r} \mid \psi_{ev}' \rangle \tag{4.2}$$

where ψ_{ev}'' and ψ_{ev}' are the vibronic wave functions of the initial and final states, respectively. If the vibronic coupling is strong and the $\tilde{A}$ state of $Na(NH_3)$ does indeed possess E symmetry, the 6_0^1 transition can become allowed through the Jahn-Teller effect. For example, excitation of an e vibrational mode in an E electronic state produces vibronic states having E, A_1, and A_2 symmetries. The transition from the A_1 ground state to an E vibronic state is a perpendicular transition, while the transition to the A_1 vibronic state is a parallel transition and the $A_2 \leftarrow A_1$ transition is forbidden. Only the $E \leftarrow A_1$ transition will have significant intensity, however, because it can borrow intensity from the transitions to the $\tilde{A}$ state that are allowed in the absence of vibronic coupling, which are perpendicular transitions [30]. Greer et al. predict that the second excited electronic state of $Na(NH_3)$ has A_1 symmetry and lies only 2400 cm^{-1} above the $\tilde{A}$ state, and the experimental work of Nitsch et al.

Figure 4.6: Two-color (1+1′) photoionization spectra of the $\tilde{A}\ ^2E \leftarrow \tilde{X}\ ^2A_1$ transition of $Na(ND_3)$. (a) Low resolution (2 cm^{-1}) spectrum. (b) High resolution (0.2 cm^{-1}) scan of the 0_0^0 band. (c) High resolution (0.2 cm^{-1}) scan of the 6_0^1 band.

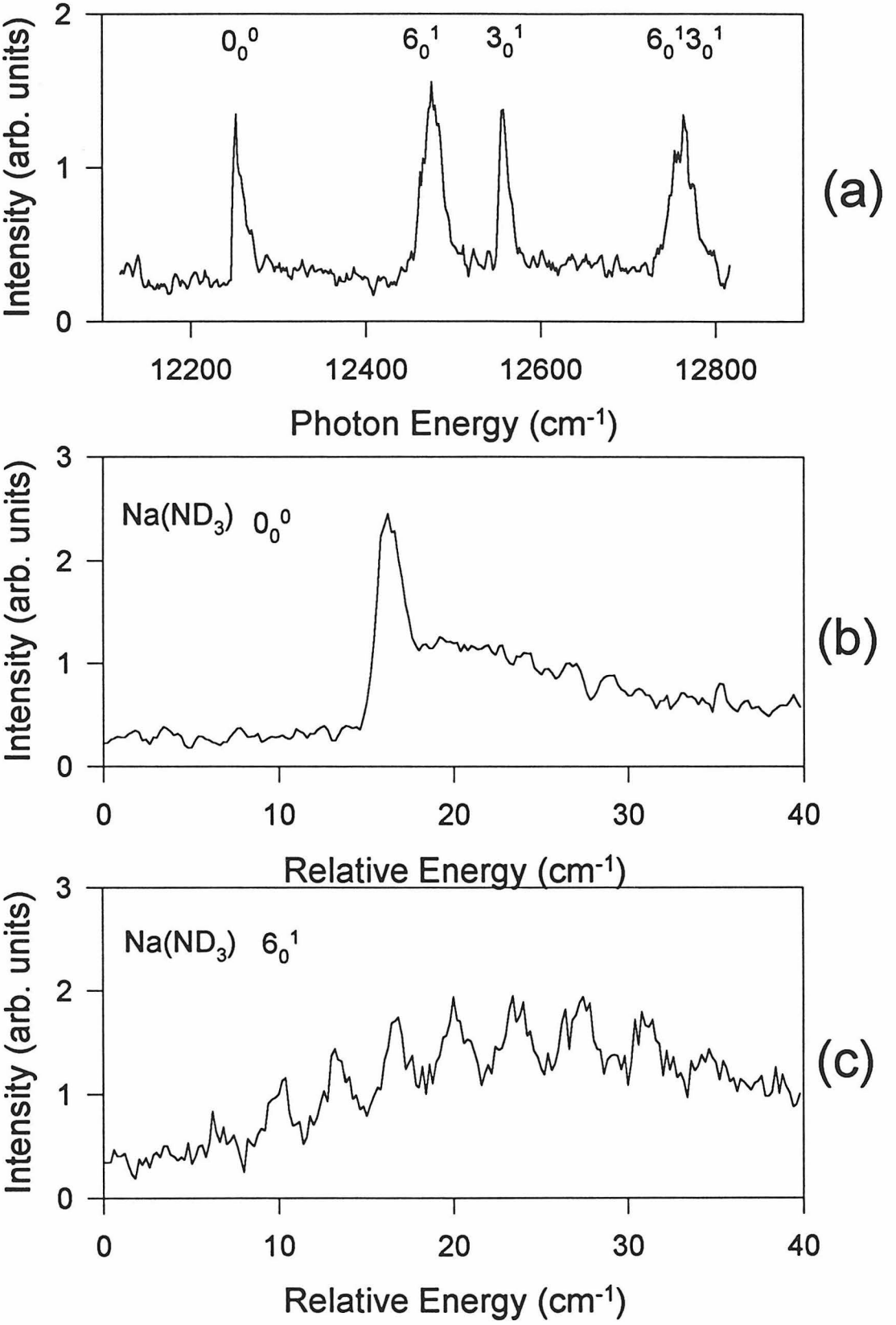
0_0^0
6_0^1
3_0^1
$6_0^1 3_0^1$
Intensity (arb. units)
Photon Energy (cm^{-1})
(a)
Na(ND$_3$) 0_0^0
Relative Energy (cm^{-1})
(b)
Na(ND$_3$) 6_0^1
Relative Energy (cm^{-1})
(c)

suggests that there is indeed an excited electronic state only 800 cm^{-1} above the $\tilde{A}$ state. Since the symmetries of the lowest excited electronic states of this complex have not been determined experimentally, the possibility exists that the $\tilde{A}$ state has A_1 symmetry and that the next highest level is of E symmetry. If the $\tilde{A}$ state does have A_1 symmetry, the 6_0^1 transition can become allowed not by the Jahn-Teller effect but by Herzberg-Teller coupling with the nearby electronic state of E symmetry [31]. In this case, the 0_0^0 band would be a parallel band, and the 6_0^1 band would be a perpendicular band because it borrows intensity from a perpendicular transition to an electronic state of E symmetry.

Which vibronic coupling mechanism is operative in this case must be determined from the rotational structure of the bands. Band profiles of the 0_0^0 and 6_0^1 transitions of $Na(ND_3)$ are shown in Figures 4.6b and 4.6c. The band contours are strikingly different. The $\tilde{A}\leftarrow\tilde{X}$ 0_0^0 band rises very sharply to a peak and then tails off smoothly. Such a band contour is characteristic of a parallel transition of a prolate symmetric top, with P branch head formation resulting from shrinkage of the Na-N bond. The 6_0^1 band, however, shows several sharp peaks spaced by 3.4 cm^{-1} , which is roughly one-half of the peak spacing observed in the $Na(NH_3)$ spectrum. This spacing is very close to the rotational constant of ammonia about its C_3 axis. It is also roughly an order of magnitude greater than the B rotational constants of these complexes derived from the calculated structures. Such a pattern is characteristic of a perpendicular transition of a symmetric top molecule for which $A \gg B$.

Similar structure is observed in the $Na(NH_3)$ spectra shown in Figure 4.7. The 0_0^0 band in panel (a) looks like a parallel band, while the $3_0^1 6_0^1$ band in panel (b) looks like a perpendicular band. These bands have been fit using symmetric top energy level expressions. Although they may be significant, centrifugal distortion and spin-rotation interactions have not been included. The resulting fits are shown in the figure, and the fit parameters are given in Table 4.2. While the rotational temperature of the complexes is not known, a value of 100 K seemed to work reasonably well. These are not given as the best or as unique fits, but only to demonstrate that the spectra can be fit with rotational constants expected for this complex. Most importantly, the

Table 4.2: Parameters used to fit the $Na(NH_3)$ 0_0^0 and $3_0^1 6_0^1$ bands.

Transition	A′ (GHz)	A″ (GHz)	B′ (GHz)	B″ (GHz)	ζ	T_{rot} (K)
0_0^0	204	184	8.5	7.5	—	100
$3_0^1 6_0^1$	184	184	8.2	7.5	0.45	100

fit of the 0_0^0 band indicates that the Na-N bond is ~6% shorter in the $\tilde{A}$ state than in the ground state.

If the $\tilde{A} \leftarrow \tilde{X}$ 0_0^0 transition is parallel and the 6_0^1 transition is perpendicular, the Herzberg-Teller vibronic coupling mechanism would then be responsible for the 6_0^1 transition. However, such a conclusion should not be based on unresolved rotational structure, since the structure of perpendicular bands can sometimes look like that of parallel bands. This happens because the peak spacing in a perpendicular band depends on the total vibronic angular momentum, which has an electronic component due to the degenerate electronic state and a vibrational component when the degenerate vibration is excited in that state [30]. Since the 0^0 level has no vibrational angular momentum, the peak spacing in a perpendicular 0_0^0 band will be different than in the 6_0^1 band. A famous example of this type of behavior is the $\tilde{C} \leftarrow \tilde{X}$ transition of CH_3I, which shows such pseudo-parallel bands [32]. Complete rotational resolution, then, will be required to settle the issue of the electronic state ordering and the vibronic coupling mechanism operative in the $Na(NH_3)$ complex.

In the interim, two-color excitation through the vibronic levels of the $\tilde{A}$ state has been used to further characterize the IPESs of the ionized complexes, particularly through the isolation of ν_6. Due to the $\Delta v = 0$ propensity rule which generally holds in the photoionization of molecules having similar geometries in their neutral and ionized forms [33], the vibrational mode that is excited in the intermediate electronic state will usually show the strongest peak in the ZEKE-PFI spectrum. A two-color ZEKE-PFI spectrum of $Na(ND_3)$ taken via the 0^0 level of the $\tilde{A}$ state is shown in Figure 4.8a. The strongest peak results from ionization to the cation ground state (the 0_0^{0+} transition). This $\Delta v = 0$ behavior is expected, since the calculated geometry of the $\tilde{A}$ state of the $Na(NH_3)$ complex is very close to that of the $Na^+(NH_3)$ complex.

Figure 4.7: Two-color (1+1′) photoionization spectra of the $\tilde{A}\ ^2E \leftarrow \tilde{X}\ ^2A_1$ transition of $Na(NH_3)$. (a) Scan of the 0_0^0 band. (b) Scan of the $3_0^1 6_0^1$ band.

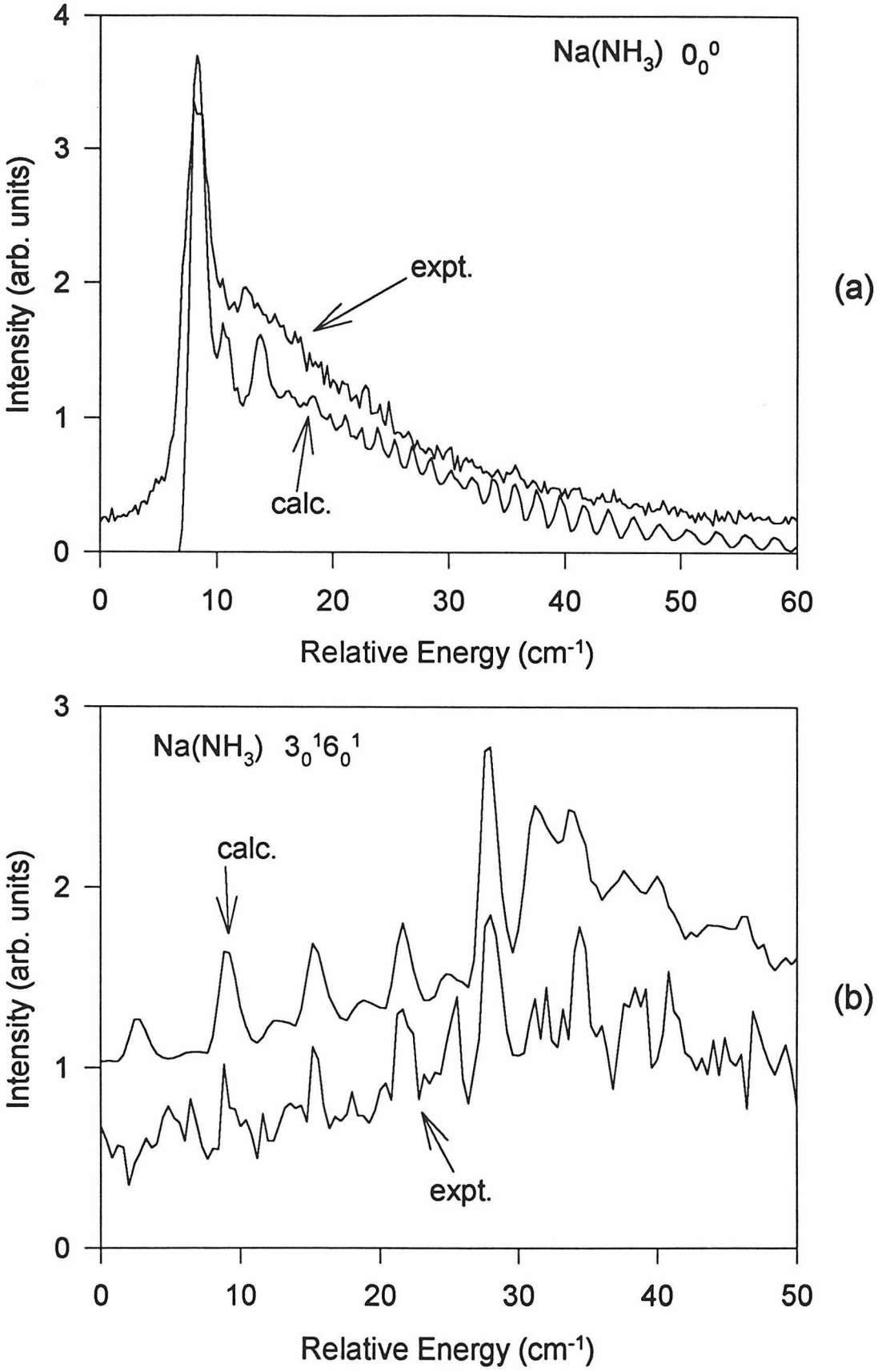
Na(NH3) 0₀⁰
expt.
calc.
Intensity (arb. units)
Relative Energy (cm⁻¹)
(a)
Na(NH3) 3₀¹6₀¹
calc.
expt.
Intensity (arb. units)
Relative Energy (cm⁻¹)
(b)

Two weaker peaks appear 290 cm^{-1} and 340 cm^{-1} higher in energy, and are assigned to the 3_0^{1+} and 6_0^{1+} transitions, respectively. It should be noted that the 3_0^{1+} transition is much weaker than in the single-photon ZEKE-PFI spectrum, and this probably indicates that the Na-N bond is shorter in the $\tilde{A}$ state than in the ground state of the neutral complex, as Greer et al. have suggested.

Two-color ZEKE-PFI spectra taken via the 6^1 level in the $\tilde{A}$ state of the $Na(ND_3)$ and $Na(NH_3)$ complexes are shown in Figures 4.8b and 4.8c, respectively. The assignment of the $Na(ND_3)$ 6_0^{1+} transition in Figure 4.8a is supported by the spectrum in Figure 4.8b, which shows a strong peak for the 6_1^{0+} transition, a strong feature 340 ± 10 cm^{-1} above the 6_1^{0+} peak corresponding to the 6_1^{1+} transition, and a weak peak 680 cm^{-1} above the 6_1^{0+} peak that I assign to the 6_1^{2+} transition. The spectrum of $Na(NH_3)$ in Figure 4.8c was obtained by tuning the excitation laser to the low frequency side of the spectral feature formed by the superposition of the 6_0^1 and 3_0^1 bands in the $Na(NH_3)$ $\tilde{A} \leftarrow \tilde{X}$ transition. It shows a strong 6_1^{0+} peak and a strong peak 468 ± 10 cm^{-1} higher in energy, which I assign as the 6_1^{1+} transition. The intensity of the 6_1^{0+} peak is greater than that of the 6_1^{1+} peak, seemingly in violation of the $\Delta v = 0$ propensity rule. This deviation from expected behavior is partly due to a loss of intensity in the ionization laser beam as the blue edge of the laser dye's tuning curve was approached. However, it is significant that the 6_1^{0+} transition appears with intensity comparable to that of the 6_1^{1+} transition.

The ratio of the frequencies of the ν_6 vibrational modes of the $Na^+(ND_3)$ and $Na^+(NH_3)$ complexes is 0.726, which is approximately what one would expect for this bending mode. The $Na^+(NH_3)$ bending frequency is also reasonably close to the bending frequencies calculated for the $Na^+(H_2O)$ complex [9]. The increased "stiffness" in the bending coordinate relative to the stretching coordinate results from the directionality of the ion-dipole force which is the main contributor to the bonding in this complex [29]. Combining these results with the changes in the ν_6 modes derived from the hot bands observed in the single-photon ZEKE-PFI spectra, frequencies for ν_6 in the neutral $Na(NH_3)$ and $Na(ND_3)$ complexes are found to be 278 ± 20 cm^{-1} and 200 ± 20 cm^{-1}, respectively. It is somewhat surprising that the bending frequency

Figure 4.8: Two-color ZEKE-PFI spectra of (a) $Na(ND_3)$ via the 0^0 level of its $\tilde{A}$ state, (b) $Na(ND_3)$ via the 6^1 level of its $\tilde{A}$ state, and (c) $Na(NH_3)$ via the 6^1 level of its $\tilde{A}$ state.

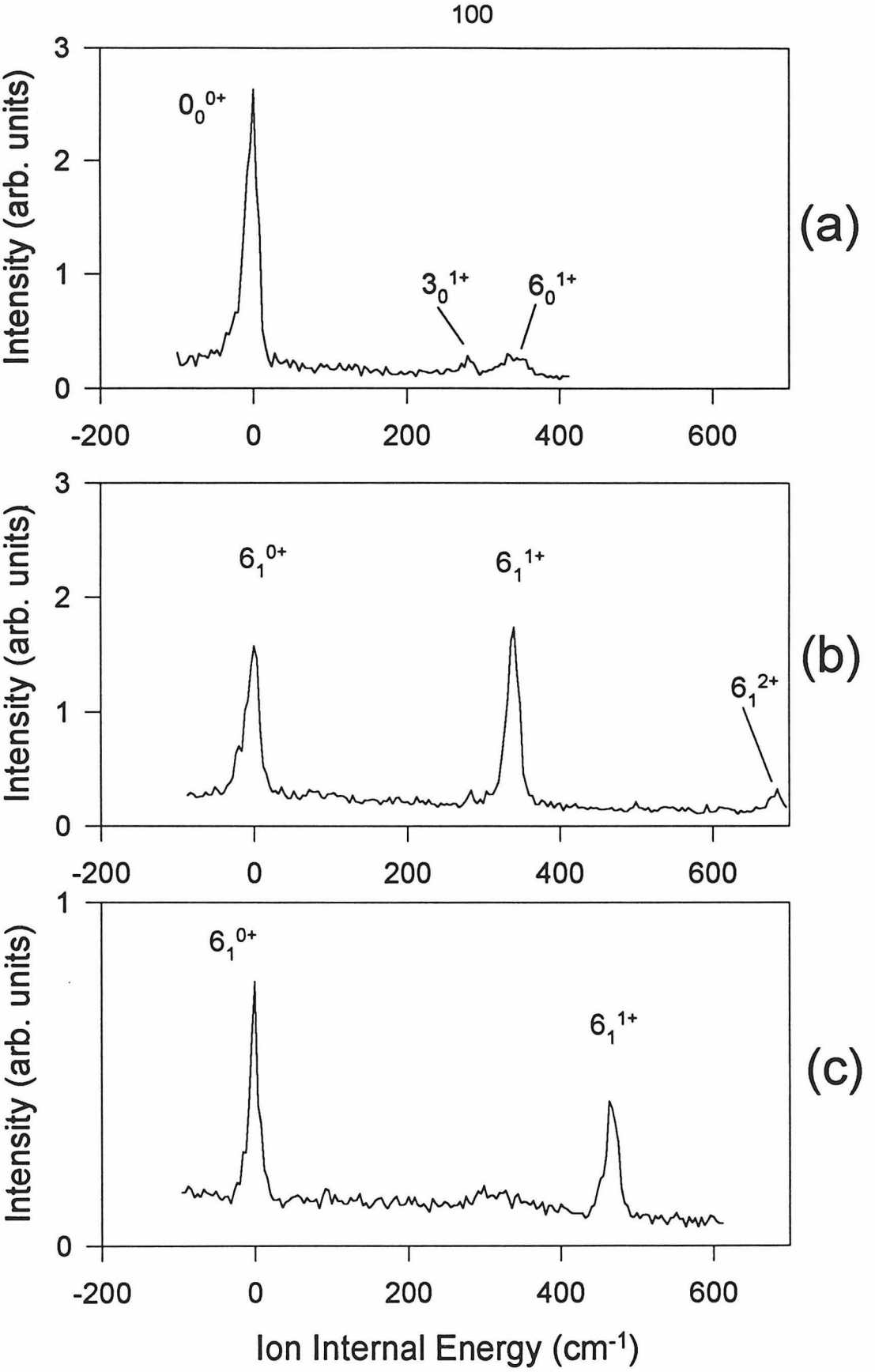
Intensity (arb. units)
0_0^{0+}
3_0^{1+}
6_0^{1+}
(a)
6_1^{0+}
6_1^{1+}
6_1^{2+}
(b)
6_1^{0+}
6_1^{1+}
(c)
-200
0
200
400
600
Ion Internal Energy (cm^{-1})

for the neutral $Na(NH_3)$ complex is higher than that for the stretching mode, since the calculations that have been done on similar species to date have found that the stretching frequencies are higher [19, 34]. However, this finding is supported by the results of Loutellier et al. [35], who measured the intermolecular vibrational frequencies of $Li(NH_3)$ in an argon matrix and found the bending frequency (381 cm^{-1}) to be higher than the stretching frequency (320 cm^{-1}). The measurement of the vibrational frequencies of other alkali metal-molecule complexes should shed considerable light on the nature of the bonding interactions in these neutral complexes.

The assigned ν_6 frequency for the $Na^+(NH_3)$ complex is supported by the spectrum presented in Figure 4.9a, taken via the 3^1 level of the $\tilde{A}$ state. The strongest peak in the spectrum is assigned to the 3_1^{1+} transition, and weak peaks that we assign to the 3_1^{0+}, $6_0^{1+}3_1^{0+}$, and 3_1^{2+} transitions are evident. The $6_0^{1+}3_1^{0+}$ peak is 470 cm^{-1} above the 3_1^{0+} peak.

ZEKE-PFI spectra of $Na(NH_3)$ and $Na(ND_3)$ taken via the 6^13^1 level of the $\tilde{A}$ state are shown in Figures 4.9b and 4.9c. The $Na(NH_3)$ spectrum shows a $6_1^{0+}3_1^{0+}$ peak, a $6_1^{0+}3_1^{1+}$ peak, a $6_1^{0+}3_1^{2+}$ peak, and a peak 770 cm^{-1} above $6_1^{0+}3_1^{0+}$ peak that we assign to the $6_1^{1+}3_1^{1+}$ transition. The $6_1^{1+}3_1^{0+}$ transition appears with very little intensity. The $Na(ND_3)$ spectrum shows a peak for the $6_1^{0+}3_1^{0+}$ transition, a peak for the $6_1^{0+}3_1^{1+}$ transition 280 cm^{-1} above it, and a third peak 624 cm^{-1} above $6_1^{0+}3_1^{0+}$ peak that corresponds to the $6_1^{1+}3_1^{1+}$ transition. These spectra confirm my assignments of the intermediate states.

The most startling aspect of the ZEKE-PFI spectra taken via the 6^13^1 level is the violation of the $\Delta v = 0$ propensity rule by strong transitions to ion vibrational states of different symmetry. The spectra show the expected $\Delta v = 0$ transition to the $6^{1+}3^{1+}$ level which has e symmetry, but also strong transitions to the origin and the 3^{1+} level, which have a_1 symmetry. Interestingly, the peak for the transition to the 6^{1+} level is weak or nonexistent. Similar behavior is observed in the spectra taken via the 6^1 level, shown in Figures 4.8b and 4.8c, which show the $\Delta v = 0$ peaks for the transition to the 6^{1+} level as well as strong transitions to the ion ground states. In contrast, the ZEKE-PFI spectra shown in Figures 4.8a and 4.9a, taken via states of a_1

Figure 4.9: Two-color ZEKE-PFI spectra of (a) $Na(NH_3)$ via the 3^1 level of its $\tilde{A}$ state, (b) $Na(NH_3)$ via the $6^1 3^1$ level of its $\tilde{A}$ state, and (c) $Na(ND_3)$ via the $6^1 3^1$ level of its $\tilde{A}$ state.

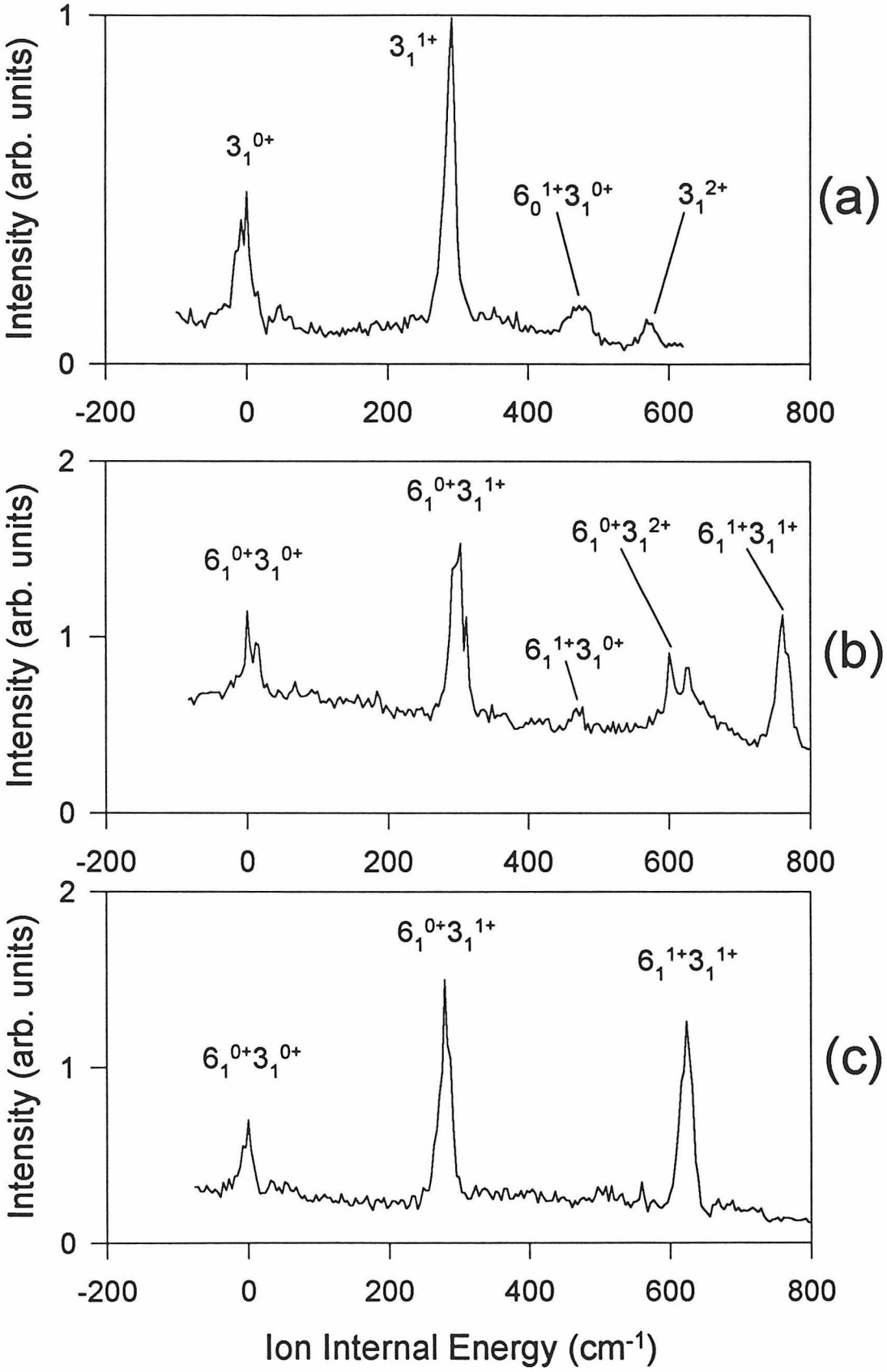
Intensity (arb. units)
1
0
3_1^{1+}
3_1^{0+}
$6_0^{1+}3_1^{0+}$
3_1^{2+}
(a)
-200
0
200
400
600
800
Intensity (arb. units)
2
1
0
$6_1^{0+}3_1^{1+}$
$6_1^{0+}3_1^{2+}$
$6_1^{1+}3_1^{1+}$
$6_1^{0+}3_1^{0+}$
$6_1^{1+}3_1^{0+}$
(b)
-200
0
200
400
600
800
Intensity (arb. units)
2
1
0
$6_1^{0+}3_1^{1+}$
$6_1^{1+}3_1^{1+}$
$6_1^{0+}3_1^{0+}$
(c)
-200
0
200
400
600
800
Ion Internal Energy (cm^{-1})

vibrational symmetry that possess no excitation of ν_6, show only very weak transitions to states of e vibrational symmetry. Thus, the selection rule for allowed electronic transitions which forbids interactions between states of different vibrational symmetry (see equation 4.1) is most closely followed in the single-photon ZEKE-PFI spectra, which show only transitions between states having the same vibrational symmetry.

I attribute the transitions between states of different vibrational symmetry to strong vibronic coupling in the $\tilde{A}$ state, which my spectra of the $\tilde{A}$ state have shown to exist. It should be noted that vibronic coupling in the intermediate electronic state has been found to be responsible for transitions between states of different vibrational symmetry in two-color ZEKE-PFI spectra of other molecules [36, 37]. It is possible that the transitions could result from vibronic coupling in the cation, but this would require either the existence of low-lying excited electronic states in the cation or degeneracy of the ground electronic state of the cation. To my knowledge, neither condition is satisfied in the $Na^+(NH_3)$ complex. Further understanding of vibronic coupling in this complex, as well as the structural parameters of complexes of sodium ions with ammonia, water and other molecules, can be obtained from rotationally resolved two-color ZEKE-PFI spectra which are currently being taken.

4.3 Rotational Structure

4.3.1 Single Photon Spectra

Close-up views of the ZEKE-PFI spectra of the 0_0^{0+} transitions of $Na(H_2O)$ and $Na(D_2O)$ are shown in Figure 4.10, while spectra of the same transition for the $Na(NH_3)$ and $Na(ND_3)$ complexes are shown in Figure 4.11. The extraction field was 0.67 V/cm and the step size 1 cm^{-1} for the scans of the complexes with water, while the extraction field was 0.29 V/cm and the step size 0.5 cm^{-1} for the scans of the ammonia- containing complexes. All of the spectra look very similar, with no large differences resulting from deuteration or the different symmetries of the water- and ammonia-containing complexes. Since the B rotational constants of all the complexes

are nearly the same while the A rotational constants are very different, it is reasonable to assume that the structure in the ZEKE-PFI spectra results from transitions in which N, but not K, changes. A $\Delta N = 0, \pm 1$, $\Delta K = 0$ selection rule is expected for the optical parallel transitions between states of A symmetry of symmetric top and slightly asymmetric top molecules having C_{3v} and C_{2v} symmetry [30]. Although the $Na(H_2O)$ complex is a slightly asymmetric top, the spectra of similar complexes such as $Ca^+(H_2O)$ and $Mg^+(H_2O)$ have been fit successfully with symmetric top energy level expressions [38]. The ZEKE-PFI spectrum of Na(HDO) shown in Figure 4.12 has the same structure observed in the spectra of the other complexes, demonstrating that the structure is not produced by metastable rotational states, which, unlike the H_2O, D_2O, or NH_3 in the other complexes, HDO does not have.

The spectra consist primarily of three peaks, the highest a very narrow (1.5 cm^{-1}) peak, with more rounded peaks of roughly equal intensity on either side. At first glance, this looks like a Q branch with P and R branches beside it, but this assessment must be discarded for at least two reasons. First, the side peaks occur at different distances from the central peak (8-9 cm^{-1} for the peak at lower frequency vs 3-4 cm^{-1} for the peak at higher frequency). Second, high quality ab initio calculations indicate that the sodium-molecule bond lengths of all the complexes decrease when they are ionized [28, 10], which means that the spectra should have P band heads.

I have assigned the sharp central peak in each spectrum as a P band head, and the features found on the high frequency side of this peak are assigned to unresolved Q and R branches. The peak on the low frequency side of the center peak is assigned as an O branch, and structure even farther away from the P band head is assigned to an N branch and other branches. To support these assignments, in Figure 4.13 the ZEKE-PFI spectrum of $Na(NH_3)$ is compared to the two-color (1+1′) photoionization spectrum taken via the $\tilde{A}$ state origin of $Na(NH_3)$, and it may be seen that the spectra are very similar from the sharp P band head to higher frequency. It is reasonable to compare the rotational contours of these spectra, because the binding strength in the $\tilde{A}$ state is 75% of the binding strength in the cation [29], and calculations indicate that the sodium-ammonia bond is shorter in the $\tilde{A}$ state of the complex than in the

Figure 4.10: Rotational profiles in the single-photon ZEKE-PFI spectra of the 0_0^{0+} transition of (a) $Na(H_2O)$ and (b) $Na(D_2O)$.

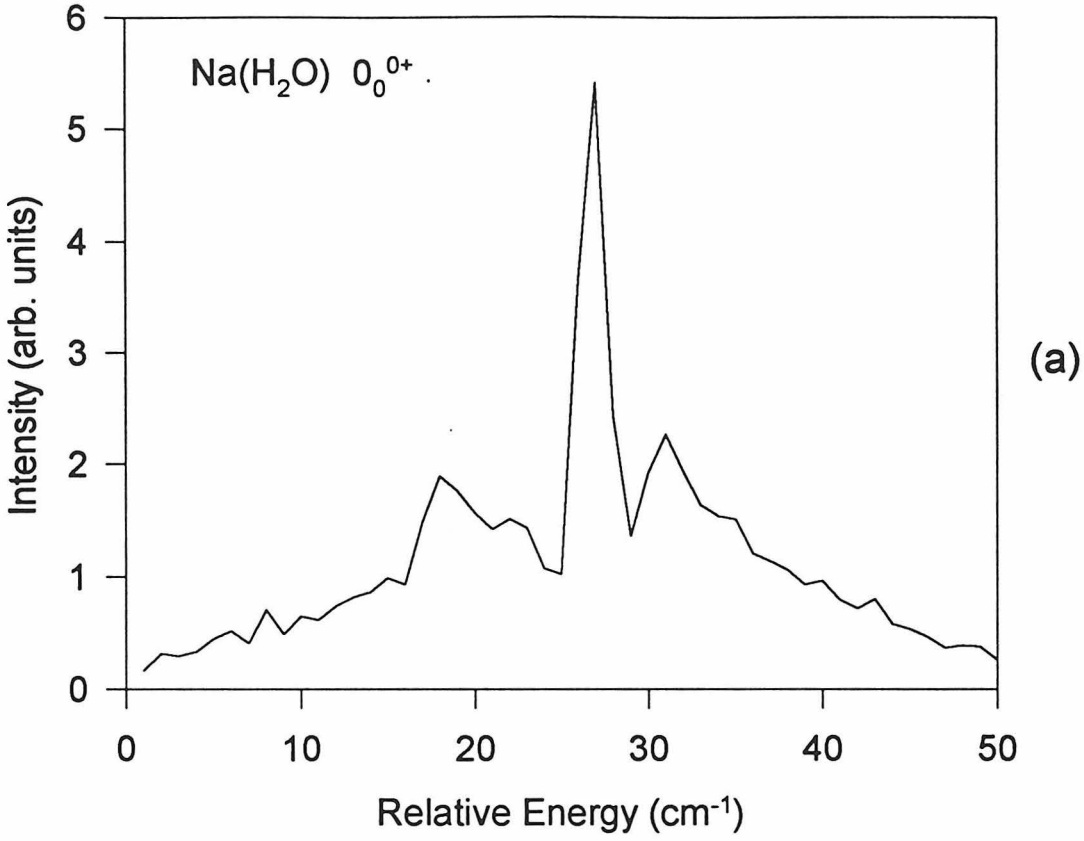
Na(H2O) 0₀⁰⁺
Intensity (arb. units)
Relative Energy (cm-1)
0
1
2
3
4
5
6
0
10
20
30
40
50

(a)

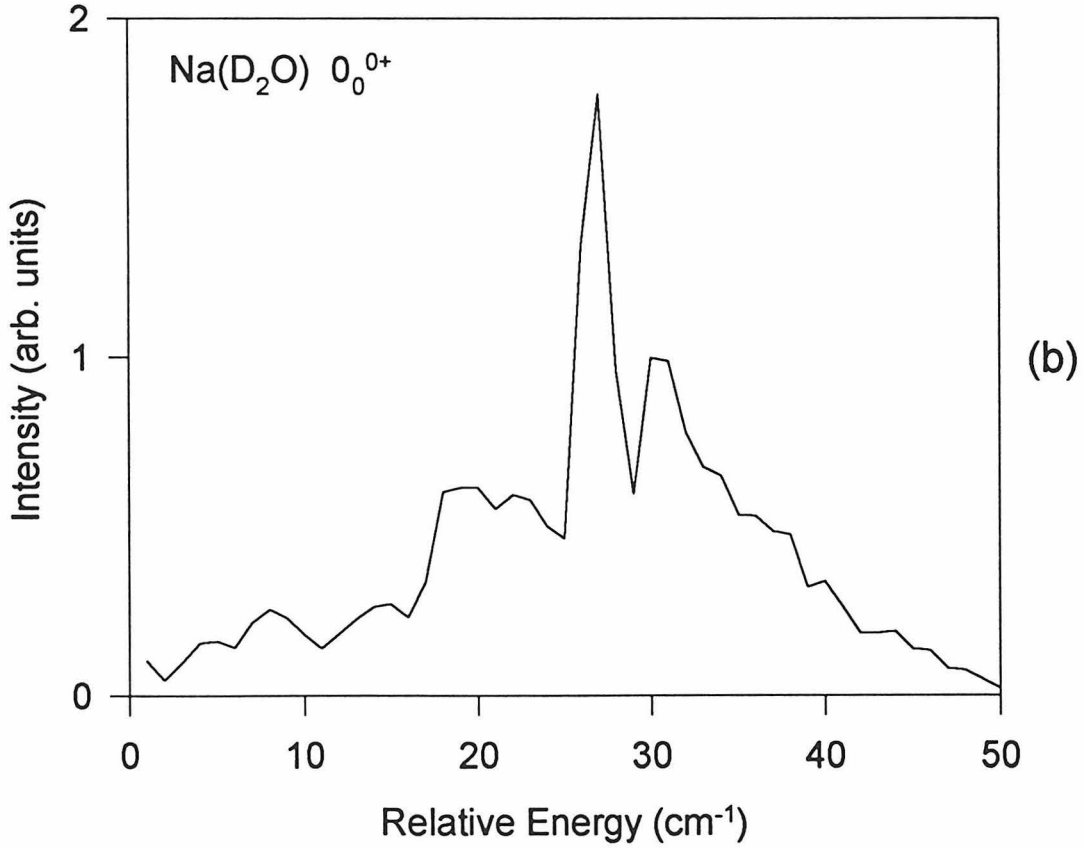
Na(D2O) 0₀⁰⁺
Intensity (arb. units)
Relative Energy (cm-1)
0
1
2
0
10
20
30
40
50

(b)

Figure 4.11: Rotational profiles in the single-photon ZEKE-PFI spectra of the 0_0^{0+} transition of (a) $Na(NH_3)$ and (b) $Na(ND_3)$.

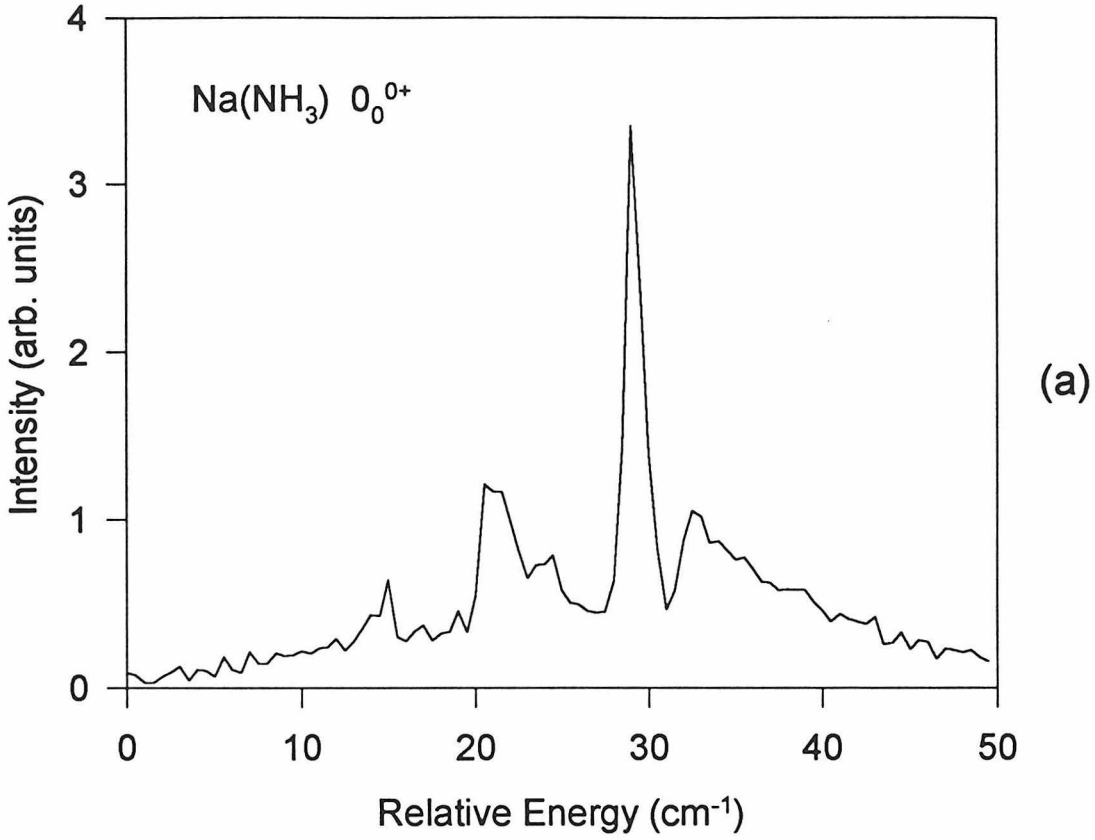
Na(NH3) 0₀⁰⁺
Intensity (arb. units)
Relative Energy (cm⁻¹)
0
1
2
3
4
0
10
20
30
40
50

(a)

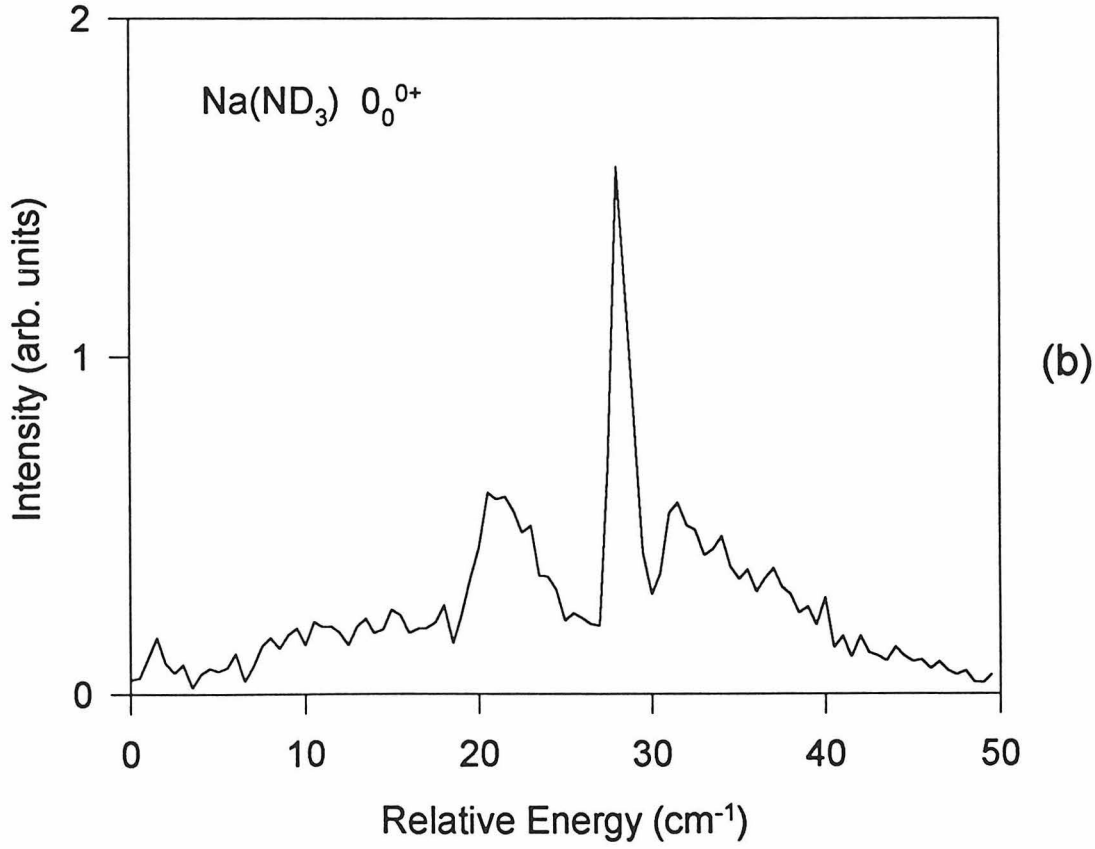
Na(ND3) 0₀⁰⁺
Intensity (arb. units)
Relative Energy (cm⁻¹)
0
1
2
0
10
20
30
40
50

(b)

Figure 4.12: Single-photon ZEKE-PFI spectra showing the 0_0^{0+} transitions of $Na(H_2O)$, Na(HDO), and $Na(D_2O)$.

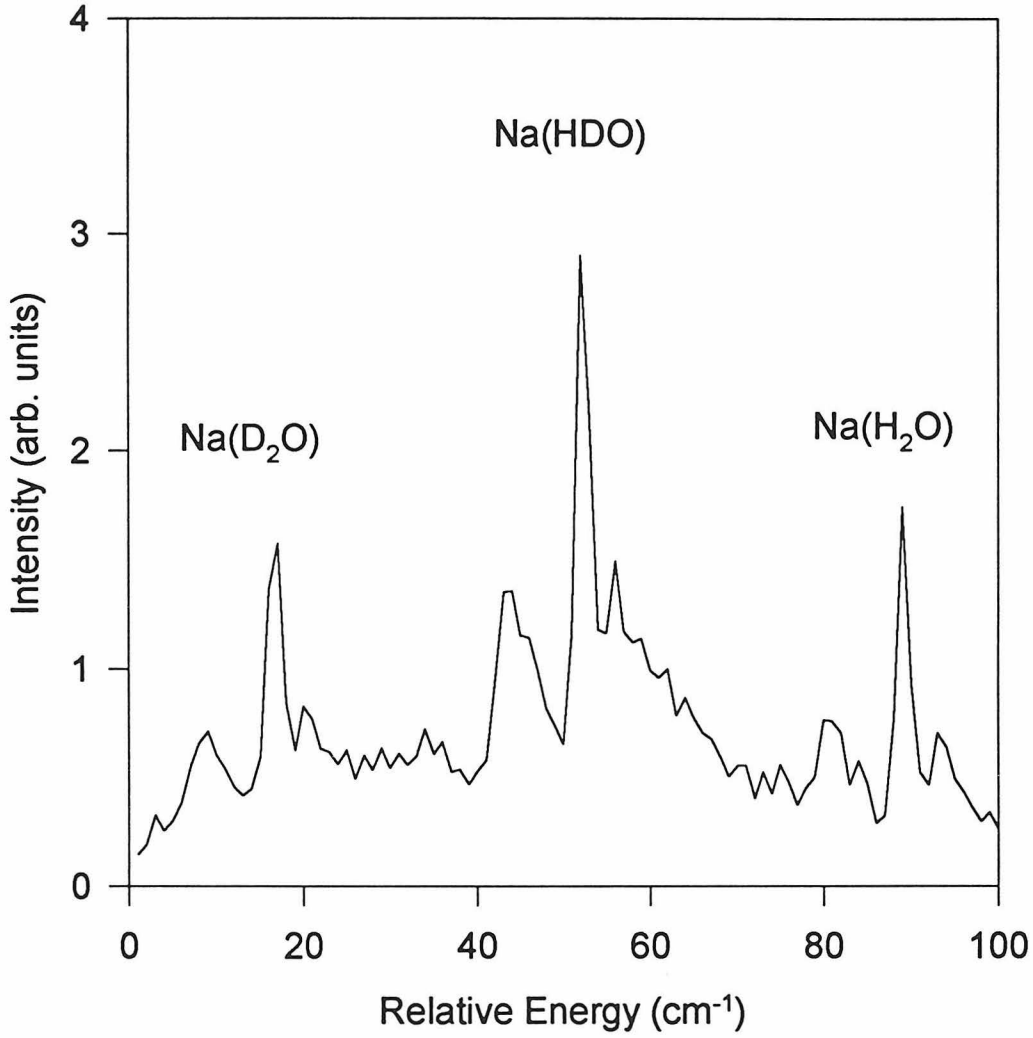
Na(HDO)
Na(D2O)
Na(H2O)
Intensity (arb. units)
Relative Energy (cm-1)
0
1
2
3
4
0
20
40
60
80
100

Table 4.3: Separation of the P and O band heads (D_{PO}), the P and N band heads (D_{PN}), and the ratios of these values from the single-photon ZEKE-PFI spectra of the 0_0^{0+} transitions of $Na(H_2O)$ and $Na(NH_3)$.

	$Na(H_2O)$	$Na(D_2O)$	$Na(NH_3)$	$Na(ND_3)$
D_{PO} (cm^{-1})	8.75	8	7.95	7.25
D_{PN} (cm^{-1})	23.67	23	21.4	20.25
D_{PO}/D_{PN}	0.370	0.348	0.371	0.358

ground state, and very close to the calculated bond length of the ionized complex [28]. The two-color photoionization spectrum cannot have an O branch because of the $\Delta N = 0, \pm 1$ selection rule, but the ZEKE-PFI spectrum can because angular momentum conservation constraints can be satisfied by the angular momentum of the departing electron [39]. It is reasonable, then, to attribute the features that appear in the ZEKE-PFI spectrum, but not the two-color photoionization spectrum, to an O branch and other branches that correspond to higher changes in rotational angular momentum.

A careful inspection of the ZEKE-PFI spectra in Figure 4.14 reveals a distinct shoulder on the low frequency side of the O branch. This is assigned as an N branch. Both the N and O branches rise fairly sharply on the low frequency side because they, like the P branch, form band heads. The assignments of the N and O branches may be confirmed in the following way from the positions of the band heads, which are taken as the points at which the intensity rises sharply. The N values at which the P, O, and N band heads form are found by differentiating the symmetric top line position formulas with respect to N, setting the derivatives equal to zero, and solving for N. By plugging these N values back into the line position formulas, the band head positions can be given as a function of B^+ and B''. It is then found that the ratio of the distance between the P and O band heads (D_{PO}) to the distance between the P and N band heads (D_{PN}) is 0.375. Values for D_{PO}, D_{PN}, and the ratio D_{PO}/D_{PN} are given in Table 4.3, where it may be seen that D_{PO}/D_{PN} is close to 0.375 for all the complexes. The agreement with the expected value is excellent, considering the limited signal to noise ratios and the fact that the complexes with water are not symmetric tops, only nearly so.

Figure 4.13: A comparison of the ZEKE-PFI 0_0^{0+} spectrum and the $\tilde{A}\leftarrow\tilde{X}$ 0_0^0 R2PI spectrum of $Na(NH_3)$. The branch most responsible for each major feature is indicated.

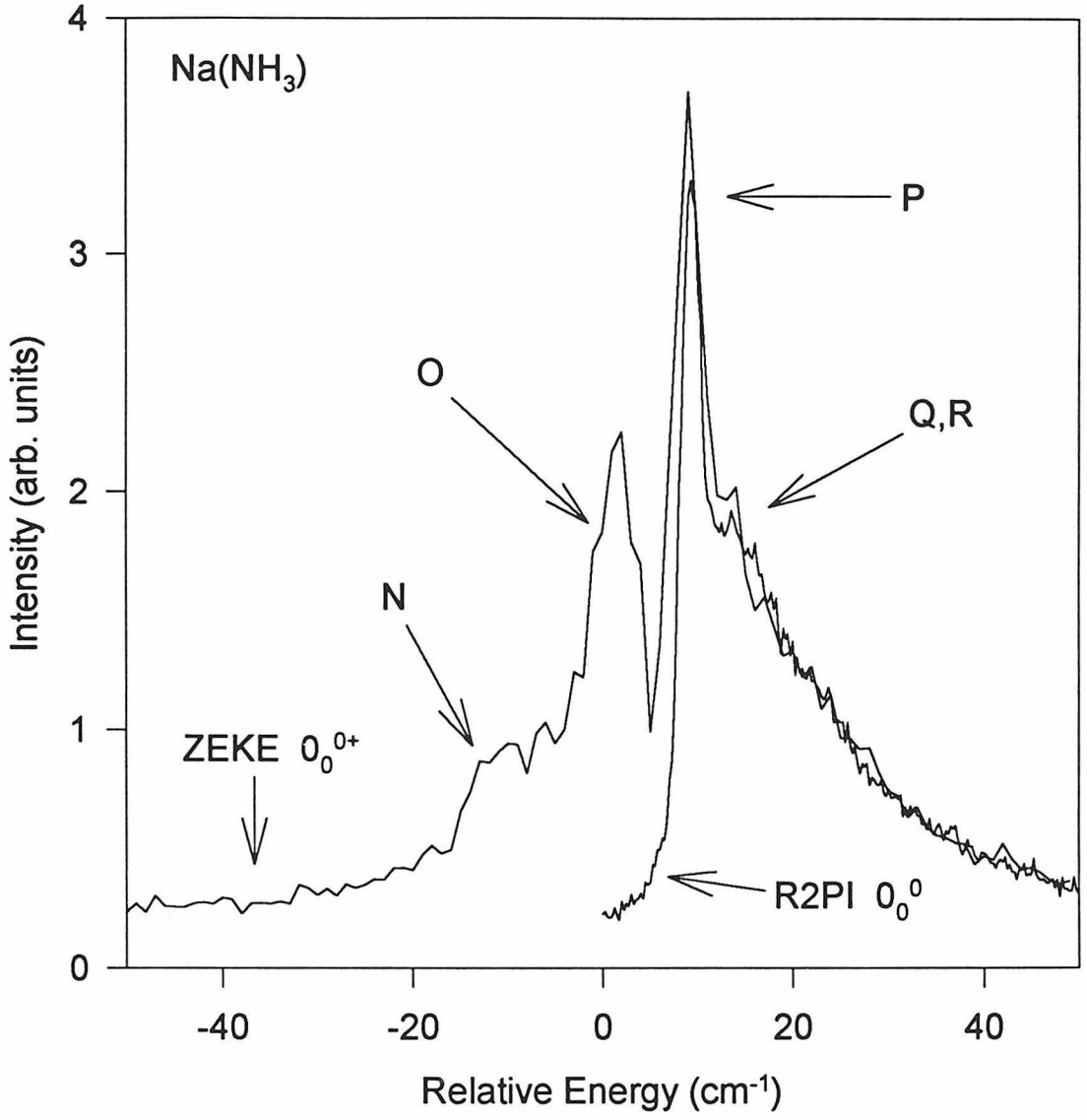
Na(NH3)
P
O
Q,R
N
ZEKE 0₀⁰⁺
R2PI 0₀⁰
Intensity (arb. units)
Relative Energy (cm⁻¹)
0
1
2
3
4
-40
-20
0
20
40

Figure 4.14: Single-photon ZEKE-PFI spectra of (a) $Na(NH_3)$ and (b) $Na(H_2O)$ The branch most responsible for each major feature is indicated.

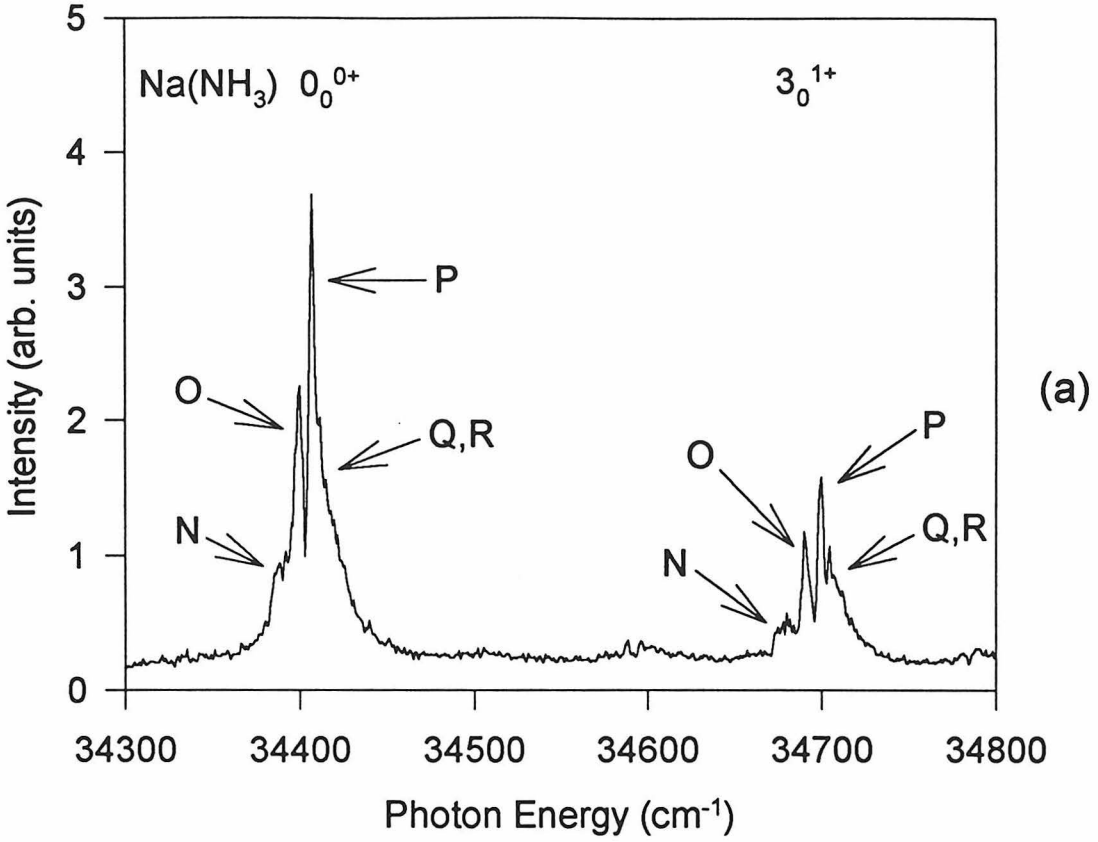
Na(NH3) 0₀⁰⁺
3₀¹⁺
P
O
Q,R
N
O
P
Q,R
N
Intensity (arb. units)
Photon Energy (cm⁻¹)
0
1
2
3
4
5
34300
34400
34500
34600
34700
34800

(a)

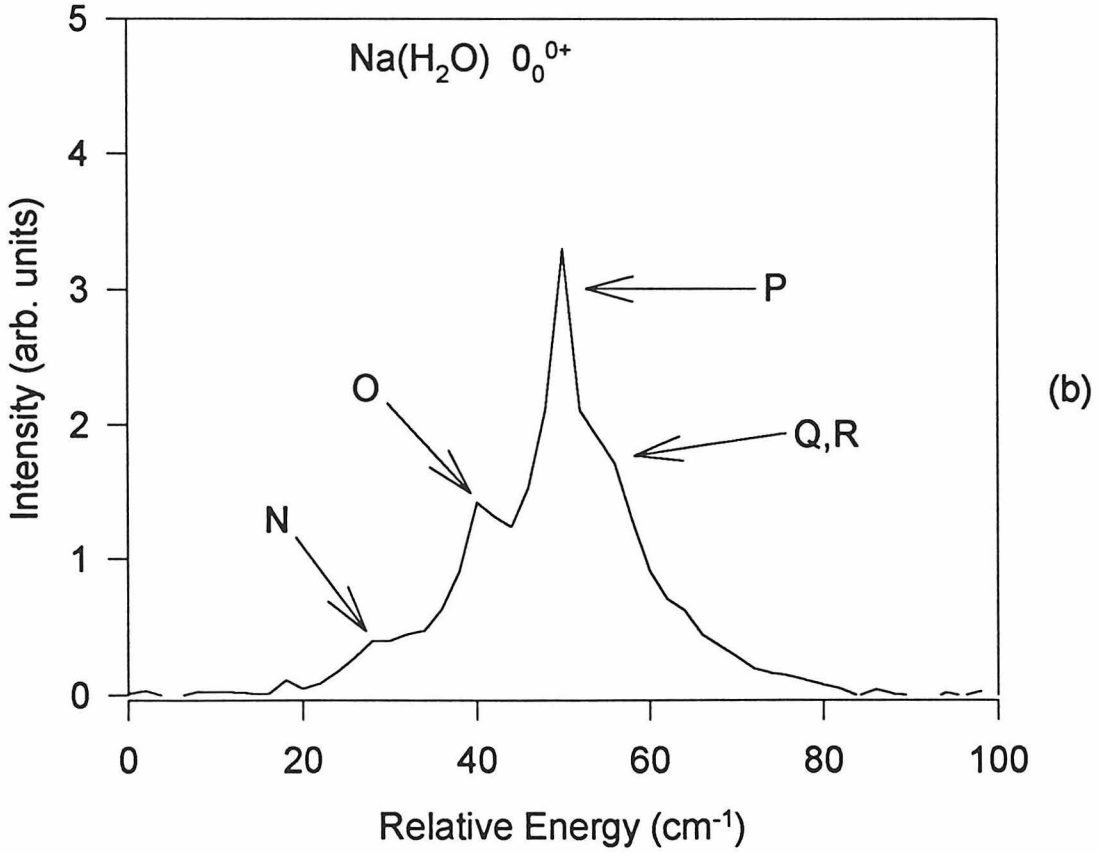
Na(H2O) 0₀⁰⁺
P
O
Q,R
N
Intensity (arb. units)
Relative Energy (cm⁻¹)
0
1
2
3
4
5
0
20
40
60
80
100

(b)

This procedure also gives the following relationship between B^+ and B'' :

$$B'' = (D_{PO}/3)/(1 + D_{PO}/(3 \times B^+)). \tag{4.3}$$

Using the measured D_{PO} value of 7.95 cm^{-1} and a value of B^+ (0.2828 cm^{-1}) derived from the calculated geometry of $Na^+(NH_3)$ (R_{Na-N} = 2.365 Å), it is found that the sodium-ammonia bond shrinks by 5.2±0.5% when the complex is ionized. This is very similar to the change that was observed to occur in the Na-N bond length in the transition from the ground state to the $\tilde{A}$ state. Although this formula does not rigorously apply to the $Na^+(H_2O)$ complex, plugging the measured D_{PO} for this complex (8.75 cm^{-1}) and a value of B^+ (0.3092 cm^{-1}) derived from the calculated geometry (R_{Na-O} = 2.23 Å) into equation (4.3) also gives a 5.2±0.5% reduction in the sodium-water bond length upon ionization. Unfortunately, the rotational constants for these complexes cannot be determined from these spectra at this time because the rotational temperature and relative intensities of the ZEKE-PFI transitions are not known. However, the values of R_{Na-N} (2.495 Å) and R_{Na-O} (2.352 Å) derived for the neutral complexes from the above formula are in excellent agreement with theoretical values of 2.526 Å and 2.355 Å for $Na(NH_3)$ and $Na(H_2O)$, respectively [28, 10].

Using these rotational constants and a rotational temperature of 100 K, the narrow width of the P band heads is explained. A band contour is a function of, among other things, the population in the rotational levels at the experimental temperature as well as the position at which the band head occurs. If the band "turns around" at approximately the same N value at which the population distribution is maximum, the band head will be extremely high and narrow. This occurs for the P band, which, for these complexes turns around at N = 10, close to the same N at which the population distribution is maximum. In the case of the O band, however, the band head occurs at an N value of 20, much higher than the N at which the population maximum occurs. Consequently, this band is wider and the band head less distinct.

ZEKE-PFI spectra of $Na(NH_3)$ taken with different extraction voltages (applied between plates 12.7 mm apart) are shown in Figure 4.15. In (a), it is seen that the

peak positions are the same in both the 4 V and 1 V spectra. The 1 V features are narrower, however, with most of the narrowing occurring on the low frequency side of the bands. This is reasonable, since the smaller extraction field does not "dig" as far into the Rydberg manifold as the 4 V field. In (b), the 0.3 V features are somewhat narrower than the 1 V features, and the peak positions are shifted 1 cm^{-1} to higher energy. Much of this shift is due to the fact that a 0.3 V static field was present in the 1V and 4 V experiments but not in the 0.3 V experiment. The shift is consistent with that expected for a 0.3 V field. The feature marked by an asterisk did not shift with the other features, and is probably not associated with the $Na(NH_3)$ complex. No corresponding peaks occur in the spectra of the other complexes, so this peak will not receive further consideration here.

4.3.2 Two-Color ZEKE-PFI Spectra of $Na(NH_3)$

In an attempt to get better spectral resolution by limiting the number of rotational states contributing to the ZEKE-PFI spectrum, two-color ZEKE-PFI spectra of $Na(NH_3)$ were taken via the $\tilde{A}\leftarrow\tilde{X}$ origin transition. By placing the excitation laser frequency at the P band head of this transition and then moving it in 5 cm^{-1} steps (unless otherwise noted in Figures 4.16-4.18) toward higher frequency, the two-color ZEKE-PFI spectra shown in Figures 4.16-4.18 were obtained. The ionizing laser was scanned over the same energy range in all the spectra, and the distances from the beginning of the scan to the strongest peaks are given in the figures. The spectra are dominated by four nearly equally spaced peaks that spread apart as the excitation laser accesses higher N values. Several other peaks separated by approximately the same spacing are also evident in the spectra. The four strongest peaks are assigned as O, P, Q, and R branch peaks, with the weaker peaks corresponding to higher changes of rotational angular momentum. The O branch peaks are very strong, much like they were in the single photon spectra, and this makes the assignment of the O branch in the single photon spectra more plausible.

It is evident that as the peaks spread out at higher N values, they also shift to

Figure 4.15: Single-photon ZEKE-PFI spectra of the 0_0^{0+} transition of $Na(NH_3)$ under different pulsed field conditions. The peak marked by the asterisk is not believed to result from PFI of this complex.

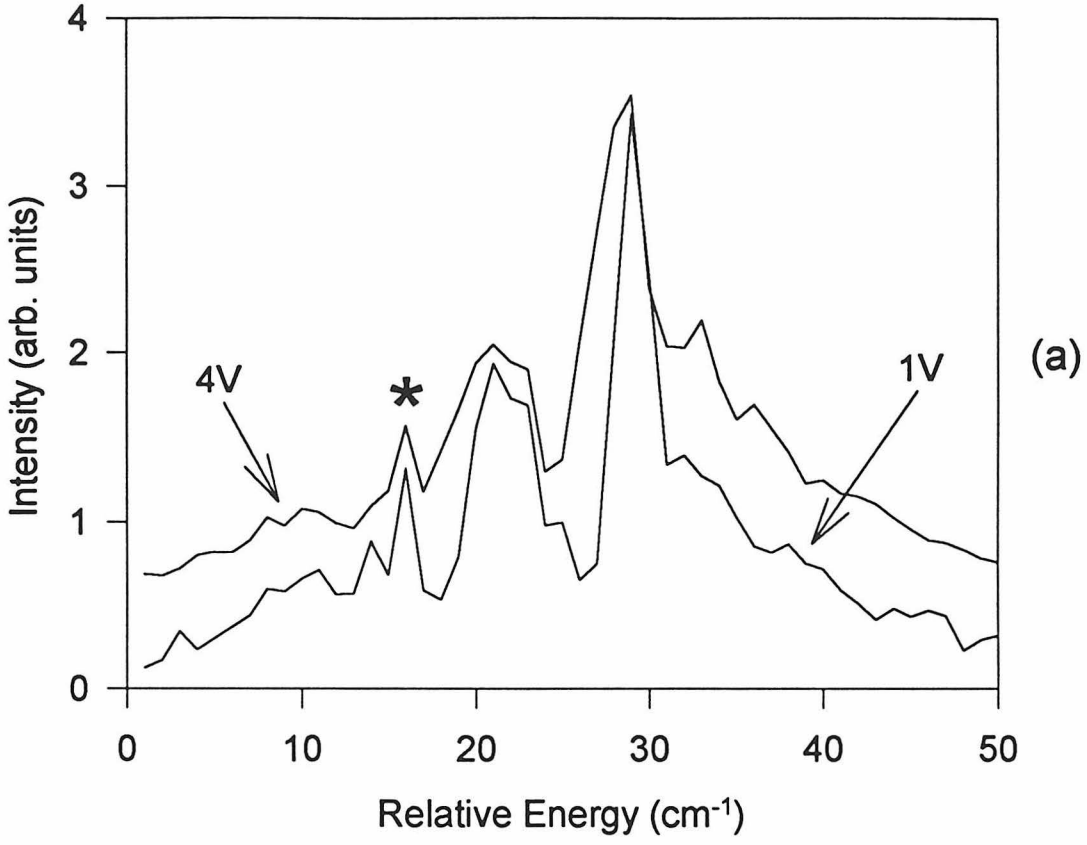
4
3
2
1
0
Intensity (arb. units)
4V
*
1V
(a)
0
10
20
30
40
50
Relative Energy (cm-1)

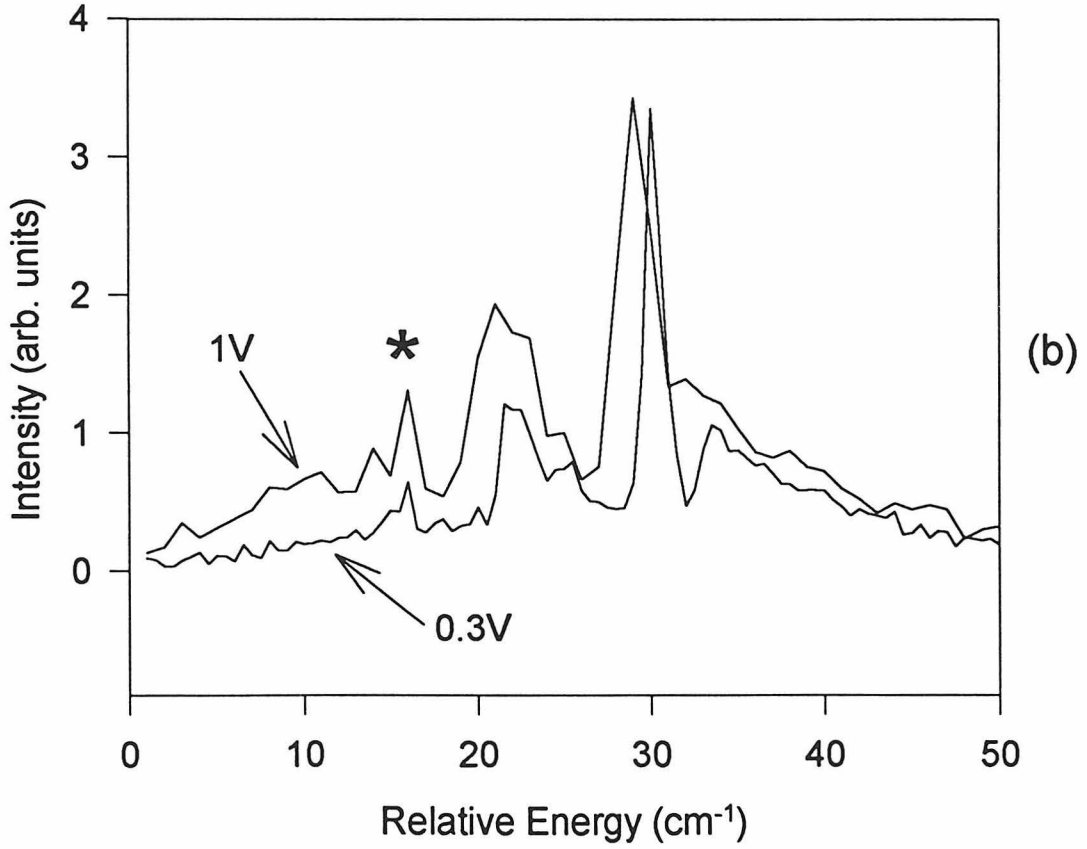
4
3
2
1
0
Intensity (arb. units)
1V
*
(b)
0.3V
0
10
20
30
40
50
Relative Energy (cm-1)

Figure 4.16: (a) R2PI scan of the $\tilde{A}\leftarrow\tilde{X}$ 0_0^0 transition of $Na(NH_3)$. The arrows indicate the points in the band excited by the first laser in the two-color ZEKE-PFI spectra shown in panels b and c of this figure and in Figures 4.17 and 4.18. (b) and (c) Two-color ZEKE-PFI spectra via the $\tilde{A}$ 0^0 state of $Na(NH_3)$. The positions of the main peaks relative to the beginning of the scan are given in cm^{-1}, and the position of excitation relative to the band head is noted.

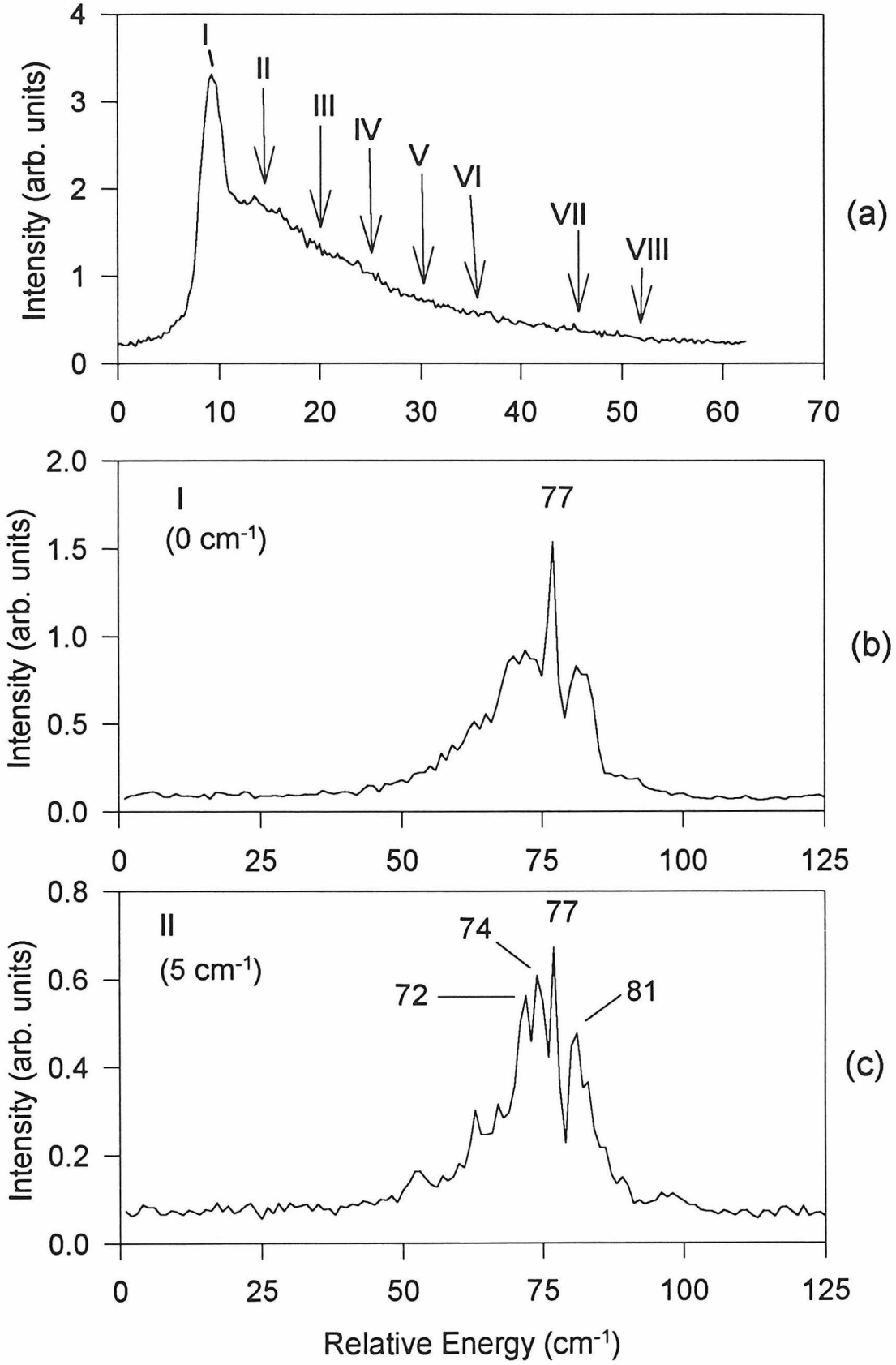
Intensity (arb. units)
I
II
III
IV
V
VI
VII
VIII
(a)
I
(0 cm-1)
77
(b)
II
(5 cm-1)
74
77
72
81
(c)
Relative Energy (cm-1)

Figure 4.17: Two-color ZEKE-PFI spectra via the $\tilde{A}$ 0^0 state of $Na(NH_3)$. The positions of the main peaks relative to the beginning of the scan are given in cm^{-1}, and the position of excitation relative to the band head is noted.

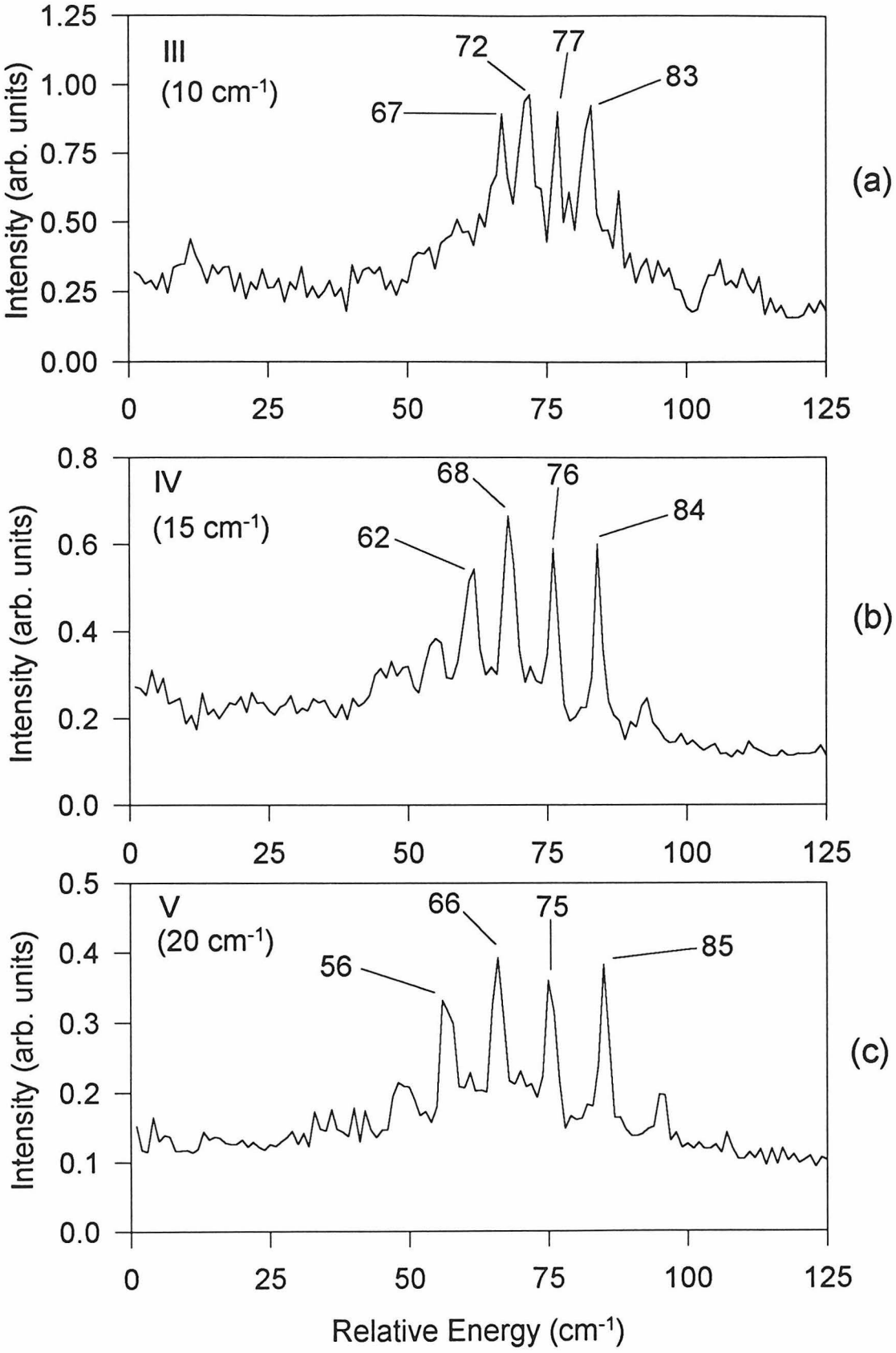
III
(10 cm-1)
72
77
83
67
(a)
IV
(15 cm-1)
68
76
84
62
(b)
V
(20 cm-1)
66
75
85
56
(c)
Intensity (arb. units)
Relative Energy (cm-1)

Figure 4.18: Two-color ZEKE-PFI spectra via the $\tilde{A}$ 0^0 state of $Na(NH_3)$. The positions of the main peaks relative to the beginning of the scan are given in cm^{-1}, and the position of excitation relative to the band head is noted.

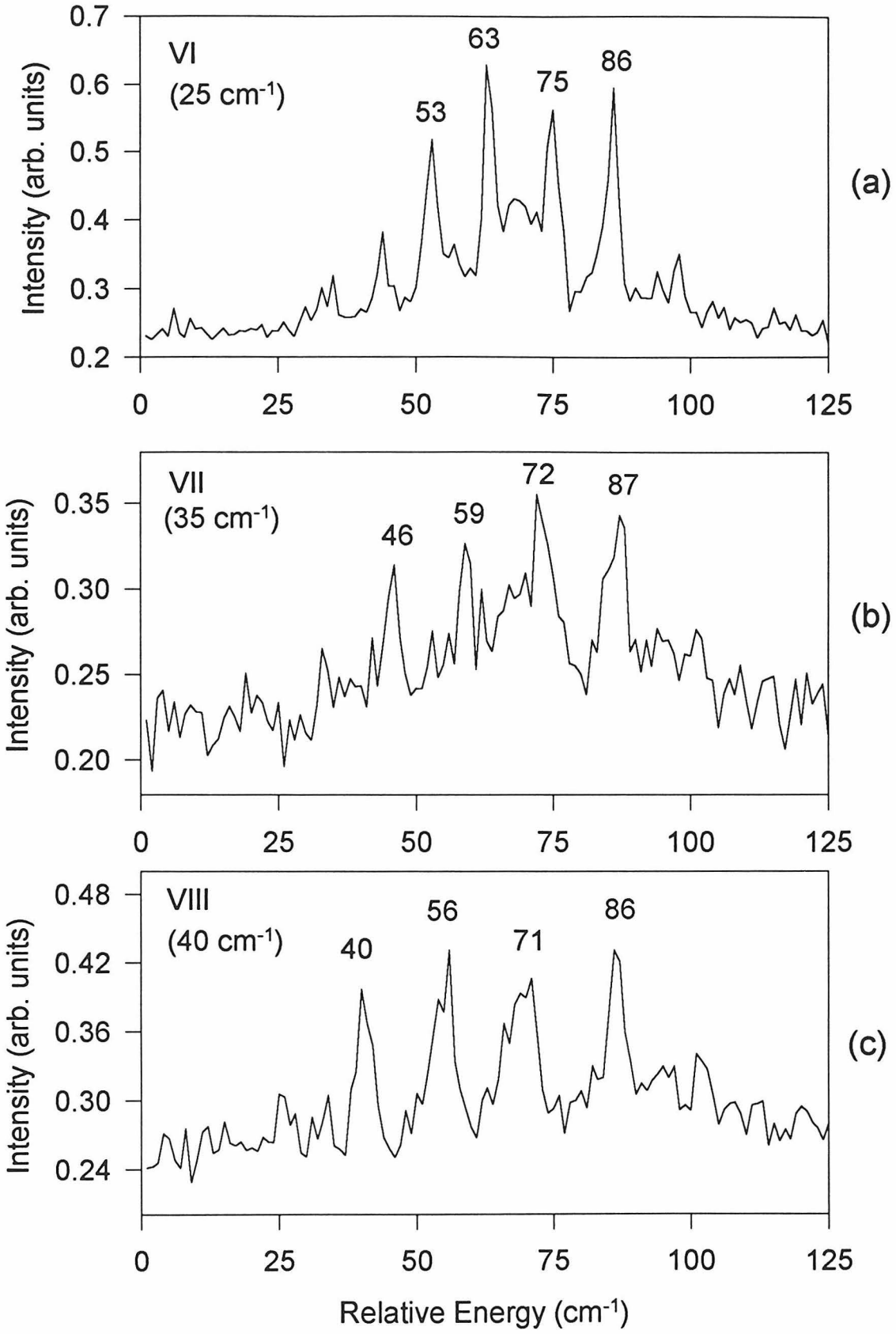
VI
(25 cm-1)
53
63
75
86
(a)
Intensity (arb. units)
0.7
0.6
0.5
0.4
0.3
0.2
VII
(35 cm-1)
46
59
72
87
(b)
Intensity (arb. units)
0.35
0.30
0.25
0.20
VIII
(40 cm-1)
40
56
71
86
(c)
Intensity (arb. units)
0.48
0.42
0.36
0.30
0.24
0
25
50
75
100
125
Relative Energy (cm-1)

lower frequency. This results from the $(B^+ - B')N^2$ term in the line position formulas, where B′ is the rotational constant in the $\tilde{A}$ state. The Q peak starts at 77 cm^{-1} in the the first few scans, then moves to lower energy, ending 6 cm^{-1} below where it started. Note also that the R peaks for the last three spectra occur at the same location, 86-87 cm^{-1} into the scan. This is an R band head, and it shows that the sodium-ammonia bond is shorter in the $\tilde{A}$ state than in the ion. The location of the R band head shows that the bond increases its length by $1.5 \pm 0.2\%$ as the complex is ionized from the $\tilde{A}$ state. Unfortunately, the resolution and S/N ratios of the ZEKE-PFI spectra are not high enough to allow N values to be assigned to the spectra, so only the relative change in the B rotational constant can be determined at this time.

Although the single-photon ZEKE-PFI spectra strongly suggest that transitions involving negative changes in rotational angular momentum, the O branch in particular, are stronger than the corresponding transitions involving positive changes in rotational angular momentum, the limited rotational resolution and the absence of R, S, T, etc. band heads makes this difficult to assess. Perhaps the best way to gauge the strengths of the S, T, U, etc. branches is by again comparing the $Na(NH_3)$ 0_0^{0+} ZEKE-PFI profile with the rotational contour of the $Na(NH_3)$ $\tilde{A} \leftarrow \tilde{X}$ origin transition, which cannot have S, T, U, etc. branches. The widths of the spectra, shown in Figure 4.13, from the P band head to higher frequency, are nearly the same, and this indicates that branches corresponding to positive changes in rotational angular momentum of more than one unit do not make large contributions to the ZEKE-PFI band profile.

In the two photon ZEKE-PFI spectra, however, it is very clear that the O branch is much stronger than the S branch, and that there is a greater propensity for transitions involving negative changes in rotational angular momentum than for those involving positive changes. Enhanced intensity in the O, N, M, etc. branches relative to the S, T, U, etc. branches is commonly observed in ZEKE-PFI spectroscopy, and is believed to result from field-assisted rotational autoionization [40, 41]. This occurs when the laser-excited Rydberg states that converge to some rotational level of the molecule but are too low to be ionized by the pulsed electric field couple with Rydberg states of

higher principal quantum number that converge toward a lower rotational energy level of the molecule and can be ionized by the pulsed electric field. The system evolves from the initial Rydberg states to the field-ionizable Rydberg states during the delay between the laser pulse and the pulsed ionizing field, and this transfer of population to the Rydberg states converging toward the lower rotational level increases the strength of the ZEKE-PFI peak corresponding to that rotational level when the Rydberg states are field ionized.

Stray electric fields are thought to enhance the coupling between the Rydberg manifolds, which becomes more efficient as the B rotational constant of the molecule decreases. This happens because as the rotational constant decreases, the principal quantum numbers of the states involved in the mixing increase, making them more susceptible to Stark mixing induced by small electric fields. For molecules with B^+ rotational constants comparable to the $Na^+(NH_3)$ complex, changes in N as large as -4 have been observed in electric fields of only 0.05 V/cm. Considerable effort has gone into understanding these effects in better characterized molecules such as N_2 and Na_2, but an in-depth analysis of the ZEKE-PFI intensities in the $Na(NH_3)$ and $Na(H_2O)$ complexes will be postponed until they are better characterized.

4.4 Conclusions

From the ZEKE-PFI spectra presented in this chapter, the intermolecular stretching and bending vibrational frequencies have been measured for both the neutral and ionized forms of the sodium-ammonia complex. Only the intermolecular stretching frequency was measured for the $Na^+(H_2O)$ complex, but the bending frequencies should be measurable by two-color ZEKE-PFI spectroscopy when the $\tilde{A}$ state of the neutral complex is located. In order to map the IPESs, anharmonicities will also have to be measured. The ZEKE-PFI spectra presented here exhibit progressions in the vibrational modes from which anharmonicities can be determined once adequate signal and a better assignment of the rotational structure in the bands are obtained. My ZEKE-PFI spectra showed that the sodium-water and sodium-ammonia bond

lengths shrink 5.2 $\pm$ 0.5% when the complexes are ionized. If the geometries of the neutral complexes can be determined by other methods, ZEKE-PFI spectroscopy can give the geometries of the ionized complexes. The two-color ZEKE-PFI spectra of $Na(NH_3)$ indicate that ZEKE-PFI alone can give the ion geometry if the spectral resolution can be improved.

Bibliography

[1] W. Rudolph, M.H. Brooker and C.C. Pye, *J. Phys. Chem.*, 99:3793, 1995.

[2] J.C. Polanyi and J. Wang, *J. Phys. Chem.*, 99:13691, 1995.

[3] E.D. Glendening, *J. Am. Chem. Soc.*, 118:2473, 1996.

[4] J.E. Combariza and N.R. Kestner, *J. Phys. Chem.*, 99:2717, 1995.

[5] F.F. Abraham, M.R. Mruzik and G.M. Pound, *Faraday Discuss. Chem. Soc.*, 61:34, 1976.

[6] M.D. Toney, E. Hohenester, S.W. Cowan, and J.N. Jansonius, *Science*, 261:756, 1993.

[7] I. Džidić and P. Kebarle, *J. Phys. Chem.*, 74:1466, 1970.

[8] A.W. Castleman, Jr., P.M. Holland, D.M. Lindsay and K.I. Peterson, *J. Am. Chem. Soc.*, 100:6039, 1978.

[9] C.W. Bauschlicher, Jr., S.R. Langhoff, H. Partridge, J.E. Rice and A. Komornicki, *J. Chem. Phys.*, 95:5142, 1991.

[10] K. Hashimoto and K. Morokuma, *J. Am. Chem. Soc.*, 116:11436, 1994.

[11] K. Hashimoto and K. Morokuma, *J. Am. Chem. Soc.*, 117:4151, 1995.

[12] T.J. Selegue and J.M. Lisy, *J. Phys. Chem.*, 96:4143, 1992.

[13] R.J. Saykally and G.A. Blake, *Science*, 259:1570, 1993.

[14] C.P. Schulz, R. Haugstätter, H.U. Tittes and I.V. Hertel, *Phys. Rev. Letters*, 57:1703, 1986.

[15] C. Nitsch, C.P. Schulz, A. Gerber, W. Zimmermann-Edling and I.V. Hertel, *Z. Physik D*, 22:651, 1992.

[16] L. Manceron, A. Loutellier and J.P Perchard, *Chem. Phys.*, 92:75, 1985.

[17] P.F. Meier, R.H. Hauge and J.L. Margrave, *J. Am. Chem. Soc.*, 100:2108, 1978.

[18] L.A. Curtiss and J.A. Pople, *J. Chem. Phys.*, 82:4230, 1985.

[19] J. Bentley and I. Carmichael, *J. Phys. Chem.*, 85:3821, 1981.

[20] M. Trenary, H.F. Schaefer III and P. Kollman, *J. Chem. Phys.*, 68:4047, 1978.

[21] I.V. Hertel, C. Hüglin, C. Nitsch and C.P. Schulz, *Phys. Rev. Letters*, 67:1767, 1991.

[22] F. Misaizu, K. Tsukamoto, M. Sanekata and K. Fuke, *Chem. Phys. Letters*, 188:241, 1992.

[23] R. N. Barnett and U. Landman, *Phys. Rev. Letters*, 70:1775, 1993.

[24] K. Müller-Dethlefs, M. Sander, and E.W. Schlag, *Z. Naturforsch.*, A39:1089, 1984.

[25] G. Reiser, W. Habenicht, K. Müller-Dethlefs, and E.W. Schlag, *Chem. Phys. Letters*, 152:119, 1988.

[26] K. Müller-Dethlefs and E.W. Schlag, *Ann. Rev. Phys. Chem.*, 42:109, 1991.

[27] R. Lindner, H.J. Dietrich and K. Müller-Dethlefs, *Chem. Phys. Letters*, 228:417, 1994.

[28] J.C. Greer, C. Hüglin, I.V. Hertel and R. Ahlrichs, *Z. Physik D*, 30:69, 1994.

[29] C. Nitsch, C. Hüglin, I.V. Hertel and C.P. Schulz, *J. Chem. Phys.*, 101:6559, 1994.

[30] G. Herzberg, *Molecular Spectra and Molecular Structure*, Vol. 3 (Van Nostrand, Princeton, NJ, 1966).

[31] G. Herzberg and E. Teller, *Z. Phys. Chem.*, 21:410, 1933.

[32] R.S. Mulliken and E. Teller, *Phys. Rev.*, 61:283, 1942.

[33] X. Song, C.W. Wilkerson, J. Lucia, S. Pauls, and J.P. Reilly, *Chem. Phys. Letters*, 174:377, 1990.

[34] J. Flügge and P. Botschwina, in *Structures and Dynamics of Clusters*, Universal Academy Press, 1996.

[35] A. Loutellier, L. Manceron, and J.P. Perchard, *Chem. Phys.*, 146:179, 1990.

[36] G. Reiser, D. Rieger, T.G. Wright, K. Müller-Dethlefs, and E.W. Schlag, *J. Phys. Chem.*, 97:4335, 1993.

[37] M.C.R. Cockett, H. Ozeki, K. Okuyama, and K. Kimura, *J. Chem. Phys.*, 98:7763, 1993.

[38] C.T. Scurlock, S.H. Pullins, J.E. Reddic, and M.A. Duncan, *J. Chem. Phys.*, 104:4591, 1996.

[39] K. Müller-Dethlefs, *J. Chem. Phys.*, 95:4821, 1991.

[40] F. Merkt, H.H. Fielding, and T.P. Softly, *Chem. Phys. Letters*, 202:153, 1993.

[41] F. Merkt and T.P. Softly, *Phys. Rev. A*, 46:302, 1992.

Chapter 5 Conclusions and Future Directions

The work on the benzene-ammonia dimer revealed that the complex has a structure in which the ammonia donates a hydrogen bond to the benzene similar to the amino-aromatic hydrogen bonding observed in some proteins. Although valuable structural information has been obtained, much more work will need to be done in order to develop an accurate IPES for this complex. Much of this work will involve high-resolution far-IR investigations of the intermolecular vibrational modes of the complex. To data, this work has proceeded slowly on account of the slow scanning rate of tunable far-IR laser sideband spectrometers. However, new methods of generating far-IR light are being developed which offer much faster scanning.

In one method being developed by the Blake group, GaAs photomixers are used to generate FIR light at a frequency equal to the difference of the frequencies of two diode laser beams impinging on the photomixer [1]. This method gives broad coverage, including the region from 200 cm^{-1} to 400 cm^{-1} where other light sources do not perform well. The necessary equipment is also relatively inexpensive, making it more accessible to more laboratories.

Free electron lasers also give access to the FIR and MIR spectral regions [2]. Although these sources do not have high spectral resolution, they can be used to map out the vibrational spectra of complexes quickly. This data will provide a coarse guide for IPESs, and will show where high resolution FIR instruments should be scanned in order to get more detailed data.

Although only limited structural information on the sodium complexes was acquired, my results suggest that the geometries of larger complexes, which serve as models of ion channels and binding sites, might be measurable with ZEKE-PFI techniques. Although the B rotational constants of these complexes will be smaller, the

ZEKE-PFI spectra shown here exhibited distinct features with spacings one to two orders of magnitude larger than B. In the single photon spectra, these were the N and O band heads, while in the two-color spectra, they were the peaks in the P, Q, and R branches. Improved signal, resolution, and possibly the measurement of the geometries of the neutral complexes will be required to determine the geometries of larger complexes with alkali metal ions.

Several improvements in the experimental equipment and procedures can be made. First, an order of magnitude increase in signal can be achieved by reducing the distance between the pick-up source and the ionization region. Also, since the clusters formed in this source maintain a velocity component in the direction of the sodium beam, the cluster signal can be increased by pointing the source in a direction that compensates for this. Second, the signal-to-noise ratio can be improved by taking steps to prevent electrons other than PFI electrons from reaching the detector, and the resolution can be improved by using smaller extraction pulses. And third, mass-analyzed threshold ionization (MATI) can be employed to give mass-resolved threshold photoionization spectra of larger clusters [3].

New light sources will further extend the capabilities of ZEKE-PFI spectroscopy. High-resolution OPOs recently developed in the Blake lab will soon be used in ZEKE-PFI experiments on sodium-water and sodium-ammonia complexes [4]. These OPOs give access to the IR region of the spectrum where the $\tilde{A}\leftarrow\tilde{X}$ transitions of these complexes are located. This transition must be used in two-color ZEKE-PFI experiments because the lifetimes of higher electronic states are only $\sim$30 ps [5]. OPOs can also be used to probe the vibrational modes of the solvent molecules. The VIS/IR light from OPOs can also be used in double-resonance experiments employing microwave radiation to obtain accurate geometries for the neutral complexes. Coverage in the IR and high spectral resolution make OPOs the ideal light sources for investigating complexes with alkali metals.

Finally, improved theoretical methods for generating IPESs will be needed. Ab initio calculations can give accurate information for small complexes, but their results on larger complexes are less reliable. There is an urgent need for methods that can

give an IPES by inverting experimental vibrational data. If such methods can be developed, they will make the information obtained with ZEKE-PFI spectroscopy more useful in the modeling of biological systems in which the interactions between cations and other molecules are important.

Bibliography

[1] P. Chen and G.A. Blake, *Appl. Phys. Lett.*, in preparation.

[2] W.B. Colson, *Nucl. Inst. A*, 358:532, 1995.

[3] L. Zhu and P. Johnson, *J. Chem. Phys.*, 94:5769, 1991.

[4] S. Wu and G.A. Blake, *Appl. Optics*, accepted.

[5] C.P. Schulz, J. Höhndorf, P. Brockhaus, F. Noack, and I.V. Hertel, *Chem. Phys. Letters*, 239:18, 1995.

Appendix A The G_{36} MS Group

Because the benzene-ammonia dimer is non-rigid due to free internal rotation about the benzene C_6 axis, nuclear spin statistical weights must be determined with the methods of permutation-inversion (PI) theory. This involves generating the character table for the appropriate molecular symmetry group, finding the symmetry that the overall wavefunction must have in order to satisfy the Pauli exclusion principle, determining the symmetries of the rotational, torsional, and nuclear spin wavefunctions, and then finding which combinations of these give the correct symmetry for the overall wavefunction. PI theory and molecular symmetry (MS) groups are discussed in Bunker [1], and the application of these methods, as well as Wilson's method for determining nuclear spin statistical weights [2], to the benzene-water dimer is thoroughly discussed by Gotch [3].

The reference configuration upon which this analysis is based has the NH_3 located above the benzene plane, its nitrogen atom on the benzene C_6 axis and its protons pointing toward the benzene. The C_3 axis of NH_3 and the C_6 axis of C_6H_6 are collinear. Rotation of the NH_3 and C_6H_6 about their symmetry axes is considered to be feasible, while rotations of the NH_3 and C_6H_6 individually about their other axes are not feasible. Such rotations would require breaking the bond holding the subunits together, a process with a prohibitively high barrier. ρ is the angle associated with the internal rotation, m is the quantum number for this motion, and ψ_{tor}, the wavefunction describing the internal rotation is $e^{im\rho}$.

Using the methods outlined in Bunker, the MS group was determined to be G_{36}. The class structure shown in Table A.1 was determined, and the equivalent rotations generated by each class are given, as discussed by Bunker. The character table shown in Table A.2 was then obtained. These were used to determine the symmetries of the rotational and torsional wavefunctions, which are shown in Tables A.3 and A.4.

Only the protons were considered in the determination of the symmetry of the

Table A.1: Class structure of the G_{36} MS group

Class	Permutation-Inversion Operations	Equivalent Rotations
CL1	E	R_z^0, ρ
CL2	(123456)	$R_z^{\pi/3}$, $\rho+\pi/3$
	(165432)	$R_z^{\pi/3}$, $\rho+\pi/3$
CL3	(135)(246)	$R_z^{2\pi/3}$, $\rho+2\pi/3$
	(153)(264)	$R_z^{2\pi/3}$, $\rho+2\pi/3$
CL4	(14)(25)(36)	R_z^{π}, $\rho+\pi$
CL5	(789)	R_z^0, $\rho+2\pi/3$
	(798)	R_z^0, $\rho+2\pi/3$
CL6	(123456)(789)	$R_z^{\pi/3}$, $\rho-\pi/3$
	(165432)(798)	$R_z^{\pi/3}$, $\rho-\pi/3$
CL7	(123456)(798)	$R_z^{\pi/3}$, $\rho+\pi$
	(165432)(789)	$R_z^{\pi/3}$, $\rho+\pi$
CL8	(135)(246)(789)	$R_z^{2\pi/3}$, ρ
	(153)(264)(798)	$R_z^{2\pi/3}$, ρ
CL9	(135)(246)(798)	$R_z^{2\pi/3}$, $\rho+4\pi/3$
	(153)(264)(789)	$R_z^{2\pi/3}$, $\rho+4\pi/3$
CL10	(14)(25)(36)(789)	R_z^{π}, $\rho+5\pi/3$
	(14)(25)(36)(798)	R_z^{π}, $\rho+5\pi/3$
CL11	(12)(36)(45)(78)*	$R_{\pi/6}^{\pi}$, $4\pi/3-\rho$
	(12)(36)(45)(79)*	$R_{\pi/6}^{\pi}$, $4\pi/3-\rho$
	(12)(36)(45)(89)*	$R_{\pi/6}^{\pi}$, $4\pi/3-\rho$
	(14)(23)(56)(78)*	$R_{\pi/6}^{\pi}$, $4\pi/3-\rho$
	(14)(23)(56)(79)*	$R_{\pi/6}^{\pi}$, $4\pi/3-\rho$
	(14)(23)(56)(89)*	$R_{\pi/6}^{\pi}$, $4\pi/3-\rho$
	(16)(25)(34)(78)*	$R_{\pi/6}^{\pi}$, $4\pi/3-\rho$
	(16)(25)(34)(79)*	$R_{\pi/6}^{\pi}$, $4\pi/3-\rho$
	(16)(25)(34)(89)*	$R_{\pi/6}^{\pi}$, $4\pi/3-\rho$
CL12	(15)(24)(78)*	$R_{\pi/3}^{\pi}$, $5\pi/3-\rho$
	(15)(24)(79)*	$R_{\pi/3}^{\pi}$, $5\pi/3-\rho$
	(15)(24)(89)*	$R_{\pi/3}^{\pi}$, $5\pi/3-\rho$
	(26)(35)(78)*	$R_{\pi/3}^{\pi}$, $5\pi/3-\rho$
	(26)(35)(79)*	$R_{\pi/3}^{\pi}$, $5\pi/3-\rho$
	(26)(35)(89)*	$R_{\pi/3}^{\pi}$, $5\pi/3-\rho$
	(13)(46)(78)*	$R_{\pi/3}^{\pi}$, $5\pi/3-\rho$
	(13)(46)(79)*	$R_{\pi/3}^{\pi}$, $5\pi/3-\rho$
	(13)(46)(89)*	$R_{\pi/3}^{\pi}$, $5\pi/3-\rho$

Table A.2: Character table of the G_{36} MS group

Γ	CL1	CL2	CL3	CL4	CL5	CL6	CL7	CL8	CL9	CL10	CL11	CL12
A_1	1	1	1	1	1	1	1	1	1	1	1	1
A_2	1	1	1	1	1	1	1	1	1	1	-1	-1
B_1	1	-1	1	-1	1	-1	-1	1	1	-1	1	-1
B_2	1	-1	1	-1	1	-1	-1	1	1	-1	-1	1
E_1	2	1	-1	-2	-1	-2	1	-1	2	1	0	0
E_2	2	-1	-1	2	-1	2	-1	-1	2	-1	0	0
E_3	2	1	-1	-2	-1	1	-2	2	-1	1	0	0
E_4	2	-1	-1	2	-1	-1	2	2	-1	-1	0	0
E_5	2	1	-1	-2	2	1	1	-1	-1	-2	0	0
E_6	2	-1	-1	2	2	-1	-1	-1	-1	2	0	0
E_7	2	2	2	2	-1	-1	-1	-1	-1	-1	0	0
E_8	2	-2	2	-2	1	-1	1	-1	-1	1	0	0

Table A.3: Symmetry of the rotational wavefunctions of $C_6H_6(^{14}NH_3)$.

Rotational State	Γ_{rot}
k=0,J even	A_1
k=0, J odd	A_2
k=6q±1	E_5
k=6q±2	E_6
k=6q±3	$B_1 + B_2$
k=6q±6	$A_1 + A_2$

Table A.4: Symmetry of the torsional wavefunctions of $C_6H_6(^{14}NH_3)$.

Torsional State	Γ_{tor}
m=0	A_1
m=±1	E_3
m=±2	E_4
m=±3	$B_1 + B_2$

Table A.5: The reducible representation of the nuclear spin wavefunctions of $C_6H_6(^{14}NH_3)$.

Class	Number of unchanged wavefunctions
CL1	512
CL2	16
CL3	32
CL4	64
CL5	128
CL6	4
CL7	4
CL8	8
CL9	8
CL10	16
CL11	32
CL12	64

overall wavefunction and of the nuclear spin wavefunctions. Carbon atoms have no spin, and there is only one nitrogen atom (spin 1), so no exchange is possible. The complete wavefunction ψ is given by

$$\psi = \psi_e \psi_v \psi_r \psi_{tor} \psi_{spin} \tag{A.1}$$

where ψ_e is the electronic wavefunction, ψ_v is the vibrational wavefunction, ψ_r is the rotational wavefunction, ψ_{tor} is the torsional wavefunction, and ψ_{spin} is the nuclear spin wavefunction. The overall wavefunction must have B_1 or B_2 symmetry. ψ_e and ψ_v have A_1 symmetry. The reducible representation of ψ_{spin} is shown in Table A.5, and its breakdown into the irreducible representations is given in Table A.6. The resulting nuclear spin statistical weights are given in Table A.7.

Table A.6: Reduction of the reducible representation of the nuclear spin wavefunctions of $C_6H_6(^{14}NH_3)$.

Γ	Contribution to Γ_{spin}
A_1	52
A_2	4
B_1	12
B_2	28
E_1	18
E_2	22
E_3	18
E_4	22
E_5	36
E_6	44
E_7	28
E_8	20

Table A.7: Nuclear spin statistical weights of $C_6H_6(^{14}NH_3)$.

Rotational State	Γ_{rot}	m=0	m=±1
k=0,J even	A_1	40	44
k=0, J odd	A_2	40	44
k=6q±1	E_5	88	76
k=6q±2	E_6	72	100
k=6q±3	$B_1 + B_2$	112	72
k=6q±6	$A_1 + A_2$	80	88

Bibliography

[1] P.R. Bunker, *Molecular Symmetry and Spectroscopy*, Academic Press, Orlando, FL, 1979.

[2] E.B. Wilson, Jr., *J. Chem. Phys.*, 3:276, 1935.

[3] A.J. Gotch, *Probing Solute/Solvent Interactions: A Study of Benzene-Small Molecule van der Waals' Complexes*, Ph.D. thesis, Purdue University, 1992.

Appendix B Experimental Details

B.1 Getting ZEKE-PFI Signals

First, the timing of the ionizing voltage pulse should be adjusted so the laser fires during the pulse. Electrons generated by laser ionization will be accelerated toward the detector. Grounding plugs should be put into the SHV feedthroughs for the post-extraction grid and the μ-metal tube, and then removed. It should be noted that the signal from electrons striking the detector appears strong on the oscilloscope when the plugs are removed, and then fades away. The grid and tube should again be grounded momentarily, and the signal observed. The process of grounding the grid and tube when the signal fades should be repeated several times over a period of $\sim$15 minutes. It should be observed that the signal decays rapidly at first, and more slowly later on. When the signal persists for several minutes, the grid and tube should be connected to the 9 V battery, whereupon the signal level should remain constant. If the timing of the ZEKE-PFI ionization pulse is now set to a value appropriate for ZEKE-PFI experiments, ZEKE-PFI signal should be observed when the laser is at an appropriate wavelength.

B.2 The General Valve

The driver circuit for the General Valve does not function properly in external trigger mode. The transistor in the circuit fails, drawing huge amounts of current from the power supply and creating impulsive interference. It should only be used in internal trigger mode. Another note of caution regarding the General Valve is that the valve itself will fail after use at a temperature of 170° C.

B.3 The Interlock Circuit

This interlock circuit was used to turn off the diffusion pumps (DPs) and close the gate valves if the flow of cooling water stopped or if the backing pressure was too high. Each DP was equipped with a flowmeter that generated an AC voltage proportional to the water flow. The circuit amplified these signals, converted them to DC, and compared them to reference voltages. The amplification and comparison circuits are shown in Figure B.1, along with the pinouts of the chips that were used. The input AC signals were filtered and then amplified with a non-inverting op amp circuit. Trim pots were used to adjust the gain. The amplified signals were then rectified and filtered to make DC signals. A comparator chip was used to compare these DC signals to reference voltages that could be adjusted with trim pots. The outputs of the comparators are high when the input voltages are larger than the reference voltages, which occurs when enough water is flowing. The outputs from the comparators are ANDed together with an AND gate to produce an output that is high only if all conditions are OK. A signal from the Pirani gauge is included inthe ANDing. A 5V signal is sent through a relay in the Pirani gauge which closes if the pressure is less than the set point (0.1 Torr) and passes the signal to the AND gate. If all signals are OK, the AND gate sends a 5V signal to the comparator chip that drives the relay.

The relay is used to open or close two voltage lines. One line is 120 V AC that is used to drive the gate valves and the contactors that serve as switches for the DPs. The other line is 5 V DC that that actually drives the relay. Obviously, the relay cannot close if it depends on power coming through its normally open contacts, and this feature is used to prevent the interlock from turning things on and off repeatedly. The relay is initially closed by flipping a toggle switch that sends 5 V to it. The relay then closes and is kept closed by the 5 V that goes through its contacts. If the circuit turns off, it can only be turned on again by flipping the toggle switch. Additional details are inside the front cover of the lab notebook.

Figure B.1: A partial circuit diagram showing the amplification, rectification, and comparison of the AC signals from the flowmeters, and the pinouts of the chips used in the interlock.

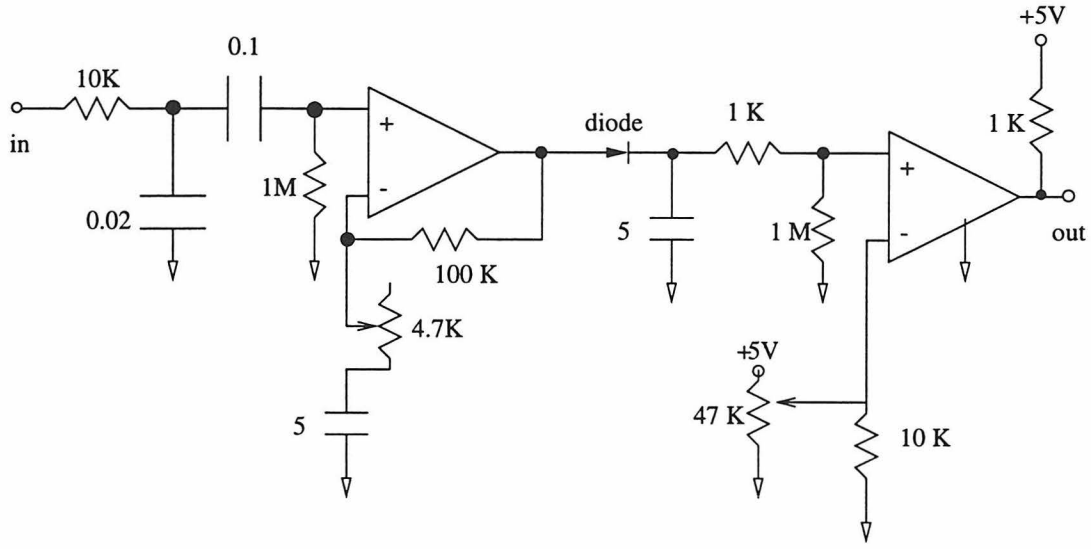

LM324N Quad op amp

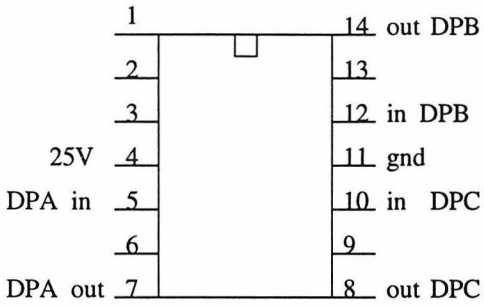

MC3302P Quad comparator

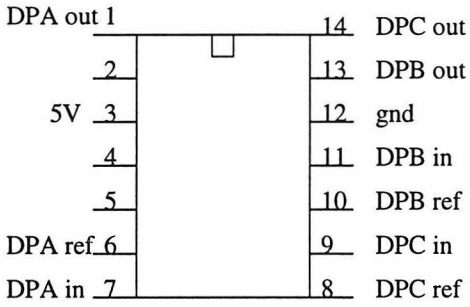

T74LS08 Quad AND gate

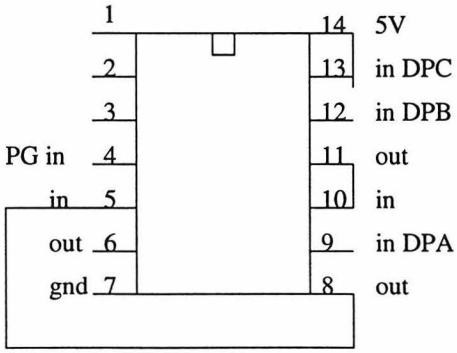

LM311 Comparator

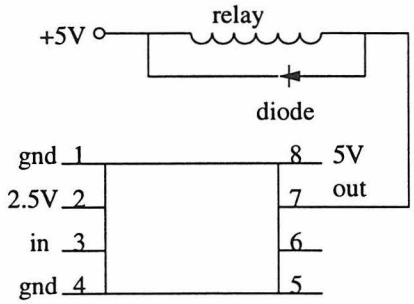

B.4 Data Collection Software

The data collection program, of which there are several versions, was written in Microsoft Quickbasic. The version given here is named scope8.bas. Several parameters must be changed in the program for each experiment, and these are labeled.

```
'THIS PROGRAM IS FOR READING  MASS SPECTRA  FROM THE LECROY.
'THE LASER IS STEPPED BY GPIB CONTROL.
'GRATING, CRYSTAL, AND ETALON SCANS CAN BE DONE.
'IN DELAY LOOPS, 125 COUNTS DELAY ONE MICROSECOND
DECLARE SUB crystep (calaray#(), calpts%, wavelen#, crypos&)
DECLARE SUB testbusy (devnum%)
DECLARE SUB sendpos (devnum%, gratstr$, etstr$, crystr$, restr$)
DECLARE SUB steps24letters (numstp&, bites3$)
DECLARE SUB getpos (devnum%, gratstr$, etstr$, crystr$, restr$)
DECLARE SUB letters24steps (instrg$, nsteps&)
DECLARE SUB letters2steps (instrg$, nsteps&)
DECLARE SUB steps2letters (numstp&, bites3$)
DECLARE SUB wrt (devnum%, outstr$)
DECLARE SUB rd (devnum%, instrg$)
DECLARE SUB getgains (gains%, fgain!, vgain%)
DECLARE SUB swchbites (ndat%)
COMMON SHARED /nistatblk/ ibsta%, iberr%, ibcnt%
'DECLARE THIS COMMON WHEN USING THE GPIB
DIM wave1%(1 TO 16000), wave2(1 TO 16000)
'******** DIMENSION THE DATARR ARRAY
DIM datarr(1 TO 601, 1 TO 20), mass(1 TO 50), ftime(1 TO 50), mpoint%(1 TO 50)
DIM mproc%(1 TO 30)
DIM junk%(1 TO 1000), wdesc%(1 TO 20), fdesc%(1 TO 20), ypix(1000), ypix2(1000)
DIM ypix3(512), ypix4(512)
DIM calaray#(1 TO 30, 1 TO 2)
'OUTPUT FILES
'******************** NAME FILE ***************************
OPEN "bnheir33.dat" FOR BINARY AS #2
OPEN "bnhei33.dat" FOR OUTPUT AS #1
'GOTO 10
'********************** SET UP MASS SPEC ******************
'*** ENTER MASSES TO PROCESS, RELATIVE TO THE CALIBRATION MASS (1)
mproc%(1) = 1
mproc%(2) = 18
mproc%(3) = 35
mproc%(4) = 79
mproc%(5) = 96
mproc%(6) = 79
mproc%(7) = 96
mproc%(8) = 113
'ENTER CALIBRATION MASS
mass(1) = 78
'THE TIME UNIT IS THE MICROSECOND
'ENTER THE ARRIVAL TIME OF THIS MASS
ftime(1) = 12.226
'ENTER THE NUMBER OF MASSES TO PROCESS
nmass% = 5
'CALCULATE THE ARRIVAL TIMES FOR THE OTHER MASSES
FOR idum% = 1 TO nmass% - 1
 mass(idum% + 1) = mass(1) + mproc%(idum% + 1) - 1
 ftime(idum% + 1) = SQR(mass(idum% + 1) / mass(1)) * ftime(1)
NEXT idum%
'PRINT ftime(1), ftime(2), ftime(3), ftime(6), ftime(7)
'******************** SET THIS
```

```
'**************CALCULATE THE POINTS WHERE THE OTHER MASS PEAKS OCCUR
'************* ENTER THE DELAY IN MICROSECONDS
'**** .01 is for the 10 ns sampling interval
tdel = 11
FOR idum% = 1 TO nmass%
 pinit% = INT(ftime(idum%) / .01)
 terr = ABS(ftime(idum%) - pinit% * .01)
 IF ABS(ftime(idum%) - (pinit% + 1) * .01) < terr THEN
  pinit% = pinit% + 1
 END IF
 mpoint%(idum%) = pinit% - tdel / .01 + 1
NEXT idum%
'PRINT mpoint%(1), mpoint%(2), mpoint%(3), mpoint%(6), mpoint%(7)
'GOTO 99
junk$ = "                    "
junkstr$ = "                                                    "
'************************** DO GRAPHICS
'GOTO 10
SCREEN 12
WINDOW (-64, -.13)-(576, 1.12)
LINE (0, 0)-(512, 0)
LINE (0, 0)-(0, 1)
LINE (0, 1)-(512, 1)
LINE (512, 0)-(512, 1)
'LINE (0, 0)-(512, 0)
LOCATE 28, 40
PRINT "x axis"
LOCATE 13, 1
PRINT "y axis"
'LOCATE 15, 7
'PRINT "0"
LOCATE 28, 8
PRINT "0"
LOCATE 28, 70
PRINT "512"
LOCATE 27, 6
PRINT "0"
LOCATE 3, 7
PRINT "1"
'LINE (0, 0)-(512, 0)
'GOTO 99
'*************** SET EVERY TIME *********************************
'NPTS IS THE NUMBER OF POINTS THAT ARE READ FROM THE WAVEFORM
npts! = 1000
npts% = 1000
'TAREA! SHOULD BE BIGGER THAN THE AREA OF THE PEAK
'TAREA IS USED TO NORMALIZE THE DATA
tarea! = -1
'SET THE NUMBER OF POINTS IN THE SCAN
datpts% = 200
'*****************************************************************
'PLTCNT IS THE CURRENT POINT
pltcnt% = 1
'GOTO 99
```

```
'********************** INITIALIZE DEVICES. SEE SCOPE MANUAL
10 CALL ibfind("gpib0", bdnum%)
'DEV1 IS THE LECROY
CALL ibfind("dev1", devnum%)
'DEV15 IS A LASER
CALL ibfind("dev15", devnum2%)
'GOTO 99
'***************** SET UP CRYSTAL CALIBRATION
'CALARAY#(*,1) CONTAINS THE CALIBRATED WAVELENGTHS
calaray#(1, 1) = 515!
'calaray#(1, 2) = -2434
'NUMBER OF CALIBRATION POINTS
ncal% = 6
FOR ical% = 2 TO ncal%
 calaray#(ical%, 1) = calaray#(1, 1) + (ical% - 1) * 1!
NEXT ical%
'FOR ical% = 1 TO 19
' wavelen# = calaray#(ical%, 1) + .05
' CALL crystep(calaray#(), ncal%, wavelen#, crypos&)
' PRINT crypos&
'NEXT ical%
'GOTO 99
'*************** FIND OR SET LASER MOTOR POSITIONS ***************
'gratcon# = 0
'CALL gratconrd(devnum2%, gratcon#)
gratcon# = 2278.65
gratpos& = 0
etpos& = 0
crypos& = 0
respos& = 0
gorder% = 6
gratstr$ = "      "
etstr$ = "    "
crystr$ = "    "
restr$ = "    "
CALL getpos(devnum2%, gratstr$, etstr$, crystr$, restr$)
CALL letters2steps(gratstr$, gratpos&)
CALL letters24steps(etstr$, etpos&)
CALL letters24steps(crystr$, crypos&)
'PRINT gratpos&, etpos&, crypos&
'GOTO 99
'SET MOTORS TO INITIAL POSITIONS OF THE SCAN
gratpos& = 263353 + 5
etpos& = 2890 + 5
crypos& = 12000 - 3160 - 100
CALL steps2letters(gratpos&, gratstr$)
CALL steps24letters(etpos&, etstr$)
CALL steps24letters(crypos&, crystr$)
CALL sendpos(devnum2%, gratstr$, etstr$, crystr$, restr$)
CALL testbusy(devnum2%)
gratpos& = gratpos& - 5
etpos& = etpos& - 5
crypos& = crypos& + 100
npos& = etpos& - 800
```

```
CALL steps2letters(gratpos&, gratstr$)
CALL steps24letters(etpos&, etstr$)
CALL steps24letters(crypos&, crystr$)
CALL sendpos(devnum2%, gratstr$, etstr$, crystr$, restr$)
CALL testbusy(devnum2%)
'GOTO 99
wavelen1# = (gratpos& * .00315 + gratcon#) / gorder%
wavenum1# = 1E+07 / wavelen1#
wavenum1# = wavenum1# + 11.5
'SET WAVENUMBER INCREMENT FOR THE SCAN
wvnuminc = .02
crypos1& = crypos&
GOTO 77
'TEST LASER SCAN ONLY
FOR iscan% = 1 TO 20
 wavenum# = wavenum1# + iscan% * wvnuminc
 wavelen# = 1E+07 / wavenum#
 gratpos1& = (gorder% * wavelen# - gratcon#) / .00315
 gratpos1& = gratpos1& + 16
' IF iscan% > 0 AND iscan% < 22 THEN
'  gratpos1& = gratpos1& + 18
' END IF
' IF iscan% >= 22 AND iscan% < 38 THEN
'  gratpos1& = gratpos1& + 10
' END IF
' IF iscan% >= 8 AND iscan% < 26 THEN
'  gratpos1& = gratpos1& + 12
' END IF
' IF iscan% >= 38 THEN
'  gratpos1& = gratpos1& + 0
' END IF
 cos2# = wavelen# * COS(.0025) / wavelen1#
 sin2# = SQR(1 - cos2# ^ 2)
 etsteps% = ATN(sin2# / cos2#) / 3.125E-06
 CALL crystep(calaray#(), ncal%, wavelen#, crypos1&)
 crypos1& = 12000 + crypos1&
 etpos1& = npos& + etsteps%
 PRINT gratpos1&, etpos1&, crypos1&
 gratpos1& = gratpos1& + 5
 etpos1& = etpos1& + 5
 CALL steps2letters(gratpos1&, gratstr$)
 CALL steps24letters(etpos1&, etstr$)
 CALL steps24letters(crypos1&, crystr$)
 CALL sendpos(devnum2%, gratstr$, etstr$, crystr$, restr$)
 CALL testbusy(devnum2%)
 gratpos1& = gratpos1& - 5
 etpos1& = etpos1& - 5
 CALL steps2letters(gratpos1&, gratstr$)
 CALL steps24letters(etpos1&, etstr$)
 CALL steps24letters(crypos1&, crystr$)
 CALL sendpos(devnum2%, gratstr$, etstr$, crystr$, restr$)
 CALL testbusy(devnum2%)
SLEEP 5
NEXT iscan%
```

```
'PRINT wavelen1#, wavenum1#
GOTO 99
'********************** SET UP SCOPE **************
77 outstr$ = "remote" + CHR$(13)
CALL ibwrt(devnum%, outstr$)
outstr$ = "CTRL,CR" + CHR$(13)
CALL ibwrt(devnum%, outstr$)
outstr$ = "cfmt,a,word" + CHR$(13)
CALL ibwrt(devnum%, outstr$)
outstr$ = "sel,fe" + CHR$(13)
CALL ibwrt(devnum%, outstr$)
'SET SCREEN TO REMOTE
'outstr$ = "scr,rm" + CHR$(13)
'CALL ibwrt(devnum%, outstr$)
'outstr$ = "scr,off" + CHR$(13)
'CALL ibwrt(devnum%, outstr$)
'CLEAR STATUS BYTE
outstr$ = "stb,5,?" + CHR$(13)
CALL ibwrt(devnum%, outstr$)
CALL ibrd(devnum%, junk$)
'******************** THIS IS THE MAIN LOOP FOR TAKING DATA
FOR idat% = 1 TO datpts%
LOCATE 1, 1
PRINT "  "
LOCATE 1, 1
PRINT idat%
'DELAY LOOP
'FOR ishit& = 1 TO 50000
'NEXT ishit&
'TURN SCREEN OFF
'outstr$ = "scr,off" + CHR$(13)
'CALL ibwrt(devnum%, outstr$)
'STEP LASER
 wavenum# = wavenum1# + (idat% - 1) * wvnuminc
 wavelen# = 1E+07 / wavenum#
 gratpos1& = (gorder% * wavelen# - gratcon#) / .00315
 gratpos1& = gratpos1& + 16
' IF idat% > 0 AND idat% < 275 THEN
'  gratpos1& = gratpos1& + 18
' END IF
' IF idat% >= 88 AND idat% < 286 THEN
'  gratpos1& = gratpos1& + 12
' END IF
' IF idat% >= 286 AND idat% < 418 THEN
'  gratpos1& = gratpos1& + 6
' END IF
' IF idat% >= 418 THEN
'  gratpos1& = gratpos1& + 0
' END IF
 cos2# = wavelen# * COS(.0025) / wavelen1#
 sin2# = SQR(1 - cos2# ^ 2)
 etsteps% = ATN(sin2# / cos2#) / 3.125E-06
 CALL crystep(calaray#(), ncal%, wavelen#, crypos1&)
 crypos1& = 12000 + crypos1&
```

```
etpos1& = npos& + etsteps%
' PRINT gratpos1&, etpos1&, crypos1&
gratpos1& = gratpos1& + 5
etpos1& = etpos1& + 5
CALL steps2letters(gratpos1&, gratstr$)
CALL steps24letters(etpos1&, etstr$)
CALL steps24letters(crypos1&, crystr$)
CALL sendpos(devnum2%, gratstr$, etstr$, crystr$, restr$)
CALL testbusy(devnum2%)
gratpos1& = gratpos1& - 5
etpos1& = etpos1& - 5
CALL steps2letters(gratpos1&, gratstr$)
CALL steps24letters(etpos1&, etstr$)
CALL steps24letters(crypos1&, crystr$)
CALL sendpos(devnum2%, gratstr$, etstr$, crystr$, restr$)
CALL testbusy(devnum2%)
'RESET AVERAGE
501 outstr$ = "arst" + CHR$(13)
CALL ibwrt(devnum%, outstr$)
'************* SLEEP DURING AVERAGING TO SPEED UP SCOPE ************
SLEEP 20
'*********** SEE IF AVERAGING IS DONE ******************
21 outstr$ = "stb,5,?" + CHR$(13)
CALL ibwrt(devnum%, outstr$)
CALL ibrd(devnum%, junkstr$)
aflag% = VAL(MID$(junkstr$, 7, 1))
IF aflag% < 8 THEN
 FOR ishit& = 1 TO 60000
 NEXT ishit&
GOTO 21
END IF
'DELAY LOOP.  EXTRA TRIGGERS NEEDED TO COMPLETE AVERAGING
FOR ishit& = 1 TO 20000
NEXT ishit&
'***************** USE FUNCTION F TO INTEGRATE FUNCTION E
'outstr$ = "trff,on" + CHR$(13)
'CALL ibwrt(devnum%, outstr$)
"DELAY LOOP.  EXTRA TRIGGERS NEEDED TO MAKE FUNC. F PARAMETERS
CURRENT
'FOR ishit& = 1 TO 30000
'NEXT ishit&
'TURN SCREEN ON
'outstr$ = "scr,on" + CHR$(13)
'CALL ibwrt(devnum%, outstr$)
'****************** READ DESCRIPTOR
outstr$ = "rd,fe.de" + CHR$(13)
CALL ibwrt(devnum%, outstr$)
CALL ibrdi(devnum%, fdesc%(), 10)
CALL swchbites(fdesc%(5))
'****** FDESC%(5) IS THE WAVEFORM OFFSET
'CALCULATE GAIN
'CALL swchbites(fdesc%(3))
'CALL getgains(fdesc%(3), fgain, vgain%)
'PRINT fgain, vgain%
```

```
'*************** READ DATA
'************* SET EVERY TIME ****************************
outstr$ = "rd,fe.da,1,1000,0" + CHR$(13)
CALL ibwrt(devnum%, outstr$)
'*************************************************************
instr3$ = "                                                                    "
CALL ibrdi(devnum%, junk%(), 4)
CALL ibrdi(devnum%, wave1%(), 25000)
CALL ibrd(devnum%, instr3$)
'*************** SAVE RAW DATA
PUT #2, , fdesc%(5)
FOR iraw% = 1 TO npts%
 PUT #2, , wave1%(iraw%)
NEXT iraw%
'******************** PROCESS DATA
'SEE SCOPE MANUAL
FOR i% = 1 TO npts%
 CALL swchbites(wave1%(i%))
 wave2(i%) = wave1%(i%)
 IF wave2(i%) < 0 THEN
  wave2(i%) = wave2(i%) + 65536
 END IF
 wave2(i%) = (wave2(i%) - 32768) / 8192 - (fdesc%(5) - 200) / 25
' WRITE #1, i%, wave2(i%)
NEXT
'PLOT DATA
'CALCULATE AREA OF PEAK
'******************** SET EVERY TIME ****************************
' ycrap = wave2(1) - wave2(26)
'DO A BASELINE CORRECTION
 FOR idumy% = 1 TO nmass%
  datarr(idat%, idumy%) = 0
  basel1 = wave2(mpoint%(idumy%) - 3) + wave2(mpoint%(idumy%) - 4)
  basel2 = wave2(mpoint%(idumy%) + 3) + wave2(mpoint%(idumy%) + 4)
  basel = (basel1 + basel2) / 4
'NOW ADD THE POINTS IN THE PEAK
  FOR ushit% = 1 TO 5
'  datarr(idat%, idumy%) = (wave2(mpoint%(idumy%) + minc%) - wave2(mpoint%(idumy%) -
minc%) - ycrap) * fgain / tarea!
   datarr(idat%, idumy%) = datarr(idat%, idumy%) + (wave2(mpoint%(idumy%) - 3 + ushit%) -
basel)
  NEXT ushit%
 datarr(idat%, idumy%) = datarr(idat%, idumy%) / tarea!
' WRITE #2, idumy%, datarr(idat%, idumy%)
 NEXT idumy%
'************* PLOT DATA
 ypix(idat%) = datarr(idat%, 2)
 PSET (idat% * 1, ypix(idat%))
' ypix2(idat%) = datarr(idat%, 3)
' PSET (idat% * 1, ypix2(idat%) + .5)
'FOR iplt% = 1 TO nmass%
'  PRESET (iplt% * 8, ypix(iplt%))
'  ypix(iplt%) = datarr(idat%, iplt%)
'  PSET (iplt% * 8, ypix(iplt%))
```

```
' NEXT iplt%
'FOR iplt% = 1 TO npts%
' PRESET (iplt%, ypix(iplt%))
' ypix(iplt%) = wave2(iplt%) / -8!
' PSET (iplt%, ypix(iplt%))
'NEXT iplt%
'*********************************************************************
pltcnt% = pltcnt% + 1
'DELAY LOOP
'FOR iwat& = 1 TO 32500
'NEXT iwat&
'outstr$ = "trff,off" + CHR$(13)
'CALL ibwrt(devnum%, outstr$)
'TURN SCREEN OFF
'outstr$ = "scr,off" + CHR$(13)
'CALL ibwrt(devnum%, outstr$)
'93 cstr$ = INKEY$
'IF LEN(cstr$) = 0 THEN
' GOTO 93
'END IF
NEXT idat%
'********************* WRITE DATA TO A FILE
88 FOR impt% = 1 TO nmass%
 FOR ipt% = 1 TO datpts%
'************ NOTE! DO YOU WANT TO SAVE RAW OR NORMALIZED DATA? ***
 WRITE #1, datarr(ipt%, impt%) * tarea! * -1
 NEXT ipt%
NEXT impt%
99 END

SUB chkerror
'THIS SUB STOPS THE PROGRAM IF A GPIB ERROR OCCURS
IF ibsta% >= 16384 THEN
 PRINT "ERROR OCCURRED"
 END
END IF
END SUB

SUB crystep (calaray#(), calpts%, wavelen#, crypos&)
'THIS SUB CALCULATES THE PROPER CRYSTAL POSITION FOR THE WAVELENGTH
IN USE.
'IT USES LINEAR INTERPOLATION.
'CALARAY#(*,1) CONTAINS THE WAVELENGTHS OF THE CALIBRATION POINTS
'CALPTS% : # OF CALIBRATION POINTS
'WAVELEN# : WAVELENGTH FOR WHICH CRYSTAL POSITION MUST BE
CALCULATED.
'1ST WAVELENGTH : 515 nm.  ADD 1nm PER POINT
calaray#(1, 2) = -2510 + 15
calaray#(2, 2) = -2729 + 15
calaray#(3, 2) = -2948 + 15
calaray#(4, 2) = -3163 + 15
calaray#(5, 2) = -3375 + 15
calaray#(6, 2) = -3587 + 15
calaray#(7, 2) = -2560
```

```
calaray#(8, 2) = -2580
calaray#(9, 2) = -2600
calaray#(10, 2) = -2623
calaray#(11, 2) = -2645
calaray#(12, 2) = -2666
calaray#(13, 2) = -2688
calaray#(14, 2) = -2710
calaray#(15, 2) = -2734
calaray#(16, 2) = -2756
calaray#(17, 2) = -2778
calaray#(18, 2) = -2800
calaray#(19, 2) = -2820
calaray#(20, 2) = -2842
calaray#(21, 2) = -2863
calaray#(22, 2) = -2884
calaray#(23, 2) = -2904
calaray#(24, 2) = -2927
calaray#(25, 2) = -2948
calaray#(26, 2) = -2970
calaray#(27, 2) = -2992
calaray#(28, 2) = -3015
imax% = 1
FOR i% = 2 TO calpts%
IF calaray#(i%, 1) > wavelen# THEN
 imax% = i%
 GOTO 11
END IF
NEXT i%
11 wavstep# = calaray#(imax%, 1) - calaray#(imax% - 1, 1)
cryinc# = calaray#(imax%, 2) - calaray#(imax% - 1, 2)
wavdiff# = wavelen# - calaray#(imax% - 1, 1)
crypos& = calaray#(imax% - 1, 2) + wavdiff# / wavstep# * cryinc#
END SUB

SUB getgains (gains%, fgain, vgain%)
'THIS SUB CONVERTS THE CODE NUMBER FOR THE VERTICAL GAIN
'TO THE VERTICAL GAIN.  SEE SCOPE MANUAL
'FCODE IS FIXED GAIN
fcode% = gains% \ 256
'VGAIN IS VARIABLE GAIN
vgain% = gains% - 256 * fcode%
IF gains% < 0 AND vgain% <> 0 THEN
 fcode% = fcode% - 1
END IF
vgain% = gains% - 256 * fcode%
'PRINT fcode%, vgain%
IF fcode% = 29 THEN
 fgain = 1
END IF
'BRACKET THE CODE NUMBER. FIND MANTISSA AND EXPONENT.
IF fcode% < 29 THEN
 lowlim% = 29
 fexp% = 0
 DO
```

```
 lowlim% = lowlim% - 3
 fexp% = fexp% - 1
LOOP UNTIL lowlim% <= fcode%
fdum% = fcode% - lowlim%
SELECT CASE fdum%
CASE 0
 fmant% = 1
CASE 1
 fmant% = 2
CASE 2
 fmant% = 5
END SELECT
fgain = fmant% * 10 ^ fexp%
END IF
IF fcode% > 29 THEN
 hilim% = 29
 fexp% = -1
 DO
  hilim% = hilim% + 3
  fexp% = fexp% + 1
 LOOP UNTIL hilim% > fcode%
 lowlim% = hilim% - 3
 fdum% = fcode% - lowlim%
 SELECT CASE fdum%
 CASE 0
  fmant% = 1
 CASE 1
  fmant% = 2
 CASE 2
  fmant% = 5
 END SELECT
 fgain = fmant% * 10 ^ fexp%
END IF
'PRINT fgain, vgain%
END SUB

SUB getpos (devnum%, gratstr$, etstr$, crystr$, restr$)
'THIS SUB GETS THE POSITIONS OF ALL FOUR STEPPER MOTORS
'POSTRG$ CONTAINS THE POSITIONS
postrg$ = "                "
CALL wrt(devnum%, "?A")
CALL rd(devnum%, postrg$)
gratstr$ = MID$(postrg$, 1, 6)
etstr$ = MID$(postrg$, 7, 4)
crystr$ = MID$(postrg$, 11, 4)
restr$ = MID$(postrg$, 15, 4)
END SUB

SUB gratconrd (devnum%, gratcon#)
'THIS SUB GETS THE GRATING CONSTANT AND PUTS IT IN GRATCON#
gratstr$ = "      "
gratreq$ = "?G"
CALL wrt(devnum%, gratreq$)
CALL rd(devnum%, gratstr$)
```

```
gratint& = 0
CALL letters2steps(gratstr$, gratint&)
gratcon# = gratint&
gratcon# = gratcon# / 1000!
END SUB

SUB gratconwrt (devnum%, gratcon&)
'THIS SUB SENDS A GRATING CALIBRATION CONSTANT TO THE LASER
CALL steps2letters(gratcon&, gratstr$)
gratout$ = "SG" + gratstr$
CALL wrt(devnum%, gratout$)
END SUB

SUB letters24steps (instrg$, nsteps&)
'THIS SUB CONVERTS A STRING OF FOUR LETTERS INTO AN INTEGER (NUMBER
'OF STEPS). IT DOES THE REVERSE OF WHAT SUB STEPS24LETTERS DOES.
'SEE THE DYE LASER MANUAL.
'WARNING! INSTRG$ MUST BE EXACTLY FOUR LETTERS LONG.
nsteps& = 0
FOR i% = 1 TO 4
 nsteps& = nsteps& + (ASC(MID$(instrg$, i%, 1)) - 65) * 16 ^ (i% - 1)
NEXT
END SUB

SUB letters2steps (instrg$, nsteps&)
'THIS SUB CONVERTS A STRING OF SIX LETTERS INTO AN INTEGER (NUMBER
'OF STEPS). IT DOES THE REVERSE OF WHAT SUB STEPS2LETTERS DOES.
'SEE THE DYE LASER MANUAL.
'WARNING! INSTRG$ MUST BE EXACTLY SIX LETTERS LONG.
nsteps& = 0
FOR i% = 1 TO 6
 nsteps& = nsteps& + (ASC(MID$(instrg$, i%, 1)) - 65) * 16 ^ (i% - 1)
NEXT
END SUB

SUB rd (devnum%, instrg$)
'THIS SUB READS READS A STRING FROM DEVICE DEVNUM%
CALL ibrd(devnum%, instrg$)
END SUB

SUB sendpos (devnum%, gratstr$, etstr$, crystr$, restr$)
outstr$ = "SA" + gratstr$ + etstr$ + crystr$ + restr$
CALL wrt(devnum%, outstr$)
END SUB

SUB steps24letters (numstp&, bites3$)
'THIS SUB CONVERTS AN INTEGER (NUMBER OF STEPS) TO A STRING
'FOUR LETTERS LONG. A BYTE IS REPRESENTED BY TWO LETTERS, EACH
'RANGING FROM A TO P. THIS FORM IS SIMILAR TO HEXADECIMAL, EXCEPT
'THAT 0 = A AND 15 = P.
'SEE THE DYE LASER MANUAL.
'VARIABLES :
'NUMSTP& : INTEGER NUMBER OF STEPS (INPUT)
'BITES3$ : STRING OF LETTERS (OUTPUT)
```

```
DIM num&(1 TO 4)
numdum& = numstp&
FOR i% = 4 TO 1 STEP -1
num&(i%) = INT(numdum& / 16 ^ (i% - 1))
numdum& = numdum& - num&(i%) * 16 ^ (i% - 1)
num&(i%) = 65 + num&(i%)
NEXT
bites3$ = " "
FOR i% = 1 TO 4
bites3$ = bites3$ + CHR$(num&(i%))
NEXT
bites3$ = LTRIM$(bites3$)
END SUB

SUB steps2letters (numstp&, bites3$)
'THIS SUB CONVERTS AN INTEGER (NUMBER OF STEPS) TO A STRING
'SIX LETTERS LONG.  A BYTE IS REPRESENTED BY TWO LETTERS, EACH
'RANGING FROM A TO P.  THIS FORM IS SIMILAR TO HEXADECIMAL, EXCEPT
'THAT 0 = A AND 15 = P.
'SEE THE DYE LASER MANUAL.
'VARIABLES :
'NUMSTP& : INTEGER NUMBER OF STEPS (INPUT)
'BITES3$ : STRING OF LETTERS (OUTPUT)
DIM num&(1 TO 6)
numdum& = numstp&
FOR i% = 6 TO 1 STEP -1
num&(i%) = INT(numdum& / 16 ^ (i% - 1))
numdum& = numdum& - num&(i%) * 16 ^ (i% - 1)
num&(i%) = 65 + num&(i%)
NEXT
bites3$ = " "
FOR i% = 1 TO 6
bites3$ = bites3$ + CHR$(num&(i%))
NEXT
bites3$ = LTRIM$(bites3$)
END SUB

SUB swchbites (ndat%)
'THIS SUB SWITCHES THE BYTES IN A WORD. NECESSARY FOR PCs.
 jstr$ = MKI$(ndat%)
 jstr2$ = MID$(jstr$, 2, 1)
 jstr2$ = jstr2$ + MID$(jstr$, 1, 1)
 ndat% = CVI(jstr2$)
END SUB

SUB testbusy (devnum%)
'THIS SUB CHECKS THE LASER'S BUSY FLAG UNTIL IT INDICATES READY
busyflag$ = "  "
DO UNTIL LEFT$(busyflag$, 1) = "R"
CALL wrt(devnum%, "?S")
CALL rd(devnum%, busyflag$)
'CHECK FOR ERRORS HERE AND PRINT MESSAGE IF ERROR AND EXIT SUB
LOOP
END SUB
```

```
SUB wrt (devnum%, outstr$)
'THIS SUB WRITES A STRING TO DEVICE DEVNUM%
'ADD CARRIAGE RETURN TO END OF STRING
outstr$ = outstr$ + CHR$(13)
CALL ibwrt(devnum%, outstr$)
'DO ERROR CHECKING HERE
END SUB
```